

ISTANBUL TECHNICAL UNIVERSITY ★ GRADUATE SCHOOL

**COMPRESSIVE SENSING OF
CYCLOSTATIONARY PROPELLER NOISE**

Ph.D. THESIS

Umut FIRAT

Department of Electronics & Communication Engineering

Telecommunication Engineering Programme

SEPTEMBER 2023

ISTANBUL TECHNICAL UNIVERSITY ★ GRADUATE SCHOOL

**COMPRESSIVE SENSING OF
CYCLOSTATIONARY PROPELLER NOISE**

Ph.D. THESIS

**Umut FIRAT
(504122303)**

Department of Electronics & Communication Engineering

Telecommunication Engineering Programme

Thesis Advisor: Prof. Dr. Tayfun AKGÜL

SEPTEMBER 2023

İSTANBUL TEKNİK ÜNİVERSİTESİ ★ LİSANSÜSTÜ EĞİTİM ENSTİTÜSÜ

**ÇEVİRİMSSEL DURAĞAN PERVANE GÜRÜLTÜSÜ İÇİN
SİKİŞTİRMALİ ALGILAMA**

DOKTORA TEZİ

**Umut FIRAT
(504122303)**

Elektronik ve Haberleşme Mühendisliği Anabilim Dalı

Telekomünikasyon Mühendisliği Programı

Tez Danışmanı: Prof. Dr. Tayfun AKGÜL

EYLÜL 2023

To my family, friends, and Ezgi

FOREWORD

This dissertation is a product of a prolonged and rough journey. I am grateful to my advisor Prof. Dr. Tayfun AKGÜL for his invaluable guidance during this pursuit. I also would like to acknowledge the steering committee members Prof. Dr. Aydın BAYTAN ERTÜZÜN and Prof. Dr. Hakan Ali ÇIRPAN for their constructive comments.

I would like to thank Dr. Ahmet YILMAZ for sharing his doctoral experience, Ph.D. candidate Barlas TOKGÖZ for accompanying me in our mutual quest, Cesur Cevdet OKUTAN for his valuable suggestions, Ufuk Levan YAKUT for his inquisitive questions and to all my friends and colleagues tolerating my absence throughout this work.

I would like to thank my family who have struggled to understand my curiously long Ph.D. process, though they have always rooted for me. I owe an exclusive gratitude to Ezgi ARIDURU whose endurance made this work possible.

September 2023

Umut FIRAT
(Electronics & Communications Engineer, M.Sc.)

TABLE OF CONTENTS

	<u>Page</u>
FOREWORD	ix
TABLE OF CONTENTS	xi
ABBREVIATIONS	xiii
SYMBOLS	xv
LIST OF TABLES	xvii
LIST OF FIGURES	xix
SUMMARY	xxiii
ÖZET	xxv
1. INTRODUCTION	1
1.1 Propeller Cavitation Noise	1
1.2 Cyclostationary Random Processes	3
1.3 Compressive Sensing	4
1.4 Purpose and Scope of the Thesis	6
1.5 Contribution of the Thesis	8
2. COMPRESSIVE SENSING FOR CYCLOSTATIONARY DETECTION .	11
2.1 Introduction	11
2.2 Cyclostationary Propeller Noise	14
2.2.1 Propeller noise measurement model	14
2.2.2 Sparsity of the SCF	15
2.2.3 Cyclic modulation spectrum	18
2.2.4 Cyclic modulation coherence	19
2.3 Compressive Sensing	22
2.3.1 Sparse approximation	23
2.3.2 Sensing matrix construction	25
2.3.3 Proposed approach	26
2.4 Numerical Examples	29
2.5 Discussion	37
3. HIGHER-ORDER CYCLIC SPECTRA AND COMPRESSIVE SENSING	39
3.1 Introduction	39
3.2 Higher-Order Cyclostationary Statistics	40
3.2.1 Cyclic bispectrum	41
3.2.2 Cyclic modulation bispectrum	42
3.3 Compressive Sensing of Cyclic Modulation Bispectrum	44
3.4 Experimental Results	46
4. CYCLIC COMPRESSIVE BEAMFORMING	53
4.1 Introduction	53
4.2 DOA Estimation	56

4.2.1	The narrowband model	56
4.2.2	The broadband model	58
4.3	Compressive Sensing	58
4.3.1	Sparse approximation	58
4.3.2	Sensing matrix.....	59
4.3.3	Compressive beamformer.....	59
4.4	Cyclic Compressive Beamformer	61
4.4.1	Cyclostationary propeller noise	61
4.4.2	Cyclic modulation spectrum	62
4.4.3	Cyclic sparse approximation.....	63
4.4.4	Computational complexity of the CCB	66
4.5	Analytical Performance of the CCB	67
4.5.1	Asymptotic CMS	67
4.5.2	Averaged CMS	69
4.5.3	MSE of the CCB	70
4.6	Experimental Results	71
4.7	Discussion	78
5.	CONCLUSIONS AND RECOMMENDATIONS.....	83
	REFERENCES	87
	APPENDICES	97
	APPENDIX A: SCF of the Propeller Noise	99
	APPENDIX B: Asymptotic Bias of the CCB.....	101
	APPENDIX C: Finite-Sample Bias and Variance of the CCB	103
	APPENDIX D: Algebraic Manipulations for Finite-Sample Variance of the CCB.....	105
	CURRICULUM VITAE.....	113

ABBREVIATIONS

AM	: Amplitude Modulation
AMSE	: Analytical MSE
ABIHT	: Averaged BIHT
ACMS	: Averaged CMS
BCoSaMP	: Block CoSaMP
BIHT	: Block IHT
BANAS	: Bosphorus Ambient Noise Acquisition System
BR	: Blade Rate
CB	: Compressive Beamformer
CBS	: Cyclic Bispectrum
CCB	: Cyclic CB
CLT	: Central Limit Theorem
CMBC	: Cyclic Modulation Bicoherence
CMBS	: Cyclic Modulation Bispectrum
CMC	: Cyclic Modulation Coherence
CMS	: Cyclic Modulation Spectrum
CoSaMP	: Compressive Sampling Matching Pursuit
CRB	: Cramér-Rao Bound
CS	: Compressive Sensing
DEMON	: Detection of Envelope Modulation on Noise
DSNR	: Detection SNR
DOA	: Direction-of-Arrival
DFT	: Discrete FT
EAF	: Expected Ambiguity Function
FFT	: Fast FT
FS	: Fourier Series
FT	: Fourier Transform
HOS	: Higher-Order Statistics
ICMBC	: Integrated CMBC
ICMC	: Integrated CMC
IHT	: Iterative Hard Thresholding
i.i.d.	: independent identically distributed
MSE	: Mean Square Error
MVDR	: Minimum Variance Distortionless Response
MMV	: Multiple Measurement Vector
MUSIC	: Multiple Signal Classification
NOB	: Number of Blades
NP	: Non-deterministic Polynomial-time
NMSE	: Normalized/Numerical MSE
NOS	: Number of Shafts
OMP	: Orthogonal Matching Pursuit
PHD	: Pisarenko Harmonic Decomposition

PSD	: Power Spectral Density
PSR	: Propeller Shaft Rate
RSNR	: Reconstruction SNR
RIP	: Restricted Isometry Property
SOS	: Second-Order Statistics
STFT	: Short-Time FT
SNR	: Signal-to-Noise Ratio
SMV	: Single Measurement Vector
SVD	: Singular Value Decomposition
SCF	: Spectral Correlation Function
TF	: Time-Frequency
ULA	: Uniform Linear Array

SYMBOLS

a	: Steering vector
A	: Array manifold matrix
α	: Cyclic frequency
B_{3x}	: Time-varying/cyclic bispectrum of $x(t)$
β	: Spectral frequency in Chapter 2
$c(t)$: Broadband propeller noise
C_x	: Cyclic autocorrelation function of $x(t)$
C_{3x}	: Instantaneous/cyclic third-order cumulant of $x(t)$
χ^2	: Chi-square distributed random variable
D	: Signal size in Chapter 2 & 3
$D(\cdot)$: Dirichlet kernel
$\delta(\cdot)$: Dirac operator
e	: Noise vector
F	: Fourier transform matrix
G_A	: Gram matrix of A
g_x	: Integrated cyclic modulation coherence of $x(t)$
G_x	: Cyclic modulation coherence of $x(t)$
g_{3x}	: Integrated cyclic modulation bicoherence of $x(t)$
G_{3x}	: Cyclic modulation bicoherence of $x(t)$
I	: Number of snapshots in Chapter 4
K	: Sparsity
L	: Analysis window size in Chapter 2 & 3 and signal size in Chapter 4
λ	: Statistical threshold
μ	: Modulation index
M	: Number of sensors/compressive samples
N	: Number of snapshots in Chapter 2 & 3, analysis window size in Chapter 4
N	: Noise matrix
N (ω, t)	: Noise short-time Fourier transform matrix
$v(t)$: Ambient noise
O	: Permutation matrix
ω	: Spectral frequency in Chapter 3 & 4
p	: Level of significance
P	: Cyclic modulation spectrum matrix
P_x	: Cyclic modulation spectrum of $x(t)$
P_{3x}	: Cyclic modulation bispectrum of $x(t)$
Φ	: Orthonormal basis
ψ	: Coherence
Ψ	: Sensing/measurement matrix
R	: Shifting size in Chapter 4
Q	: Number of source directions
R_x	: Autocorrelation function of $x(t)$
s	: Sparse source signal/vector

S	: Source matrix
$s(t)$: Source propeller noise
σ^2	: Variance
S (ω, t)	: Source short-time Fourier transform matrix
S_x	: Spectral correlation function of $x(t)$
t	: Time variable
θ	: Direction of arrival
V	: Shifting size in Chapter 2 & 3
$w(\cdot)$: Analysis window
W_x	: Wigner-Ville distribution of $x(t)$
x	: Sensor signal/vector
X	: Sensor measurements matrix
ξ	: Restricted isometry constant
$x(t)$: Sensor propeller noise
X (ω, t)	: Signal short-time Fourier transform matrix
y	: Sparse signal/vector
Y	: Compressive samples matrix
z	: Compressive measurements/vector

LIST OF TABLES

	<u>Page</u>
Table 2.1 : Parameters used in the Algorithms 1 and 2	30
Table 3.1 : Parameters used in the Algorithms 3 and 4	47
Table 3.2 : RSNR values for SOS and HOS	49
Table 4.1 : Parameters used in the Algorithms 5 and 6	66
Table 4.2 : Computational complexity of DOA estimation methods	67

LIST OF FIGURES

	<u>Page</u>
Figure 2.1 : Representative ship-radiated noise spectrum with the additive ambient noise.	12
Figure 2.2 : Relations between second-order statistics.	16
Figure 2.3 : Spectral support of the SCF of the propeller noise model given in (2.1).....	17
Figure 2.4 : Actual radiated-noise of a ship of opportunity with additive ambient noise measured with BANAS in the Strait of Istanbul a) its one-second-long segment, b) its CMS (in dB scale due to extreme variation in the spectral frequency dimension), c) its CMS at $\beta_0 = 10\text{kHz}$ (in linear scale).	20
Figure 2.5 : a) CMC (in linear scale) corresponding to CMS of Fig. 2.4, b) ICMC integrated along all the spectral band together with the statistical threshold (dotted line), DSNR = 112 (see (2.27) for the definition of DSNR), $p = 0.001$	23
Figure 2.6 : Row- ℓ_2 -norms of \mathbf{P}_x corresponding to the CMS given in Fig. 2.4. ..	28
Figure 2.7 : NMSE, DSNR and P_d plots averaged over 1000 trials for SNR = 0 dB of a-b-c) weakly modulated propeller noise ($\mu = 0.25$), d-e-f) moderately modulated propeller noise ($\mu = 0.5$), g-h-i) strongly modulated propeller noise ($\mu = 0.75$), respectively. NMSE, DSNR and P_d curves indicated by 'CoSaMP' and 'IHT' give the results obtained by the ICMCs recovered with Algorithm 1 and 2, respectively. DSNR and P_d curves indicated by 'Nyquist' give the results obtained by the Nyquist-rate ICMC.....	32
Figure 2.8 : NMSE, DSNR and P_d plots averaged over 1000 trials for SNR = 10 dB of a-b-c) weakly modulated propeller noise ($\mu = 0.25$), d-e-f) moderately modulated propeller noise ($\mu = 0.5$), g-h-i) strongly modulated propeller noise ($\mu = 0.75$), respectively. NMSE, DSNR and P_d curves indicated by 'CoSaMP' and 'IHT' give the results obtained by the ICMCs recovered with Algorithm 1 and 2, respectively. DSNR and P_d curves indicated by 'Nyquist' give the results obtained by the Nyquist-rate ICMC.	34
Figure 2.9 : CMC and ICMC recovered with a,b) Algorithm 1 (BCoSaMP), NMSE = 0.4734, DSNR = 117.74, c,d) Algorithm 2 (BIHT), NMSE = 0.4750, DSNR = 118.63, respectively. Compression rate is $M/N = 0.5$. For Nyquist-rate CMC and ICMC, see Fig. 2.5. Dotted line indicates the statistical threshold with %0.1 level of significance.....	36
Figure 3.1 : Relations between third-order statistics.....	42

Figure 3.2 : Spectral support of the cyclic bispectrum of the propeller noise model given in (3.1).	43
Figure 3.3 : ICMC and ICMBC with their maxima normalized to one.	48
Figure 3.4 : ICMCs and ICMBCs obtained by Nyquist-rate samples, recovered with BCoSaMP and BIHT for a) ICMC with $M = 0.1N$, b) ICMBC with $M = 0.1N$, c) ICMC with $M = 0.3N$, d) ICMBC with $M = 0.3N$, e) ICMC with $M = 0.5N$, and f) ICMBC with $M = 0.5N$	50
Figure 3.5 : RSNR values for recovered ICMCs (BCoSaMP in green, BIHT in magenta) and ICMBCs (BCoSaMP in blue, BIHT in red). Sub-figures in each column represent the same number of compressive samples (labeled on top) whereas each row shows the same modulation index (labeled right).	51
Figure 4.1 : Comparison of DOA estimation methods with an 8-sensor ULA for two closely-spaced sources, i.e., $\theta_0 = -2^\circ$ and $\theta_1 = 2^\circ$ with equal modulation indices of 0.5. The spatial power spectra are shown for SNR=0 dB with a) equally powered uncorrelated sources and b) the grid magnified around the true DOAs; for SNR=20 dB with c) equally powered correlated sources and again d) the grid magnified around the true DOAs.	55
Figure 4.2 : Absolute Gram matrices for a ULA with a) $M = 8$ at $\omega_d/2$, b) $M = 8$ at ω_d , c) $M = 64$ at $\omega_d/2$, and d) $M = 64$ at ω_d	60
Figure 4.3 : Normalized magnitude of the Dirichlet kernel at ω_d (solid blue), its first derivative (solid red) and second derivative (solid green) have higher contributions for closely-spaced sources compared to averaging it over ω_n 's (dashed blue) with the average of its first derivatives (dashed red) and second derivatives (dashed green).	70
Figure 4.4 : Spatial power spectra of classical beamforming methods a) Bartlett, b) Capon and c) MUSIC under uncorrelated sources along with real DOAs and refined estimates. Two sources are at $\theta_0 = -2^\circ$ and $\theta_1 = 2^\circ$ both with 0 dB SNR, and $\mu = 0.5$	72
Figure 4.5 : Spatial power spectra of compressive beamforming methods under uncorrelated sources along with real DOAs and refined estimates a) CB-BIHT, b) CB-ABIHT, c) CCB-BIHT and d) CCB-ABIHT. Two sources are at $\theta_0 = -2^\circ$ and $\theta_1 = 2^\circ$ both with 0 dB SNR, and $\mu = 0.5$	73
Figure 4.6 : Spatial power spectra of classical beamforming methods a) Bartlett, b) Capon and c) MUSIC under highly correlated sources along with real DOAs and refined estimates. Two sources are at $\theta_0 = -2^\circ$ and $\theta_1 = 2^\circ$ both with 20 dB SNR, and $\mu = 0.5$	74
Figure 4.7 : Spatial power spectra of compressive beamforming methods under highly correlated sources along with real DOAs and refined estimates, a) CB-BIHT, b) CB-ABIHT, c) CCB-BIHT and d) CCB-ABIHT. Two sources are at $\theta_0 = -2^\circ$ and $\theta_1 = 2^\circ$ both with 20 dB SNR, and $\mu = 0.5$	75
Figure 4.8 : MSE vs. SNR for two sources at $\theta_0 = -2^\circ$ and $\theta_1 = 2^\circ$ both with $\mu = 0.5$. a) NMSEs for all methods, b) AMSEs with NMSEs for CCB methods.	77

Figure 4.9 : MSE vs. modulation index for two sources at $\theta_0 = -2^\circ$ and $\theta_1 = 2^\circ$ both with 10 dB SNR. a) NMSEs for all methods, b) AMSEs with NMSEs for CCB methods. (Finite sample MSEs are too large (approx. 10^{26}) to display for $\mu = 0$ since the denominators of (4.47) and (4.49) are much smaller than their numerators, i.e., (4.41) is very small.)	78
Figure 4.10 : MSE vs. number of sources for 4° -apart sources all with 10 dB SNR and $\mu = 0.5$. a) NMSEs for all methods, b) AMSEs with NMSEs for CCB methods (with a zoom to the overlapping lines for $K \geq 3$ and $\text{MSE} \leq 3 \times 10^{-5}$).	79
Figure 4.11 : MSE vs. angle difference between DOAs for two sources both with 10 dB SNR and $\mu = 0.5$. a) NMSEs for all methods, b) AMSEs with NMSEs for CCB methods.	80
Figure 4.12 : MSE vs. number of sensors for two sources at $\theta_0 = -2^\circ$ and $\theta_1 = 2^\circ$ both with 10 dB SNR and $\mu = 0.5$. a) NMSEs for all methods, b) AMSEs with NMSEs for CCB methods.	81

COMPRESSIVE SENSING OF CYCLOSTATIONARY PROPELLER NOISE

SUMMARY

This dissertation is the combination of three manuscripts –either published in or submitted to journals– on compressive sensing of propeller noise for detection, identification and localization of water crafts. Propeller noise, as a result of rotating blades, is broadband and radiates through water dominating underwater acoustic noise spectrum especially when cavitation develops. Propeller cavitation yields cyclostationary noise which can be modeled by amplitude modulation, i.e., the envelope-carrier product. The envelope consists of the so-called propeller tonals representing propeller characteristics which is used to identify water crafts whereas the carrier is a stationary broadband process.

Sampling for propeller noise processing yields large data sizes due to Nyquist rate and multiple sensor deployment. A compressive sensing scheme is proposed for efficient sampling of second-order cyclostationary propeller noise since the spectral correlation function of the amplitude modulation model is sparse as shown in this thesis. A linear relationship between the compressive and Nyquist-rate cyclic modulation spectra is derived to utilize matrix representations for the proposed method. Cyclic modulation coherence is employed to demonstrate the effect of compressive sensing in terms of statistical detection. Recovery and detection performances of sparse approximation algorithms based on greedy pursuits are compared. Results obtained with synthetic and real data show that compression is achievable without lowering the detection performance. Main challenges are weak modulation, low signal-to-noise ratio and nonstationarity of the additive ambient noise, all of which reduce the sparsity level causing degraded recovery and detection performance.

Higher-order cyclostationary statistics is introduced to characterize propeller noise due to its non-Gaussian nature. The third-order cyclic cumulant spectrum, also known as the cyclic bispectrum, is derived and its sparsity is demonstrated for the amplitude modulated propeller noise model. Cyclic modulation bispectrum is proposed for feasible approximation of the cyclic bispectrum based solely on the discrete Fourier transform. Additionally, compressive sensing of the cyclic modulation bispectrum is suggested. Numerical results are presented for acquisition of the propeller tonals using real-world underwater acoustic data. Tonals estimated by third-order cyclic modulation bicoherence are more notable than the ones obtained by second-order cyclic modulation coherence due to latter's higher noise floor. Sparse recovery results show that frequencies of the prominent tonals can be obtained with sampling significantly below the Nyquist rate. The accurate estimation of tonal magnitudes, on the other hand, is challenging even with large number of compressive samples.

Compressive sensing can be extended to solve underdetermined system of equations which appears in direction-of-arrival estimation with uniform linear arrays. An estimator is proposed based on the compressive beamformer for cyclostationary propeller noise. Its asymptotic bias is derived, which is inherited from the conventional beamformer when there are multiple sources. Squared asymptotic bias and the finite-sample variance, also derived explicitly, constitute the mean-squared error. Spectral averaging is suggested to mitigate this error by decreasing the adverse effect of the spatial Dirichlet kernel. For low signal-to-noise ratios, averaging enables the proposed estimator to outperform the methods that assume stationarity. This is achieved even under weak cyclostationarity, numerous closely-spaced sources and few sensors.

The proposed methods are not only suitable for compressive sensing of propeller cavitation noise but also for general class of cyclostationary signals. Relevant research areas include but are not limited to communication, radar, acoustics and mechanical systems with applications such as spectrum sensing, modulation recognition, time difference of arrival estimation, time-frequency distributions, compressive detection and rolling element bearing fault diagnosis.

ÇEVİRİMSEL DURAĞAN PERVANE GÜRÜLTÜSÜ İÇİN SIKIŞTIRMALI ALGILAMA

ÖZET

Pervane kavitasyonu sonucu sualtına yayılan gürültü, deniz taşıtlarını sezme, konumlandırmak ve tanımlamak için temel bir akustik kaynaktır. Hidrofon olarak da bilinen sualtı ses algılayıcıları, oşinografik ve askeri uygulamalarda bu kaynakları yakalayarak pervane (ya da kavitasyon) tonlarından hayati bilgilerin çeşitli işaret işleme yöntemleriyle çıkarılmasını sağlamaktadır. Pervane tonlarının izge analizi, 21. yüzyılın başlarına kadar “zarf analizi” olarak sınıflandırılan ve keyfi parametre ayarlarına dayalı ampirik yöntemlerle yapılmaktaydı. Takip eden yıllarda, haberleşme işaretlerini nitelendirmede hali hazırda kullanılmakta olan çevrimsel durağan süreçler, pervane tonlarının tanımlanmasında daha titiz bir yaklaşım olarak işlev kazandı. Örneklemeye teorisinde eşzamanlı ve bağımsız olarak yaşanan gelişmeler, sıkıştırımlı algılama adıyla, pervane tonlarının seyrek vektörler olarak modellenmesine ve verimsiz Nyquist-Shannon örneklemeye kuramının üstesinden gelinmesine olanak sağladı. Sonuç olarak, uzamsal ve izgesel anlamda seyrek pervane bilgisinin eşzamanlı sıkıştırılması ve algılanması kullanışlı hale geldi. Bu tezin ana amacı, pervane tonlarının seyrekliğinden faydalanarak bu kullanışlılığın araştırılması ve yenilikçi sezim kestirim yöntemlerinin önerilmesidir.

Geniş bant pervane gürültüsünün kavitasyon sonucu genlik kiplemesine uğraması ikinci dereceden çevrimsel durağan gemi gürültüsüne yol açar. Kipleme işaretin pervane tonlarından oluşan izgesi denizaltılar ya da suüstü gemilerin sezim ve sınıflandırmasını mümkün kılmaktadır. Ancak, bu amaçla toplanan veriler, yüksek örneklemeye frekansları ve çoklu algılayıcı kullanımı nedeniyle büyük boyutlara ulaşmaktadır. Bu tezde, veri toplamanın enerji verimliliği, donanım karmaşıklığı ve bellek kapasitesine olan olumsuz etkilerinin azaltılması için pervane tonlarının sıkıştırımlı algılamasına yönelik bir plan önerilmektedir. Bu kapsamda, çevrimsel durağan pervane gürültüsüne ait izgesel ilinti işlevinin seyrek olduğu gösterilmektedir. İzgesel ilinti işlevinin kestirimi olan çevrimsel kipleme izgesinin sıkıştırımlı ve Nyquist hızında örneklenmiş hali arasındaki doğrusal ilişki türetilmektedir. Böylece, sıkıştırımlı algılamada ihtiyaç duyulan matris/vektör gösterimi kullanılabilir. Diğer yandan, çevrimsel kipleme izgesinin düzgelenmiş hali olan çevrimsel kipleme evreuyumluluğu, sıkıştırımlı algılamanın istatistiksel sezimde verdiği sonuçları değerlendirmek için kullanılmaktadır. Özyineli eşikleme (*iterative hard thresholding*) ve sıkıştırımlı eşleme takibi (*compressive sampling matching pursuit*) gibi seyrek yaklaşımlama algoritmalarının geri çatma ve sezim başarımı karşılaştırılmaktadır. Elde edilen sonuçlar, sezim başarımını olumsuz etkilemeden, sıkıştırmanın başarılı olduğunu göstermektedir. Zayıf kipleme, düşük işaret-gürültü oranı ve ortam gürültüsünün durağan olmayan doğası gibi başlıca zorluklar seyrekliği azaltmakta, dolayısıyla geri çatma ve sezim başarımını olumsuz etkilemektedir.

Bu tezde, pervane kavitasyon gürültüsünün yüksek dereceden çevrimsel durağan istatistiklerini edinmek için de bir yöntem önerilmektedir. Çevrimsel ikiz izge olarak da bilinen üçüncü dereceden çevrimsel kümülant izgesi türetilmekte ve genlik kiplemeli pervane gürültüsünün seyrekliği gösterilmektedir. Çevrimsel ikiz izgenin kestirimi için yalnızca ayrık Fourier dönüşümüne dayanan çevrimsel kipleme ikiz izgesi önerilmektedir. Çevrimsel kipleme ikiz izgesinin sıkıştırılmalı algılaması için kısmi bir Fourier temeli tavsiye edilmektedir. Bu ikiz izgenin seyrek geri çatımı çoklu ölçüm vektörü problemi olarak formüleştirmektedir. Önerilen yöntem, sadece pervane gürültüsü için değil, aynı zamanda genel anlamda Gauss dağılımlı olmayan çevrimsel durağan işaretler için de uygundur. Gerçek sualtı akustik verilerinden pervane tonlarının edinimi için bir örnek verilmektedir. Farklı sayıda sıkıştırılmalı örnek için elde edilen seyrek geri çatma sonuçları karşılaştırılmaktadır. Nyquist hızından kayda değer derecede düşük hızlarda örnekleme durumunda bile belirgin tonların frekanslarının elde edilebileceği gösterilmektedir. Diğer yandan, ton büyüklüklerinin kesin kestirimi, görece yüksek sayıda sıkıştırılmalı örnekleme bile zorlayıcıdır.

Son olarak, çevrimsel durağan gemi gürültüleri için sıkıştırılmalı hüzme şekillendirmeye dayalı bir geliş yönü kestirimcisi önerilmektedir. Birden fazla kaynak olması durumunda geleneksel hüzme şekillendiriciden devralınan asimptotik yanlılık önerilen kestirimci için türetilmektedir. Yine, açıkça türetilen sonlu örnek değışintisi ve karesel asimptotik yanlılık ortalama karesel hatayı oluşturmaktadır. Uzamsal Dirichlet çekirdeği nedeniyle oluşan bu hatayı azaltmak için izgesel ortalama alma tavsiye edilmektedir. Düşük işaret-gürültü oranlarında, durağan kaynak varsayan yöntemlere ortalama alma sayesinde üstünlük sağlanmaktadır. Buna, zayıf çevrimsel durağanlık, çok sayıda yakın kaynak ve az sayıda algılayıcı durumunda bile erişilebilmektedir.

Çevrimsel durağanlığın sıkıştırılması ve konumlandırılması, bu tezde, pervane kavitasyon gürültüsünün genlik kiplemesiyle modellenmesi örneklenecek incelenmektedir. Halbuki, literatürden alınan ve bu tezde geliştirilen sıkıştırılmalı algılama ve çevrimsel durağanlık araçları ikinci ve yüksek dereceden çevrimsel durağan istatistikleri içeren birçok alanda kullanıma uygundur. Örneğin, haberleşme işaretleri yüksek örnekleme frekanslarında edinilen ve çoğunlukla seyrek işaretlerdir. Bu tezde geliştirilen yöntemler, haberleşmede bilişsel radyo için izge algılama olarak bilinen problemin çözümünde hem sıkıştırma hem de yön bulma amacıyla kullanılabilir. Üstelik, bu yöntemler hem elektromanyetik hem de akustik işaretlere uygulanabilir. Bir diğer akustik örnek, mekanik sistemlerden toplanan işaretlerde ortaya çıkmaktadır. Dönen parçalar içeren makinalar çevrimsel durağan ve seyrek işaretler üretir. Bu makineler, rulman arıza teşhisi adı verilen yaklaşımla sürekli izlenir. Bu sırada büyük miktarda veri toplanır. Dönen parçaların ürettiği çevrimsel durağan tonların frekanslarında meydana gelen değışim makine arızasının tespitinde kullanılır. Dolayısıyla, bu tezde önerilen sıkıştırma ve sezim yöntemleri hem veri boyutunu azaltmak hem de geri çatılan sıkıştırılmalı verilerden sezim yapmak için kullanılabilir.

Bu bilgiler ışığında, pervane kavitasyon gürültüsünün ve genel anlamda çevrimsel durağan işaretlerin sıkıştırılmalı algılamasında bu tezin katkıları şu şekilde sıralanabilir: Genlik kiplemeli işaret modelinin izge ilinti işlevinin seyrekliğinin gösterilmesi; Nyquist hızında örneklenmiş ve sıkıştırılmalı çevrimsel kipleme izgesi arasında doğrusal ölçüm ilişkisinin türetilmesi; Nyquist hızında örneklenmiş çevrimsel kipleme

izgesinin seyrek geri çatımı; geri çatılmış ve Nyquist hızındaki örneklerle sezim kabiliyetlerinin karşılaştırılması; çevrimsel ikiz izgenin türetilmesi ve çevrimsel frekans uzayında seyrekliğinin gösterilmesi; gürbüz sezim için çevrimsel kipleme ikiz evreuyumluluğunun önerilmesi; çevrimsel kipleme ikiz izgesiyle sıkıştırılmalı algılama; ikinci dereceden çevrimsel durağan kaynakların geliş yönü kestirimi için yenilikçi bir yöntem önerilmesi; önerilen çevrimsel sıkıştırılmalı hüzme şekillendiricinin ortalama karesel hatasının türetilmesi; klasik ve sıkıştırılmalı geliş yönü kestirimcilerinin başarımlarının karşılaştırılması.

1. INTRODUCTION

Underwater radiated noise induced by propeller cavitation is a fundamental acoustic source to detect, localize and identify water crafts. Underwater sound sensors, also known as hydrophones, capture these sources enabling several signal processing methods to extract crucial information on the propeller (or cavitation) tonals in oceanographic and military applications. Until the beginning of the 21st century, spectral analysis of propeller tonals has relied on empirical methods with arbitrary parameter adjustments classified as *envelope analysis*. In following years, already well-established cyclostationary processes to characterize communication signals started to be utilized as a more rigorous approach towards describing propeller tonals. The simultaneous and independent development in sampling theory, i.e., Compressive Sensing (CS), unlocked the opportunity to model the propeller tonals as a sparse vector to overcome the inefficient Nyquist-Shannon sampling theorem. Consequently, synchronous compression and sensing as well as high resolution localization of spatio-spectrally-sparse propeller information became practical. The main objective of this thesis is to investigate this practicality and propose useful and innovative detection estimation methods by exploiting the sparsity of the propeller tonals. It is important to emphasize that the intention of this thesis does not limit the possibility to utilize its findings in CS of general class of cyclostationary signals. Before defining the complete purpose, scope and contribution of this thesis it is essential to take a deeper look on cavitation noise, cyclostationary processes and CS to comprehend the motivation behind this work.

1.1 Propeller Cavitation Noise

Underwater acoustic signals fall broadly in two categories: natural and anthropogenic. Seismic activities, oceanic turbulence, surface waves, marine animals, precipitation and thermal agitation are among the main natural sources [1, Ch. 7]. Man-made noise

is typically due to shipping, marine construction, hydrocarbon production, geophysical surveys and military activities [2, Ch. 6]. Some of these sources produce signals with a stochastic nature which is the very reason they are called noise [3]. Ship-radiated noise is such an example and mainly a result of propeller revolution, propulsion or auxiliary machinery and hydrodynamic flow [1, Ch. 10].

Noise induced by propeller revolution can be due to non-cavitation [4] or cavitation [5,6]. Cavitation mainly occurs on the blade surface and tip of a rotating propeller leading to forming of vapor bubbles. The noise originates from the collapse of these bubbles in a random fashion causing a broadband noise spectrum. When cavitation develops, it quickly becomes the dominant noise source of a ship [4]. Moreover, rotating blades cause a modulation effect where the amplitude of the broadband noise is modulated at the blade pass¹ frequency as well as the propeller shaft rotation frequency when there are slight physical differences between the blades [7, Ch. 8]. This creates an idiosyncratic rhythmic broadband sound. This rhythm appears at multiple frequency components, also known as modulation [8] or propeller/cavitation [7, Ch. 8] [9,10] tonals.

Detection and estimation of the propeller tonals leads to determining the Propeller Shaft Rate (PSR), Blade Rate (BR), Number of Blades (NOB) and Number of Shafts (NOS), which is arguably the most decisive phase of water craft identification. Once acquired, this information paves the way to predicting the speed, even the type, of a vessel. The conventional methods for this task are based on the envelope analysis with the most renowned Detection of Envelope Modulation on Noise (DEMON) [8,11]–[14]. It is essentially based on the envelope detection of an Amplitude Modulation (AM) signal. However, as opposed to the sinusoidal wave in telecommunication AM processing, here, the carrier is the broadband propeller noise. Common practice in DEMON processing is firstly bandpass filtering then squaring and low-pass filtering the signal to acquire the propeller tonal spectrum. Bandpass filter refines the signal where cavitation is dominant, squaring yields the envelope signal, and low-pass filter returns the lower end of the envelope spectrum where the propeller

¹Moving of a single blade to the next blade's position.

tonals typically reside. Thus, the resulting spectrum is dependent on the arbitrary filter and processing parameters making DEMON largely empirical. Cyclostationary random processes promise a more meticulous approach toward this task via statistical signal processing tools.

1.2 Cyclostationary Random Processes

Cyclostationary random processes are first introduced in [15] for describing binary message pulse trains such as telegraph signals, which have periodically varying ensemble statistics. A more comprehensive characterization is given in [16], where cyclostationarity is defined over periodic mean and autocorrelation. More established definition, however, is that a signal is wide-sense cyclostationary of order n if and only if there is an n th-order nonlinear transformation that generates finite-amplitude periodic components. An equivalent description is through spectral correlation, i.e., a signal is wide-sense cyclostationary of order n if and only if time fluctuations in n spectral bands are statistically dependent such that they have nonzero joint n th-order moment [17, Ch. 1].

The order of nonlinear transformation determines the order of cyclostationarity. If the order is one, i.e., the nonlinear transformation is linear, then the signal is first-order cyclostationary [18]. This means that the signal itself has periodic components. These kind of signals do not demand a particular effort since the classical Fourier analysis suffices to extract the periodicity. Therefore, second–or higher–order cyclostationary signals are of concern when developing signal processing tools to characterize them. For example, analog and digital communication signals display cyclostationarity due to modulation [17, Ch. 1] where the message signal modulates the carrier yielding a periodic change in the energy of the signal, which is extracted via second-order transformations.

Another class of cyclostationary signals are due to machinery such as propellers, gears, fans and electrical motors, which exhibit periodic motion that modulates the vibration or noise they emanate [18]. Propeller cavitation noise treated as a second-order cyclostationary signal enabled a rigorous analysis and a statistical threshold for automatic detection of propeller tonals as presented in [19].

The energy-like functions obtained by simply squaring the signal is commonly adopted in practical cyclostationary signal processing. It is theoretically based on the second-order moments such as the autocorrelation function. While the Second-Order Statistics (SOS) is adequate to characterize most of the cyclostationary signals it might yield degraded performance when there is non-Gaussianity involved [17, Ch. 2]. Some signals may exhibit weak or no second-order cyclostationarity where higher-order cyclostationary moments and polyspectra may better describe their characteristics [20]. Ship-radiated propeller noise is such an example, where its non-Gaussian nature [21,22] enable the utilization of cyclostationary Higher-Order Statistics (HOS).

Another merit of cyclostationary processing reveals itself with its ability to represent the propeller tonals as spatio-spectrally-sparse vectors. This enables an efficient sampling scheme to exploit the sparsity in data compression and high-resolution spatial localization of cyclostationary propeller noise.

1.3 Compressive Sensing

CS, also known as compressed sensing [23] and compressive sampling [24], is a simultaneous data acquisition and compression technique exploiting the *sparsity* of the signal in an *incoherent* basis [23]–[27]. The number of samples needed to reconstruct the signal can be much smaller than its length. This is a remarkable improvement over the conventional principle of the Nyquist-Shannon sampling theorem, which states that representing a T -second-long continuous signal with a bandwidth of B Hz requires $N = 2BT$ samples [28].

A sparse signal² can be represented by a coefficient vector, which has much smaller nonzero entries compared to its size. For example, a discrete signal $\mathbf{x} \in \mathbb{C}^N$ consisting of $K \ll N$ sinusoidal components has K nonzero Fourier Series (FS) coefficients in the frequency-domain. Complex exponentials in the FS expansion constitute an orthonormal representation basis (or matrix) $\mathbf{F} \in \mathbb{C}^{N \times N}$ which enforces the sparsity on the signal $\mathbf{y} = \mathbf{F}\mathbf{x}$. Then, the sensing matrix $\mathbf{\Psi} \in \mathbb{R}^{M \times N}$ takes $M < N$ linear

²The terms signal and vector are used interchangeably. Lower case bold characters indicate vectors whereas matrices are represented by uppercase bold ones.

measurements $\mathbf{z} = \Psi\mathbf{y} = \Psi\mathbf{F}\mathbf{x}$ provided that the sensing and representation matrices are sufficiently incoherent. In other words, the largest correlation between the vectors of these matrices dictates the required number of measurements to be able to fully recover the sparse signal [24]. Additionally, the measurement process is non-adaptive, i.e., the sensing matrix is fixed and do not alter between measurements [29].

To construct efficient sensing matrices one relies on several properties among which the Restricted Isometry Property (RIP) is the strongest condition [29]. When RIP holds for Ψ , the Euclidean distance between any pair of K -sparse vectors are preserved, which in turn implies that K -sparse vectors cannot be in the null space of Ψ [30]. This is extremely useful in recovering the sparse vector $\hat{\mathbf{y}}$ from noisy measurements $\mathbf{z} = \Psi\mathbf{y} + \mathbf{e}$ in real-world applications. Random matrices with entries drawn from independent identically distributed (i.i.d.) sub-Gaussian (including Gaussian) distributions satisfy the RIP with high probability. Moreover, if Ψ is constructed using a Gaussian distribution then $\Psi\mathbf{F}$ is also Gaussian since \mathbf{F} is an orthonormal basis. This means that $\Psi\mathbf{F}$ can also satisfy the RIP when M is sufficiently large [29].

Sparse approximation can be executed via several computational techniques among which the convex optimization and greedy pursuits are the most commonly utilized [31]. The nonconvex optimization is defined by minimizing an ℓ_p norm of the sparse vector $\hat{\mathbf{y}}$, e.g., $\|\hat{\mathbf{y}}\|_p$, with $0 < p < 1$ which is an intractable problem [23]. In the extreme case, $p \rightarrow 0$, the ℓ_0 pseudo-norm requires a combinatorial optimization, i.e., searching all the sparse subsets of $\{1, 2, \dots, N\}$ for a solution [23]. However, when ℓ_0 gives a sparse solution then ℓ_1 provides the same unique solution [23]. This enables a tractable sparse recovery problem by relaxation of ℓ_0 to its convex counterpart ℓ_1 , e.g., minimizing $\|\hat{\mathbf{y}}\|_1$ subject to $\|\Psi\hat{\mathbf{y}} - \mathbf{z}\|_2 < \varepsilon$ with ε being the maximum allowed norm of the noise. Greedy pursuit methods are faster alternatives to convex optimization with similar recovery guarantees for ultra sparse vectors and lesser noise [31]. The recovery problem can be rewritten in reverse as minimizing $\|\Psi\hat{\mathbf{y}} - \mathbf{z}\|_2$ subject to $\|\hat{\mathbf{y}}\|_1 < K$.

CS has emerged as an efficient sampling scheme. However, it can also be utilized to solve underdetermined system of equations. Such problems occur in numerous

applications, one of which is the Direction-of-Arrival (DOA) Estimation. One of the goals in DOA estimation is to find the azimuth angle of an impinging wave on an array of sensors. Generally, the number of sensors M are much less than the number of possible angles of the source N . This is modeled by a linear system of equations where the so-called array manifold matrix \mathbf{A} is formed by steering vectors looking at different angles and each representing the phase shifts (or time delays) at each sensor. Then this matrix is multiplied with a K -sparse³ source vector \mathbf{y} where each row represents the signal at a certain angle with additive noise \mathbf{e} . Apparently, the DOA estimation equations $\mathbf{z} = \mathbf{A}\mathbf{y} + \mathbf{e}$ are the same as the CS measurements. This reveals the question whether one can utilize a sparse recovery approach to exploit the sparsity of \mathbf{y} for localization of the sources. The answer is positive and there is a matured literature on this subject with a generally accepted name, *compressive beamforming* [32]–[49]. Here, the array manifold matrix acts as a deterministic sensing matrix, which might violate the RIP that is easily satisfied by random matrices. Conveniently, there is a measure closely related to the RIP known as coherence that can be used to assess the fitness of the array manifold matrix as a sensing matrix. The maximum inner product between the column vectors of \mathbf{A} yields the coherence. The smaller its value the easier \mathbf{A} satisfies the RIP for K -sparse vectors.

1.4 Purpose and Scope of the Thesis

Underwater acoustic signal processing or in particular sonar signal processing mainly consists of target detection, localization and identification stages [50,51]. Conventional systems depend on Nyquist-rate samples to process multiple hydrophone signals in order to extract information on the existence, whereabouts and acoustic signatures of water crafts. These signals are essentially of broadband (stationary or cyclostationary) and narrowband (periodic) nature. While cyclostationary and periodic (first-order cyclostationary) parts of these signals can be represented by sparse vectors, the stationary part lacks sparsity and therefore must be reliant to Nyquist sampling scheme. The periodic part, mainly due to intermittent or continuous sources, has a theoretical

³In DOA estimation applications there are usually much fewer sources than the possible angles.

sparsity unless the broadband noise overwhelms the spectrum. However, the usual case is that the Fourier spectra are not sparse enough to employ CS.

Having defined the constraints on the signal of interest, this thesis investigates an efficient sampling scheme to detect and localize water crafts with cyclostationary signatures [52]–[54]. The signal model is based on AM [8,13,55]–[60] where the deterministic envelope is formed by a single propeller tonal with a certain cyclic frequency. The carrier is assumed to be a stationary random process representing the broadband propeller noise.

The first investigation is on the representation of the spectral sparsity of this signal model using the second-order Spectral Correlation Function (SCF) [61]. There is a fast and reliable Fourier-based estimator of the SCF, e.g., Cyclic Modulation Spectrum (CMS) [18] for developing a linear and non-adaptive measurement model. Cyclic Modulation Coherence (CMC) [19] better describes cyclostationarity due to its independence from the spectral slope. Furthermore, Integrated CMC (ICMC) enables both automatic detection of propeller tonals and maximization of the sparsity. These cyclostationary processing tools allow to form a CS scheme to compress propeller tonal information [52]. The next questions are the sparse recovery of these tonals and the comparison of the detection performances of Nyquist-rate and recovered ICMC. Greedy methods known as Iterative Hard Thresholding (IHT) [62] and Compressive Sampling Matching Pursuit (CoSaMP) [63] are investigated for this recovery.

Another research question arises from the statistical properties of the cavitation noise. It is demonstrated that the ship-radiated propeller noise exhibits non-Gaussian characteristics [21,22]. This leads to the examination of the higher-order cyclic bispectrum [64] of the AM model for the sparsity of propeller tonals. Then, the Cyclic Modulation Bispectrum (CMBS) [53] as an estimator of the Cyclic Bispectrum (CBS) might prove useful for representing the cyclostationarity as well as building a CS scheme. Similar to CMC and ICMC, Cyclic Modulation Bicoherence (CMBC) and Integrated CMBC (ICMBC) can be used to maximize the cyclostationarity, hence the sparsity.

Finally, a DOA estimator based on CS and cyclostationary beamforming is studied for high resolution localization of cavitation noise. Cyclic Compressive Beamformer (CCB) [54] reveals an advantageous situation in DOA estimation if the sources are cyclostationary. Since there are numerous powerful DOA estimation methods with stationary source assumption it is essential to determine the statistical performance of the CCB for comparison purposes. The comparison covers extensive signal and array parameters such as the modulation index, signal-to-noise ratio, number of sources (sparsity), number of sensors (compressive samples) and angle difference between sources.

The methods inherited and proposed in this thesis can be utilized for general class of sparse cyclostationary signals, which are encountered in areas such as telecommunications [65]–[67], time-frequency analysis [68,69], radar [70] and machine diagnostics [18]. Interested readers can find a survey in [71] on recent advances in cyclostationarity and its use in CS. However, the scope of this thesis excludes these applications, which have their own literature.

1.5 Contribution of the Thesis

This thesis investigates the compression and localization of cyclostationary information by exemplifying propeller cavitation noise as an AM model. However, CS and cyclostationary tools inherited and developed in this thesis can be used in many areas involving CS of second—or higher—order cyclostationary statistics. Telecommunication [72] and mechanical [18] signals are such good examples where their cyclostationarity and sparsity make them eligible for the compression and localization of the information they convey. Having asserted that, the main contributions of this thesis are:

- 1) the demonstration that the SCF of the AM signal model is sparse,
- 2) the derivation of a linear measurement model that maps the Nyquist-rate CMS into the compressive one,
- 3) the sparse approximation of the Nyquist-rate CMS with IHT and CoSaMP,

- 4) the comparison of the detection capabilities of the Nyquist-rate and recovered samples through the ICMC,
- 5) the derivation of cyclic bispectrum and the demonstration of its sparsity in cyclic frequency domain,
- 6) the proposal of CMBC for robust detection of the higher-order cyclostationarity and a CS scheme using CMBS,
- 7) comparison of ICMC and ICMBC for both Nyquist-rate and recovered cases,
- 8) the proposal of a novel method for DOA estimation of second-order cyclostationary sources,
- 9) the analytical derivation of the Mean Square Error (MSE) of CCB,
- 10) the performance comparison of classical and compressive DOA estimators.

The body of this dissertation constitutes of three journal papers that are either published or submitted. Chapter 2 is based on the paper [52] on CS of CMS and detecting second-order cyclostationarity. Chapter 3 is based on the paper [53] on CMBS for higher-order representation and CS of propeller tonals. Chapter 4 is based on the paper [54] on CS for cyclostationary DOA estimation. Chapter 5 concludes the thesis and gives recommendations for possible research directions.

2. COMPRESSIVE SENSING FOR CYCLOSTATIONARY DETECTION

2.1 Introduction

Ship-radiated noise mainly consists of a broadband part induced by the propeller revolution and a narrowband part (machinery tonals) generated by the propulsion and auxiliary machinery represented in Fig. 2.1 [1, Ch. 10] [7, Ch. 8, Ch. 10]. Amplitude of the broadband part is modulated as a consequence of the propeller revolution when it exceeds a certain rate [7, Ch. 8]. The physical phenomena causing this, is known as cavitation which leads to generation of bubbles around the propeller that collapse and create the broadband noise [7, Ch. 7]. Note that, revolution of the propeller shaft and blades creates a periodic signal yielding the propeller (or cavitation) tonals. Given the PSR and the BR one can obtain the NOB, i.e., $(NOB) = (BR) \div (PSR)$. Detection of these components is arguably the most important stage of sonar target classification since the typical values of PSR, BR and NOB are distinguishable for various ship categories [12,55,73]–[76]. These acoustic signatures emanating from nearby ships are acquired by hydrophones existing in multiple numbers for acoustical monitoring or beamforming which causes vast data sizes. Moreover, broadband propeller noise may range up to 100 kHz [7, Ch. 8] which increases the required sampling rate and hence the data size further. This acquisition scheme negatively affects the energy efficiency, hardware complexity and storage capacity [50, Ch. 6].

CS has emerged to mitigate the inefficiency in sampling sparse signals. It has made the simultaneous data acquisition and compression possible when the signal under consideration has a sparse representation in a known incoherent basis [23]–[25,30,77,78]. Then a suitable sparse approximation method can recover the

This chapter is based on the paper “U. Fırat and T. Akgül, Compressive Sensing for Detecting Ships With Second-Order Cyclostationary Signatures, in IEEE Journal of Oceanic Engineering, vol. 43, no. 4, pp. 1086-1098, Oct. 2018, doi: 10.1109/JOE.2017.2740698.”

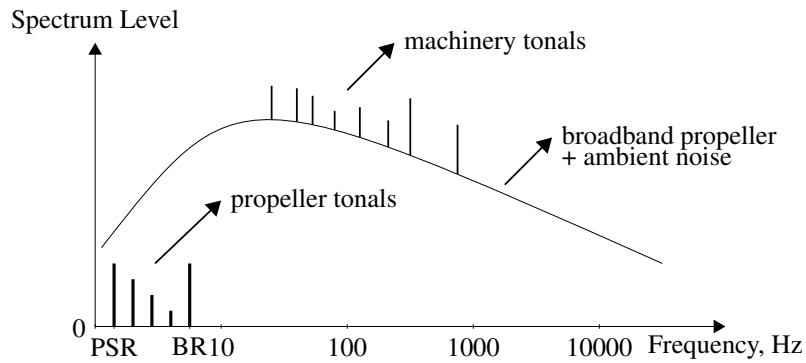


Figure 2.1 : Representative ship-radiated noise spectrum with the additive ambient noise.

Nyquist-rate signal with high probability from linear and nonadaptive sub-Nyquist-rate measurements [31,62,63,79,80].

The dense support in frequency, explicitly seen in Fig. 2.1, violates the sparsity requirement for CS to be applicable directly on the ship-radiated noise as well as on propeller tonals due to the ambient noise dominance in the low frequency region. However CS is possible if the problem can be formulated to acquire the propeller tonals in a suitable manner. For that, a function representing the inherent sparsity of propeller tonals and a basis that maps the Nyquist-rate samples of this function into the compressive ones must be found. In this thesis, we propose such a scheme for CS and sparse recovery of propeller tonals to detect ships. We employ two well-known pursuit methods which are the so-called IHT and CoSaMP.

Note that, detection (and classification) of propeller noise modulation involves estimating the second-order statistics, e.g., power spectrum of propeller tonals, rather than the time-domain representation of the modulating signal itself. CS on this kind of problems, i.e., on random processes, has recently gained a considerable attraction. Authors of [65] utilize CS in wide-band spectrum sensing for detecting the cyclic features of digitally modulated communication signals with fewer samples. They proposed an approach to linearize the relationship between the SCF estimate of the Nyquist-rate and compressive measurements to apply a convex optimization method for sparse approximation. In [69], authors proposed a CS approach for approximately Time-Frequency (TF) sparse nonstationary random processes applied not directly on the process realizations but on an estimate of a TF autocorrelation function, i.e.,

Expected Ambiguity Function (EAF). This enables a somehow twofold compression from the observed signal to EAF and then to compressive EAF. Another TF approach is introduced in [68] for the deterministic case where authors exploited the sparsity of chirp signals in TF plane and proposed a new technique to capture sharply localized TF distributions in the case of multicomponent amplitude and frequency modulated signals. Interested readers may find a comprehensive review on CS applications that involve second-order statistics, i.e., *compressive covariance sensing*, in [67].

In sonar signal processing, the most recognized approach to recover the propeller tonals is the so-called DEMON [8,12,13,56]–[60,75,81]. In short, this method obtains the modulating signal by squaring and then low pass filtering the propeller noise, i.e., extracting its envelope. There are several other methods to estimate the propeller tonals relying on maximum likelihood estimation [13,59,82] and empirical mode decomposition [57,58]. There are also studies tackling various challenging problems which occur due to the physical nature of the environment, e.g., effects of the ship roll and pitch [56], impulsive characteristics of the ship-radiated noise [60] and overlapped observations caused by multipath propagation [55]. Former two papers employ DEMON while the latter one suggest cyclostationary processing which is a well-established area in investigating several types of modulation schemes. It can be more parsimonious, permits the analysis of time varying systems and does not suffer from spectral overlaps as other above mentioned methods do [17, Ch. 1].

In this thesis, we employ the cyclostationary approach relying on these properties. However the main reason that we utilize this approach is the convenience in representing the inherent sparsity of propeller tonals and deriving a linear measurement model for CS to be applicable. We show that the amplitude modulated propeller noise exhibits second order cyclostationarity, i.e., its autocorrelation function is periodic in its time index. This causes a sparse SCF which gives us the motivation to apply CS on ship-radiated propeller noise. Then we derive a measurement model based on the CMS [18], i.e., an SCF approximation that allows matrix representations required to manifest the linear relationship between the Nyquist-rate and compressive CMS. Furthermore, CMC [19], being the normalized CMS, allows near optimal detection by mitigating the scaling effect of the coloredness of ship-radiated noise seen in Fig.

2.1. For that, we employ ICMC which allows the integration of a spectral band where cavitation dominates, thus provides a better statistical detection scheme and can be used in imposing the sparsity constraint in sparse approximation.

To summarize, our main contributions are

- 1) the demonstration that the SCF of the amplitude modulated propeller noise is sparse,
- 2) the derivation of a linear measurement model that maps the Nyquist-rate CMS into the compressive one,
- 3) the sparse approximation of the Nyquist-rate CMS with IHT and CoSaMP and
- 4) the comparison of the detection capabilities of the Nyquist-rate and recovered samples through the ICMC.

The remainder of this chapter is as follows: We give the propeller noise measurement model and cyclostationary processing tools in the next section. In Section 2.3 we give a brief introduction to CS and show how to exploit the sparsity of the SCF in the CS scheme by utilizing the CMS. Examples on the synthetic and real-world data for the recovery and detection of propeller tonals are presented in Section 2.4. General discussion on the assumptions and results as well as possible future directions are given in Section 2.5.

2.2 Cyclostationary Propeller Noise

In this section, we give a propeller noise measurement model, derive the SCF of this model and show its sparsity. We also give the definition of CMS [18] as an SCF approximation and CMC [19] as the normalized CMS recently introduced for detection of ships with cyclostationary signatures.

2.2.1 Propeller noise measurement model

In order to derive the SCF in a simple manner, we consider the modulating signal as a single sinusoid representing the BR component. Note that it is straightforward to

generalize the problem when there are multiple tonals. We also assume that the signal is sensed in far field with the additive ambient noise and without any multipath effect.

Under these assumptions we can write the propeller noise measurement model as

$$x(t) = [1 + \mu a_0 \cos(\alpha_0 t)]c(t) + v(t) \quad (2.1)$$

where $[1 + \mu a_0 \cos(\alpha_0 t)]c(t)$ is the propeller noise and $v(t)$ is the ambient noise. The signal $[1 + \mu a_0 \cos(\alpha_0 t)]$, also known as the envelope in communications literature, modulates the amplitude of the broadband propeller noise $c(t)$ with the modulation index μ [8]. The amplitude and the frequency of the BR component are a_0 and α_0 rad/s, respectively.

Despite being an idealized model, (2.1) reflects the amplitude modulation induced by cavitation and is highly accepted by the signal processing community conducting research on propeller tonals [8,13,55]–[60].

2.2.2 Sparsity of the SCF

Before deriving the SCF of $x(t)$ to show its sparsity we need to make the following assumptions: 1) The modulating signal is deterministic, 2) $c(t)$ and $v(t)$ are uncorrelated [8,11,13,59,82], zero-mean wide-sense stationary [8,11,13,19,59,83,84] random processes. Using (2.1), we can write the autocorrelation function of $x(t)$ as

$$\begin{aligned} R_x(t, s) &\triangleq \mathbb{E}\{x(t)x(s)\} \\ &= \left[1 + \frac{\mu a_0}{2} e^{j\alpha_0 t} e^{-j\alpha_0 \tau} + \frac{\mu a_0}{2} e^{-j\alpha_0 t} e^{j\alpha_0 \tau} \right. \\ &\quad + \frac{\mu a_0}{2} e^{j\alpha_0 t} + \frac{\mu a_0}{2} e^{-j\alpha_0 t} \\ &\quad + \frac{\mu^2 a_0^2}{4} e^{j2\alpha_0 t} e^{-j\alpha_0 \tau} + \frac{\mu^2 a_0^2}{4} e^{-j2\alpha_0 t} e^{j\alpha_0 \tau} \\ &\quad \left. + \frac{\mu^2 a_0^2}{4} e^{j\alpha_0 \tau} + \frac{\mu^2 a_0^2}{4} e^{-j\alpha_0 \tau} \right] R_c(\tau) + R_v(\tau) \\ &= R_x(t, \tau) \end{aligned} \quad (2.2)$$

where $\mathbb{E}\{\cdot\}$ is the expected value operator and $\tau = t - s$. The derivation of $R_x(t, s)$ is given in Appendix A. Note that $x(t)$ is nonstationary, i.e., $R_x(t, s) = R_x(t, \tau)$ depends

both on the time index t and the lag τ . However, $R_x(t, \tau) = R_x(t + nT, \tau)$, thus $x(t)$ is cyclostationary (periodically stationary) with the period $T = 2\pi/\alpha_0$ sec and $n \in \mathbb{Z}$. Since the periodicity is in the second order autocorrelation function, $x(t)$ is said to be second order wide-sense cyclostationary.

Cyclostationary random processes have been investigated widely in the literature, especially in communications and signal processing [17,18]. Fig. 2.2 shows useful relations of random processes in their second-order statistics where $R_x(t, \tau)$ has FS relation with the cyclic autocorrelation function $C_x(\alpha, \tau)$ and Fourier Transform (FT) relation with the Wigner-Ville distribution $W_x(t, \beta)$. Here, α and β are the cyclic and spectral frequency variables, respectively. The SCF $S_x(\alpha, \beta)$ has FS relation with $W_x(t, \beta)$ and FT relation with $C_x(\alpha, \tau)$. Clearly, $C_x(\alpha, \tau)$ boils down to the classical autocorrelation function and $S_x(\alpha, \beta)$ to the classical Power Spectral Density (PSD) when there is no cyclostationarity ($\alpha = 0$).

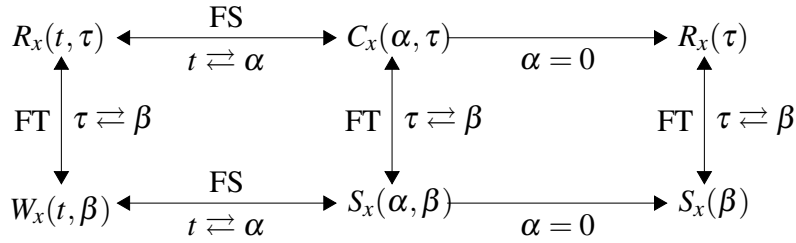


Figure 2.2 : Relations between second-order statistics.

To show the sparsity of the propeller noise explicitly, we can use these relations to calculate the spectral counterpart of $R_x(t, \tau)$ in both its variables t and τ . We can then write the SCF of $x(t)$ as

$$\begin{aligned}
S_x(\alpha, \beta) = & \left\{ S_c(\beta) + \frac{\mu^2 a_0^2}{4} [S_c(\beta - \alpha_0) \right. \\
& \left. + S_c(\beta + \alpha_0)] + S_v(\beta) \right\} \delta(\alpha) \\
& + \frac{\mu a_0}{2} [S_c(\beta + \alpha_0) + S_c(\beta)] \delta(\alpha - \alpha_0) \\
& + \frac{\mu a_0}{2} [S_c(\beta - \alpha_0) + S_c(\beta)] \delta(\alpha + \alpha_0) \\
& + \frac{\mu^2 a_0^2}{4} S_c(\beta + \alpha_0) \delta(\alpha - 2\alpha_0) \\
& + \frac{\mu^2 a_0^2}{4} S_c(\beta - \alpha_0) \delta(\alpha + 2\alpha_0)
\end{aligned} \tag{2.3}$$

where $S_c(\beta)$ and $S_v(\beta)$ are the FTs of $R_c(\tau)$ and $R_v(\tau)$, respectively; $\delta(\cdot)$ is the Dirac operator (again see Appendix A).

By inspecting the spectral support of (2.3) shown in Fig. 2.3 one can see the sparsity of the propeller noise appearing in the cyclic frequency α due to the modulating signal while the broadband propeller noise causes a dense support in the spectral frequency β . One can get the BR component by setting $\alpha = \alpha_0$ in (2.3), i.e.,

$$S_x(\alpha_0, \beta) = \frac{\mu a_0}{2} \left[S_c(\beta + \alpha_0) + S_c(\beta) \right] \delta(\alpha - \alpha_0). \quad (2.4)$$

Note that, the magnitude of the BR component grows with increasing modulation index, BR amplitude and broadband propeller noise PSD. This growth does not affect the theoretical sparsity of the SCF, i.e., sparsity implies that the number of nonzero components of a signal (here, the SCF) is much lower than the signal size. It does not suggest anything related to the values of this components. However, this growth becomes crucial in practical applications where the stationarity assumption collapses due to finite signal observations as well as nonstationary nature of the ambient and propeller noise. We mention about this in detail in next sections.

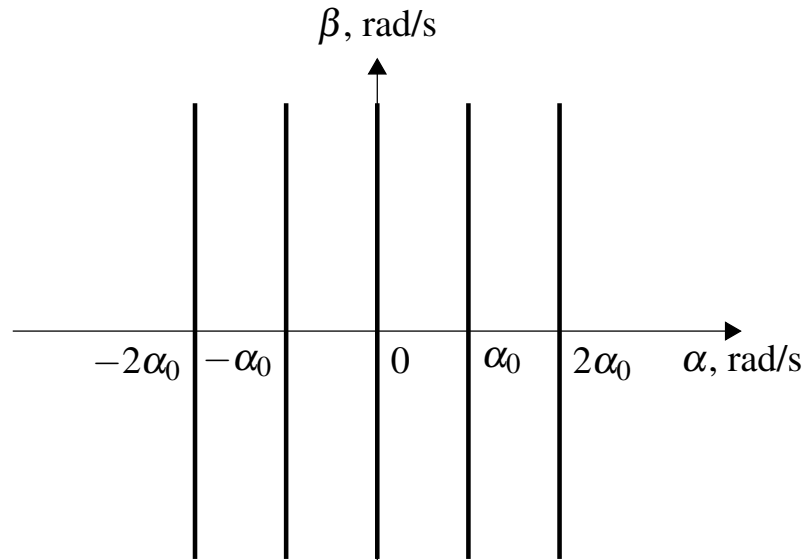


Figure 2.3 : Spectral support of the SCF of the propeller noise model given in (2.1).

SCF contains the essential information about the propeller tonals for which we seek a CS scheme. However, estimating the SCF can be a cumbersome task since the

real-world measurements are of finite length. At this point CMS offers a fast and reliable approximation of the SCF relying only on Discrete FT (DFT) which allows us to employ matrix operations in developing a CS scheme. Note that, the scope of this thesis includes neither the discussion of possible SCF estimators nor the optimality of the CMS. Thus, we merely focus on employing the CMS in CS.

2.2.3 Cyclic modulation spectrum

Let $x[l] \triangleq x(lT_s), l = 0, \dots, D - 1$, be the D -long signal which is the discretized counterpart of $x(t)$ given in (2.1) with the sampling frequency of $f_s = 1/T_s$. An L -long analysis window $w[l]$ is used to take overlapped snapshots from the signal yielding $N = \lfloor \frac{D-L}{V} \rfloor + 1$ snapshots where V is the shifting size. Then the short-time DFT of the windowed signal can be calculated as

$$X_{\Delta\beta}(t_n, \beta) = T_s \sum_{l=nV}^{nV+L-1} x[l]w[l-nV]e^{-j\beta lT_s} \quad (2.5)$$

which returns the filtered signal in a narrow band with center frequency β and width $\Delta\beta \sim 2\pi/LT_s$ at times $t_n = nVT_s, n = 0, \dots, N - 1$ [19]. By taking the DFT of the $|X_{\Delta\beta}(t_n, \beta)|^2$ over its time variable that transforms t_n to its dual cyclic frequency variable α we arrive at the CMS given as

$$P_x(\alpha, \beta) = \frac{1}{N} \sum_{n=0}^{N-1} |X_{\Delta\beta}(t_n, \beta)|^2 e^{-j\alpha t_n} \quad (2.6)$$

which is basically the DFT of the spectrogram of the signal. Here, the spectral and cyclic frequency resolutions are $\Delta\beta$ and $\Delta\alpha \sim 2\pi/DT_s$, respectively [19]. Note that, the maximum cyclic frequency cannot exceed $\Delta\beta$ rad/s by the uncertainty principle, i.e., $\Delta T \Delta\beta \geq 1$ where the time resolution is $\Delta T = 1/\alpha$. Interested readers may refer to [18] for cyclostationarity in general as well as the properties of CMS.

Fig. 2.4 shows a segment of an actual noise recorded with the so-called Bosphorus Ambient Noise Acquisition System (BANAS) in the Strait of Istanbul along with its CMS calculated using a ten-second-long measurement where $f_s = 50$ kHz, $L = 256$, $V = 64$ (75% overlap) [85]. We observe that CMS clearly affirms the existence of cyclostationarity due to its nonzero values appearing for $\alpha \neq 0$ where a stationary

signal expected to yield nothing. There are some distinguishable propeller tonals which seems to belong to a ship of opportunity. Note the dominance of a presumable PSR of 1 Hz approximately between 4 – 17 kHz. Note also the existence of a possible BR of 4.2 Hz and some harmonic components at 8.4 Hz, 12.3 and 16.4 Hz, respectively.

On the other hand, it is hard to distinguish the propeller tonals along the cyclic frequency dimension especially in the lower spectral frequency region under a few kilohertz presumably due to the highly nonstationary nature of the real-world ambient noise. Note that, the recording site is a narrow and shallow strait with a heavy ship traffic [85] which contributes to the low frequency ambient noise. Thus, the nonstationarity of the ambient noise increases when this heavy traffic noise meets with this highly reverberant environment. We revisit this effect in imposing the sparsity required in the CS scheme we propose in the next section.

While CMS has the ability to reveal the cyclostationarity it also reflects the coloredness of measured noise as explicit in its spectral frequency dimension in Fig. 2.4. However, determination of cyclostationarity involves the detection of a periodicity rather than the energy level in a specific spectral band. Therefore, authors of [19] suggest a more suitable quantity, i.e., CMC, which we now briefly mention about.

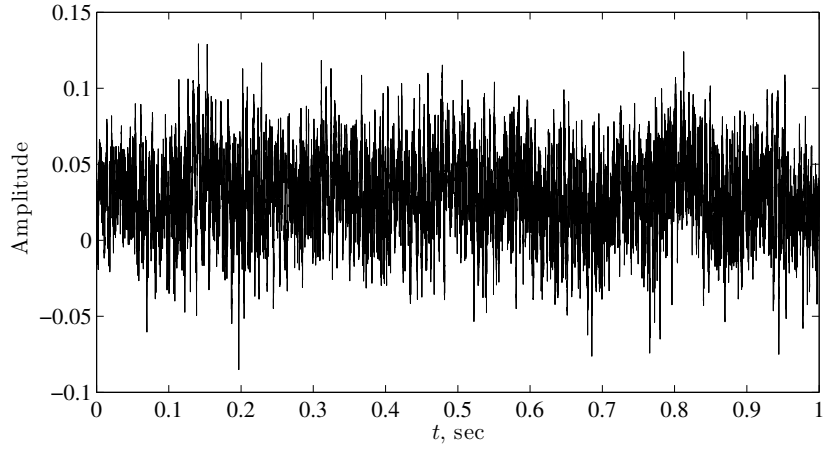
2.2.4 Cyclic modulation coherence

Since the propeller noise exhibits coloredness as seen in Fig. 2.1 normalizing it to mitigate the spectral scaling effects enables easier investigation of the cyclostationarity, e.g., as in the spectral support given in Fig. 2.3. The so-called CMC defined as

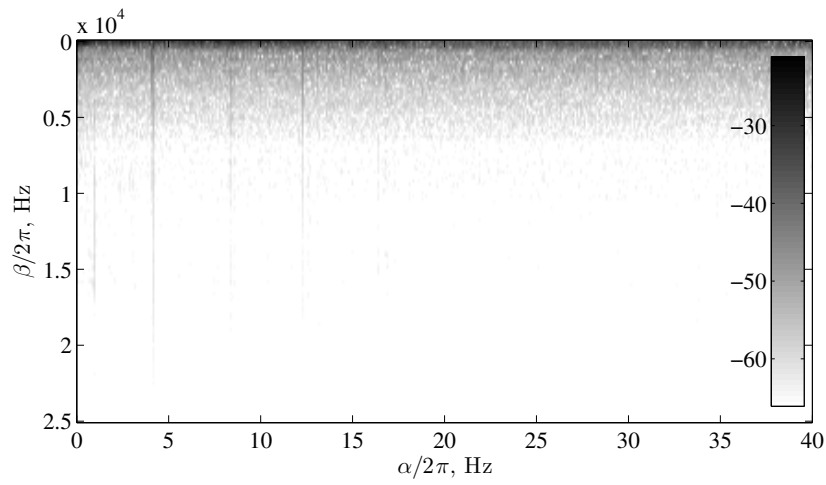
$$G_x(\alpha, \beta) = \frac{P_x(\alpha, \beta)}{P_x(0, \beta)} \quad (2.7)$$

serves to this objective [19]. Notice that, $P_x(0, \beta)$ is the averaged periodogram estimate of the PSD of the windowed signal.

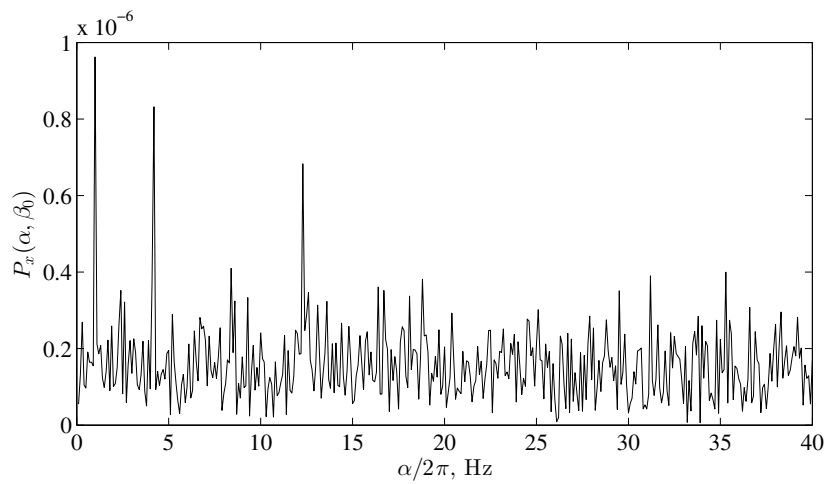
Additionally, CMC has an advantage when used as a detection statistic because of the normalization serving as a spectral whitening. Hence, one can avoid the miss of the cyclostationarity which might be caused by a low energy level in a specific band. Furthermore, integrating the CMC over the spectral band where cavitation, hence



(a)



(b)



(c)

Figure 2.4 : Actual radiated-noise of a ship of opportunity with additive ambient noise measured with BANAS in the Strait of Istanbul a) its one-second-long segment, b) its CMS (in dB scale due to extreme variation in the spectral frequency dimension), c) its CMS at $\beta_0 = 10\text{kHz}$ (in linear scale).

cyclostationarity dominates, one may obtain a better Signal-to-Noise Ratio (SNR) at detection due to the suppression of unwanted nonstationary noise. ICMC is defined in [19] as

$$g_x(\alpha) = \frac{1}{B} \sum_{i=i_1}^{i_2} |G_x(\alpha, \beta_i)|^2 \quad (2.8)$$

where i_1 and i_2 are the spectral frequency indices which define the band with $B = i_2 - i_1 + 1$.

Authors of [19] further proposed a statistical test comparing the ICMC with a statistical threshold obtained by

$$\lambda_{1-p}(\alpha) = \frac{\sigma^2(\alpha)}{2B} \chi_{1-p, 2B}^2 \quad (2.9)$$

where

$$\sigma^2(\alpha) = \frac{1}{VN} \sum_{l=1-L}^{L-1} \left| \sum_{n=\max(0,l)}^{\min(L-1, L-1+l)} w[n]w[n-l] \right|^2 \cos(\alpha_0 l) \quad (2.10)$$

is the variance of CMC and $\chi_{1-p, 2B}^2$ is the $100(1-p)$ percentile of the χ_{2B}^2 distribution with $2B$ degrees of freedom. Then the resulting statistical test reads:

- Reject the null hypothesis H_0 "there is no presence of cyclostationarity at cyclic frequency α " at the p level of significance if

$$g_x(\alpha) > \lambda_{1-p}(\alpha). \quad (2.11)$$

They further defined a detection SNR to exhibit the significance of the detection as

$$\frac{g_x(\alpha_0)}{\lambda_{1-p}(\alpha_0)} \quad (2.12)$$

at the cyclic frequency, α_0 . We employ this statistical test in Section 2.4 to compare the detection capability of the Nyquist-rate ICMC with the ICMC recovered from the compressive samples.

Now let us return to analyzing the actual ship radiated noise of Fig. 2.4. CMC and ICMC given in Fig. 2.5 reveal more information on the cyclostationarity. Note that,

by normalizing $P_x(\alpha, \beta)$ with the PSD estimate $P_x(0, \beta)$ we have a cleaner picture in terms of observing the cyclostationarity. Also note that, the effect of nonstationarity, due to presumably heavy ship traffic, diminishes after normalization.

In addition to the previous comments on the propeller tonals of Fig. 2.4, we can now clearly see them independent of the spectral energy they convey. Compared to the CMS, PSR is distinguishable also between the 21 – 25 kHz band. Furthermore, one can explicitly see the harmonic components at 12.6 Hz and 16.8 Hz in addition to the ones observed in CMS. This might mean that the ship has two propeller shafts rotating at different speeds thus creating slightly different PSRs which cause these additional components. We revisit this real-world example in Section 2.4.

Normalization of CMS does not only provide a better picture in terms of detecting cyclostationarity but also give us an idea about where to look for the sparsity to impose in sparse approximation procedure. ICMC seems to be such a function for this requirement as we demonstrate in the next section.

2.3 Compressive Sensing

CS has made it possible for a discrete-time signal to be sensed compressively and reconstructed perfectly with high probability from its samples acquired below the Nyquist-rate [23,25,30,77]. CS works under two conditions, *sparsity* and *incoherence*: *i*) sparsity is translated as the signal depending on a number of degrees of freedom which is comparably much smaller than its finite length; *ii*) incoherence implies that the basis which maps the signal to compressive observations should be sufficiently incoherent [30].

Sparsity is a strong condition for many real-world signals due to the additive noise and dense representation bases. A more realistic term would be compressibility where the signals have coefficients that, when sorted, decay according to a power law. In this thesis, we use the sparsity and compressibility interchangeably.

Now let us mention briefly about the sparse approximation problem, also known as sparse coding or sparse recovery in the literature.

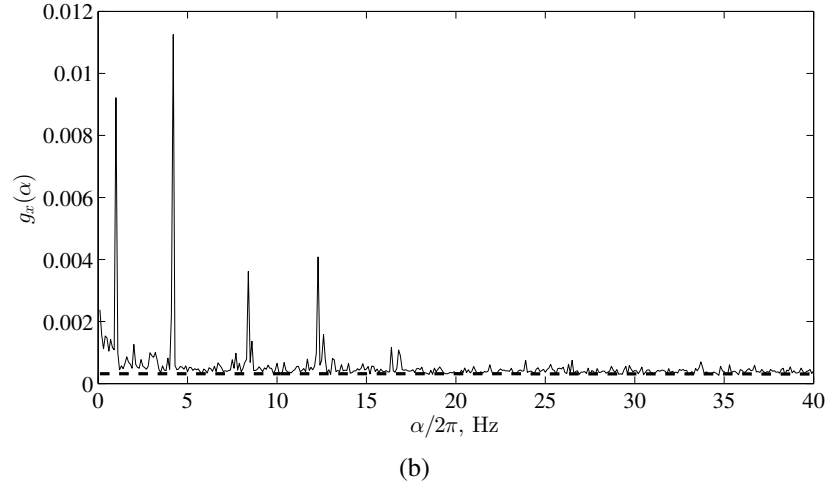
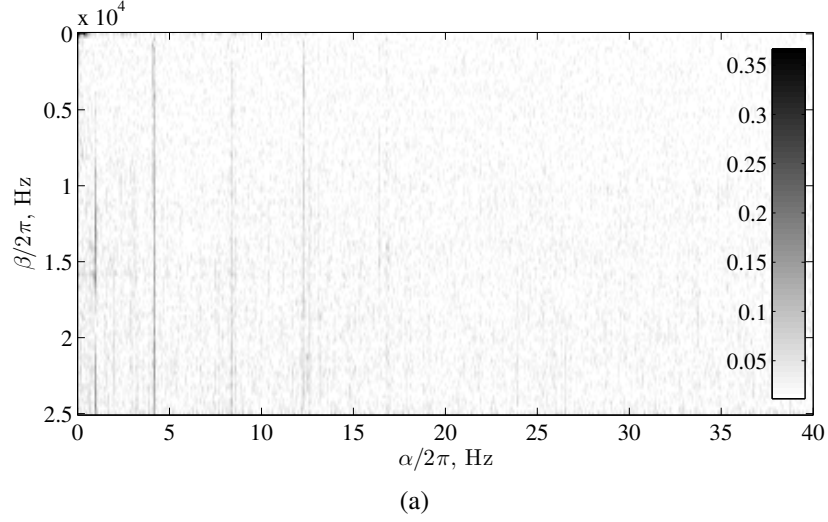


Figure 2.5 : a) CMC (in linear scale) corresponding to CMS of Fig. 2.4, b) ICMC integrated along all the spectral band together with the statistical threshold (dotted line), $\text{DSNR} = 112$ (see (2.27) for the definition of DSNR), $p = 0.001$.

2.3.1 Sparse approximation

The objective of sparse approximation is to recover a signal which is sparse/compressible itself or with respect to a redundant frame. Given the measured signal $\mathbf{y} \in \mathbb{R}^M$, the measurement matrix $\Psi \in \mathbb{R}^{M \times N}$ and the sparse signal $\mathbf{x} \in \mathbb{R}^N$ with $M < N$, we can write the (noisy) sparse approximation problem as

$$\min_{\mathbf{x}} \|\mathbf{x}\|_0 \quad \text{subject to} \quad \|\mathbf{y} - \Psi\mathbf{x}\|_2 \leq \varepsilon \quad (2.13)$$

where $\|\cdot\|_0$ is the ℓ_0 norm operator and $\varepsilon > 0$ is the error tolerance [31]. The noisy sparse approximation in (2.13) can be reformulated as

$$\min_{\mathbf{x}} \|\mathbf{y} - \Psi\mathbf{x}\|_2 \quad \text{subject to} \quad \|\mathbf{x}\|_0 \leq K \quad (2.14)$$

where K is the signal sparsity to be sought for.

The signal \mathbf{x} itself can be sparse or can be sparse in a basis, i.e., $\mathbf{x} = \Phi\mathbf{s}$ with $\mathbf{s} \in \mathbb{R}^N$ being the sparse vector of ones and zeros. $\Phi \in \mathbb{R}^{N \times N}$ can be an orthonormal basis depending on the application.

Among several approaches for sparse approximation, convex optimization and greedy pursuits are the ones most commonly utilized. The problems in (2.13) and (2.14) are Non-deterministic Polynomial-time (NP) hard (NP-hard) problems. By relaxing the combinatorial ℓ_0 pseudo-norm to its closest convex counterpart ℓ_1 norm, the NP-hard problem reduces to a tractable one which can be solved by convex optimization methods [31]. However, we choose to apply the pursuit methods due to their ease of use and speed.

One of the simplest greedy methods is the Orthogonal Matching Pursuit (OMP) that iteratively updates the estimate for the sparse signal \mathbf{x} by measuring the correlation between the columns of the measurement matrix Ψ and the residual $\mathbf{r} = \mathbf{y} - \Psi'\hat{\mathbf{x}}$ and solving the least squares problem $\hat{\mathbf{x}} = \arg \min_{\mathbf{x}'} \|\mathbf{y} - \Psi'\mathbf{x}'\|_2$ where Ψ' is the matrix composed of the most correlated single columns found at each iteration [31]. Stopping criterion can be $\|\mathbf{r}\|_2 \leq \varepsilon$ if the problem is defined as in (2.13) or after K iterations if as in (2.14). While the former prioritize the minimization of the estimation error, the latter looks for the sparsest solution (K -sparse). Several variants of OMP, e.g., CoSaMP [63], optimize this approach selecting multiple columns per iteration, pruning the set of active columns at each step or solving the least squares problems iteratively [31].

Modern pursuit methods are analogous to iterative thresholding algorithms such as IHT [62]. It is a simple algorithm to solve (2.14) given as

$$\mathbf{x}^{[n+1]} = H_K[\mathbf{x}^{[n]} + \Psi^T(\mathbf{y} - \Psi\mathbf{x}^{[n]})] \quad (2.15)$$

where a non-linear operator $H_K[\mathbf{z}]$ resets all elements of \mathbf{z} to zero except the largest K elements [62].

Having shown the problem to solve for the recovery of sparse signals, now we give the properties that the measurement matrix must bear.

2.3.2 Sensing matrix construction

In order to utilize the measurement matrix Ψ in CS framework, the condition called the RIP is needed to demonstrate the robustness of a matrix for CS. The matrix Ψ satisfies the RIP of order K if there exists a constant $\xi_K \in (0, 1)$ such that

$$(1 - \xi_K)\|\mathbf{x}\|_2^2 \leq \|\Psi\mathbf{x}\|_2^2 \leq (1 + \xi_K)\|\mathbf{x}\|_2^2 \quad (2.16)$$

holds for all $\mathbf{x} \in \Sigma_K$ where Σ_K is the set of all K -sparse vectors [29]. If ξ_K is close enough to zero then Ψ obeys the RIP of order K . When (2.16) holds, Ψ approximately preserves the Euclidean length of the K -sparse signals, which in turn implies that K -sparse vectors cannot be in the null space of Ψ [30]. This guarantees that there is a solution to (2.14).

There are random matrices satisfying the RIP if

$$M \geq CK \log(N/K) \quad (2.17)$$

holds where M is the number of compressive samples, N is the sparse vector dimension and C is some constant depending on each instance [30]. While these matrices are mostly formed by sampling i.i.d. entries from the normal, Bernoulli or another sub-Gaussian distribution [86], partial DFT matrices [26,87,88] promise fast matrix multiplications when their usage suit the problem. This is the case in our proposed approach which we present shortly.

The following theorem from [88] gives the RIP condition for partial DFT matrices.

Theorem 1 *Let $\mathbf{F} \in \mathbb{C}^{N \times N}$ be a DFT matrix with its entries defined as*

$$[\mathbf{F}]_{mn} = \frac{e^{-j2\pi mn}}{\sqrt{N}} \quad m, n \in [0, \dots, N-1] \quad (2.18)$$

and let $\xi_K > 0$ be a fixed constant. For some

$$M = \mathcal{O}(K \log^2 K \log N) \quad (2.19)$$

let $\mathbf{\Gamma} \in \mathbb{C}^{M \times N}$ be a matrix whose M rows are chosen uniformly and independently from the rows of \mathbf{F} , multiplied by $\sqrt{N/M}$. Then, with high probability, the matrix $\mathbf{\Gamma}$ satisfies the RIP of order K with constant ξ_K .

This is a significant improvement over $\mathcal{O}(K \log^6 N)$ and $\mathcal{O}(K \log N \log(K \log N) \log^2 K)$ proposed in [26] and [87], respectively. We make use of this theorem in developing the CS of CMS in the following section.

2.3.3 Proposed approach

For notational convenience which is needed in CS procedure, we give the CMS of $x[l]$ of (2.5) in matrix notation. Hence we need to stack the windowed signal $x_w[l] = x[l]w[l - nV]$ into a matrix as

$$\mathbf{X} = \begin{bmatrix} x_w[0] & x_w[1] & \dots & x_w[L-1] \\ x_w[V] & x_w[V+1] & \dots & x_w[V+L-1] \\ \vdots & \vdots & \ddots & \vdots \\ x_w[D-L] & x_w[D-L+1] & \dots & x_w[D-1] \end{bmatrix}.$$

Note that \mathbf{X} is an $N \times L$ matrix. The first step is to calculate the spectrogram by multiplying \mathbf{X} from the right with a DFT matrix and element-wise squaring the absolute values. Then, the CMS matrix is obtained by a second DFT matrix multiplication from the left as

$$\mathbf{P}_x = \mathbf{F}_N |\mathbf{X} \mathbf{F}_L^H|^{\circ 2} \quad (2.20)$$

where $(\cdot)^H$ denotes the Hermitian transpose, $(\cdot)^{\circ 2}$ is the Hadamard (element-wise) square of a matrix. \mathbf{F}_N and \mathbf{F}_L are $N \times N$ and $L \times L$ DFT matrices defined in (2.18), respectively.

Now let us form a CS scheme by uniformly choosing M random rows of \mathbf{X} with an $M \times N$ permutation matrix \mathbf{O} multiplied by $\sqrt[4]{N/M}$, so we can form an $M \times L$ matrix as

$$\mathbf{Y} = \sqrt[4]{N/M} \mathbf{O} \mathbf{X} \quad (2.21)$$

where each row of \mathbf{O} contains a single one and zeros elsewhere. Now we can write the compressive CMS matrix as

$$\mathbf{P}_y = \mathbf{F}_M |\mathbf{Y} \mathbf{F}_L^H|^{\circ 2} \quad (2.22)$$

where \mathbf{F}_M is the $M \times M$ DFT matrix. Inserting (2.21) into (2.22) and using (2.20) we obtain

$$\begin{aligned} \mathbf{P}_y &= \mathbf{F}_M |\sqrt[4]{N/M} \mathbf{O} \mathbf{X} \mathbf{F}_L^H|^{\circ 2} \\ &= \sqrt{N/M} \mathbf{F}_M \mathbf{O} |\mathbf{X} \mathbf{F}_L^H|^{\circ 2} \\ &= \sqrt{N/M} \mathbf{F}_M \mathbf{O} \mathbf{F}_N^H \mathbf{P}_x. \end{aligned} \quad (2.23)$$

Since the matrix \mathbf{O} consists of ones and zeros, it can be taken outside the absolute value operator where $\mathbf{O}^{\circ 2} = \mathbf{O}$. Moreover, \mathbf{F}_N is a unitary matrix, so that we can use $|\mathbf{X} \mathbf{F}_L^H|^{\circ 2} = \mathbf{F}_N^H \mathbf{P}_x$.

Note that $\sqrt{N/M} \mathbf{O} \mathbf{F}_N^H$ is now the CS matrix $\mathbf{\Gamma}$ given in Theorem 1 which satisfies the RIP. Since the ℓ_2 norm is preserved under orthonormal transforms $\mathbf{F}_M \mathbf{\Gamma}$ also satisfies the RIP. As a consequence, we have a linear relationship between the Nyquist-rate and compressive CMS matrices as

$$\mathbf{P}_y = \mathbf{\Psi} \mathbf{P}_x \quad (2.24)$$

where $\mathbf{\Psi} = \sqrt{N/M} \mathbf{F}_M \mathbf{O} \mathbf{F}_N^H$ is the measurement matrix satisfying the RIP of order K for the condition given in (2.19).

The model given in (2.24) is also known as the Multiple Measurement Vector (MMV) problem in sparse recovery literature [89]. In MMV scheme, one can split the problem into Single Measurement Vector (SMV) problems as in (2.14) and solve for each instance one by one. In our case, we can think of each column of \mathbf{P}_x is mapped to corresponding column of \mathbf{P}_y by the measurement matrix $\mathbf{\Psi}$, thus the problem can be treated separately for each spectral band.

However, when the columns of \mathbf{P}_x are jointly sparse as in our problem, i.e., the columns are spanning the propeller tonals having the same cyclic frequencies at all spectral bands (see Figs. 2.3 and 2.4), then it is computationally more efficient to solve the problem jointly for all the spectral bands. Besides, one might get a sparser picture if this information can be used in favor of maximizing the sparsity. To do that, we need to impose the sparsity of a vector which maximizes the joint sparse nature of the problem. In MMV problem, this vector is mostly derived from the row- ℓ_2 -norms of the matrix to be recovered [90]. The intuition behind is that one might get a vector depicting larger energy (or ℓ_2 -norm) for the indices exhibiting the joint sparsity. However, it might not be ideal for our problem where we seek the sparsity rather to detect the periodicity than to represent the cyclic energy. Fig. 2.6 shows this explicitly where row- ℓ_2 -norms of the CMS matrix, i.e., $\sqrt{\text{diag}(\mathbf{P}_x \mathbf{P}_x^H)}$, yield a result which not only lacks sparsity but also the information on the propeller tonals we pursue. This is probably due to the nonstationary nature of the real-world ambient noise mentioned in the previous section.

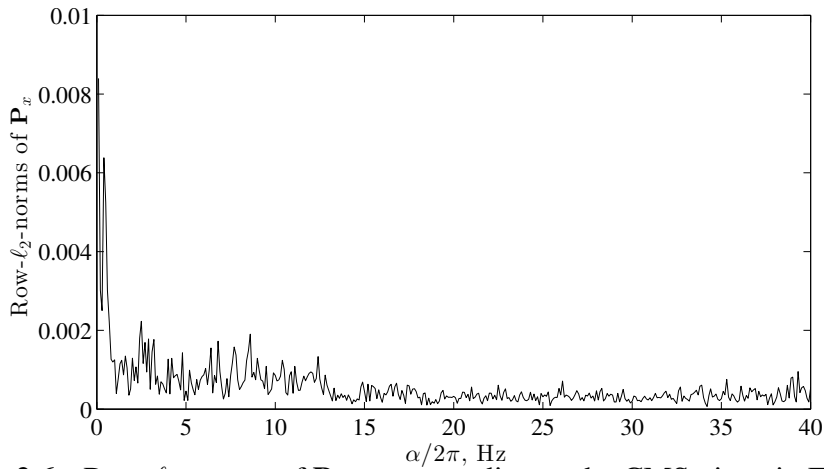


Figure 2.6 : Row- ℓ_2 -norms of \mathbf{P}_x corresponding to the CMS given in Fig. 2.4.

ICMC of Fig. 2.5, on the other hand, not only addresses the sparsest picture but also reveals the cyclostationarity to detect. For that reason we propose to employ the vector formed by the ICMC estimates as $\hat{\mathbf{g}}_x = [\hat{g}_x(0), \hat{g}_x(\Delta\alpha), \dots, \hat{g}_x((N-1)\Delta\alpha)]^T$ where $\hat{g}_x(n\Delta\alpha)$, $n = 0, 1, \dots, N-1$, is the n th element of this vector defined in (2.8). Now we can rewrite the sparse approximation problem given in (2.14) as

$$\min_{\hat{\mathbf{P}}_x} \|\mathbf{P}_y - \Psi \hat{\mathbf{P}}_x\|_F \quad \text{subject to} \quad \|\hat{\mathbf{g}}_x\|_0 \leq K \quad (2.25)$$

where $\|\cdot\|_F$ is the Frobenius norm operator. Namely the problem is to minimize the Frobenius norm of the error in approximating the CMS matrix while keeping the ICMC vector at least K -sparse. Note that, we cannot express a linear relationship between the Nyquist-rate CMC and compressive CMC due to the nonlinear normalization process of (2.7). Thus, we first recover the CMS and then calculate the CMC and ICMC using the CMS.

We utilize two popular greedy pursuit algorithms to solve (2.25): CoSaMP of [63] and IHT of [62]. The algorithms we propose are given in Algorithm 1 and 2, as Block CoSaMP (BCoSaMP) and Block IHT (BIHT), respectively. Since both algorithms are originally proposed for the recovery of sparse vectors we only modify them to suit to matrix (CMS) recovery. Interested readers are referred to above papers for detailed definitions and theoretical guarantees of these algorithms. The parameters used in both algorithms are defined in Table 2.1.

Algorithm 1: BCoSaMP for CMS recovery

Input: $\mathbf{P}_y, \Psi, K, \varepsilon, I$
Output: $\hat{\mathbf{P}}_x$

- 1 $\hat{\mathbf{P}}_x^{[0]} = \mathbf{0}, \mathbf{Z} = \mathbf{P}_y, \eta = \emptyset$
- 2 **for** $i = 0, \dots, I - 1$ **do**
- 3 $\tilde{\mathbf{P}}_x = \Psi^H \mathbf{Z}$
- 4 $\rho = \eta \cup \text{supp}(\tilde{\mathbf{g}}_x)_{2K}$
- 5 $\dot{\mathbf{P}}_x = \Psi_\rho^\dagger \mathbf{P}_y$
- 6 $\eta = \text{supp}(\dot{\mathbf{g}}_x)_K$
- 7 $\hat{\mathbf{P}}_x^{[i+1]} = [\dot{\mathbf{P}}_x]_\eta$
- 8 $\mathbf{Z} = \mathbf{P}_y - \Psi \hat{\mathbf{P}}_x^{[i+1]}$
- 9 **if** $\|\mathbf{Z}\|_F / \|\mathbf{P}_y\|_F \leq \varepsilon$ **or** $i \geq I$ **then**
- 10 **break**
- 11 **end**
- 12 **end**

2.4 Numerical Examples

In this section we present simulation results of Algorithm 1 and Algorithm 2 on recovery and detection of propeller tonals. We have synthesized propeller noise

Algorithm 2: BIHT for CMS recovery

Input: $\mathbf{P}_y, \Psi, K, \varepsilon, I$
Output: $\hat{\mathbf{P}}_x$

```
1  $\hat{\mathbf{P}}_x^{[0]} = \mathbf{0}, \mathbf{Z} = \mathbf{P}_y$ 
2 for  $i = 0, \dots, I - 1$  do
3    $\tilde{\mathbf{P}}_x = \hat{\mathbf{P}}_x^{[i]} + \Psi^H \mathbf{Z}$ 
4    $\eta = \text{supp}(\tilde{\mathbf{g}}_x)_K$ 
5    $\hat{\mathbf{P}}_x^{[i+1]} = [\tilde{\mathbf{P}}_x]_\eta$ 
6    $\mathbf{Z} = \mathbf{P}_y - \Psi \hat{\mathbf{P}}_x^{[i+1]}$ 
7   if  $\|\mathbf{Z}\|_F / \|\mathbf{P}_y\|_F \leq \varepsilon$  or  $i \geq I$  then
8     break
9   end
10 end
```

Table 2.1 : Parameters used in the Algorithms 1 and 2

$\Psi \in \mathbb{C}^{M \times N}$	Measurement matrix
$\Psi_\rho \in \mathbb{C}^{M \times 3K}$	Subset of measurement matrix
$\mathbf{P}_y \in \mathbb{C}^{M \times L}$	Measured CMS
$\hat{\mathbf{P}}_x^{[i]} \in \mathbb{C}^{N \times L}$	Recovered CMS at i th iteration
$\hat{\mathbf{P}}_x \in \mathbb{C}^{N \times L}$	Recovered CMS with minimum residual norm
$\tilde{\mathbf{P}}_x \in \mathbb{C}^{N \times L}$	CMS projection estimate
$\hat{\mathbf{P}}_x \in \mathbb{C}^{N \times L}$	CMS least-squares estimate
$\tilde{\mathbf{g}}_x \in \mathbb{C}^N$	ICMC projection estimate
$\hat{\mathbf{g}}_x \in \mathbb{C}^N$	ICMC least-squares estimate
$\mathbf{Z} \in \mathbb{C}^{M \times L}$	Residual
$\text{supp}(\cdot)_K$	Support with K largest values
$[\cdot]_\eta$	Selects the rows with the set of indices η
K	Approximation sparsity
ε	Error tolerance
I	Maximum number of iterations
\dagger	Pseudo inverse symbol

according to (2.1) with different parameters to represent different sparsity levels: a weakly modulated propeller noise ($\mu = 0.25$), a moderately modulated propeller noise ($\mu = 0.5$) and a strongly modulated propeller noise ($\mu = 0.75$). We have set the SNR (broadband propeller to ambient noise ratio) to 0 dB and 10 dB for each modulation index. Generated noise is two-second-long with the sampling frequency $f_s = 16384$

Hz. There are ten harmonics with uniformly random amplitudes between 0.1 and 1 ($a_k \sim \text{U}[0.1, 1]$) in each modulating signal with BR = 5 Hz. Broadband propeller and ambient noise are generated as pink noise to simulate the realistic (colored) scenario. We employ Hann window with length and shifting size of $L = 64$ and $V = 16$ (75% overlap), respectively. We have used $p = 0.001$ level of significance and the whole spectral band for the detection with ICMC. Approximation sparsity K is chosen in accordance with the condition given in (2.19) for every other number of compressive samples, M .

We measure the ICMC recovery performance with the Normalized MSE (NMSE) defined as

$$\text{NMSE} = \frac{\|\hat{\mathbf{g}}_x - \mathbf{g}_x\|_2^2}{\|\mathbf{g}_x\|_2^2}, \quad (2.26)$$

and ICMC detection performance with the probability of detection (P_d) and the total Detection SNR (DSNR) defined as

$$\text{DSNR} = \sum_{\alpha_i \in \Lambda} \frac{g_x(\alpha_i)}{\lambda_{1-p}(\alpha_i)}. \quad (2.27)$$

where Λ is the set including all the (ground truth) cyclic frequencies, α_i , indicating the presence of cyclostationarity, i.e., propeller tonals.

Figs. 2.7 and 2.8 display the simulation results averaged over thousand trials. First rows of the figures show the NMSE, DSNR and P_d curves of weakly modulated propeller noise. Higher NMSE values indicate the poor recovery performance which is expected due to lower sparsity level.

Recall that, SCF magnitude at BR component relies on the modulation index and SNR, i.e., the sparsity of the CMS as the SCF approximation declines with weaker modulation and lower SNR which also decreases the sparsity of the ICMC vector. Thus, the magnitudes of the propeller tonals are close to the ones corresponding to the cyclic frequency indices which do not exhibit cyclostationarity. As mentioned before, this is due to finite dimensions of the signal as well as the lack of ability to synthesize exactly stationary noise. In sparse recovery literature, this effect is investigated under

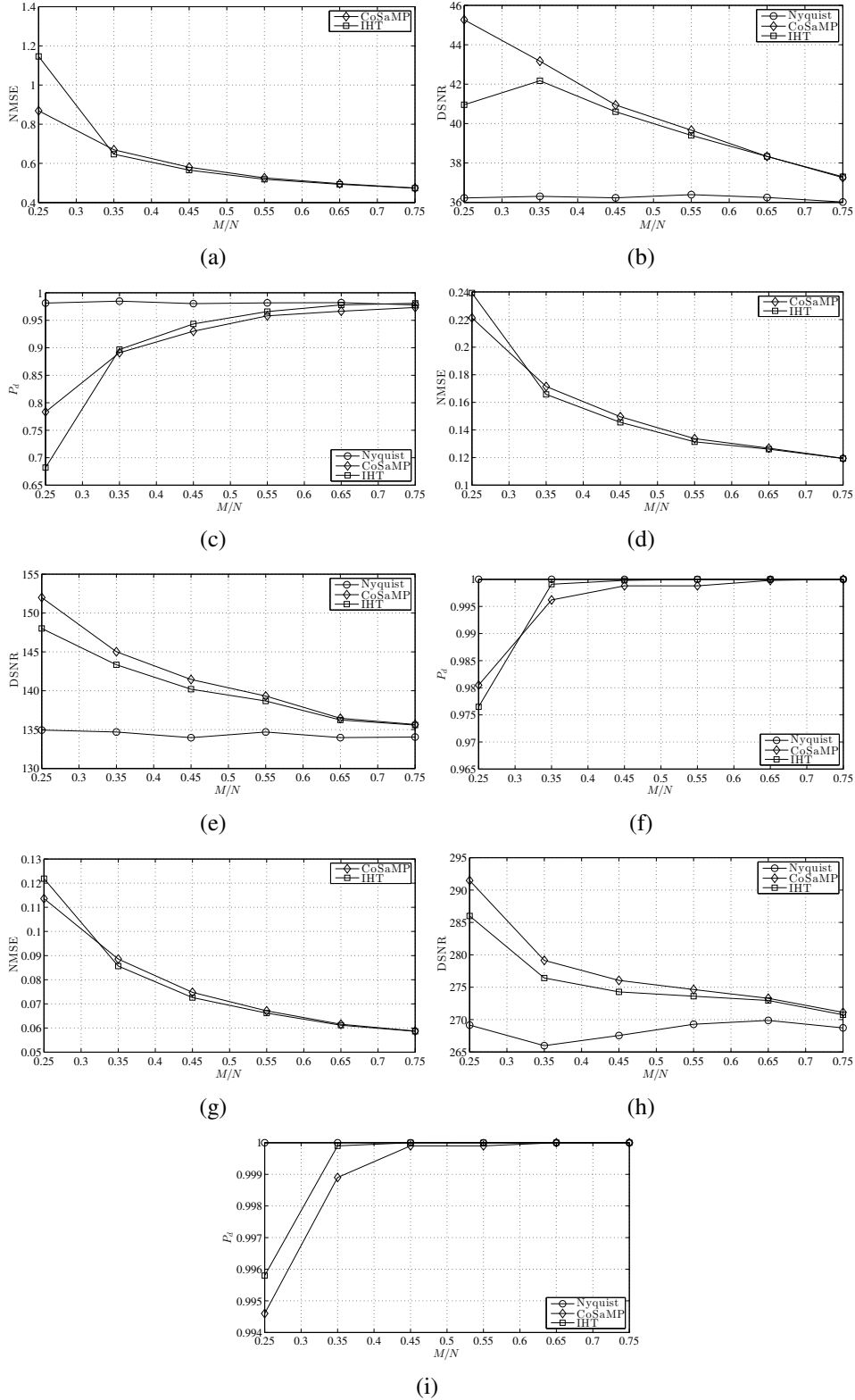


Figure 2.7 : NMSE, DSNR and P_d plots averaged over 1000 trials for SNR = 0 dB of a-b-c) weakly modulated propeller noise ($\mu = 0.25$), d-e-f) moderately modulated propeller noise ($\mu = 0.5$), g-h-i) strongly modulated propeller noise ($\mu = 0.75$), respectively. NMSE, DSNR and P_d curves indicated by 'CoSaMP' and 'IHT' give the results obtained by the ICMCs recovered with Algorithm 1 and 2, respectively. DSNR and P_d curves indicated by 'Nyquist' give the results obtained by the Nyquist-rate ICMC.

the noisy sparse recovery [29], i.e, there exists an additive noise in the measurement procedure. This noise, in our problem, is formed by the nonstationary components which superpose on the propeller tonals in the ICMC vector.

In contrast to sufficient recovery, DSNR and P_d indicate that detection is still possible at the performance slightly lower ($P_d > 0.95$ for SNR = 0 dB, $P_d > 0.995$ for SNR = 10 dB) than the Nyquist-rate processing ($P_d > 0.98$ for SNR = 0 dB, $P_d = 1$ for SNR = 10 dB) unless the compression rate (M/N) is under 0.55. The evolution of DSNR curves obtained from detections with recovered samples might be misleading due to higher DSNR values for lower compression rates. The reason behind is that lower M/N causes noisier projection estimate, i.e., $\tilde{\mathbf{P}}_x = \mathbf{\Psi}^H \mathbf{Z}$. This results in overestimation of some cyclic components which turns out to add up to a higher DSNR (compared to Nyquist-rate DSNR) even with the miss of some other components. This can also be verified by P_d curves where one can see lower P_d compared to the Nyquist-rate P_d for lower compression rates. This is also the case for moderately and strongly modulated noise.

Second and third rows of Figs. 2.7 and 2.8 demonstrate the positive effect of increasing the modulation index to both recovery and detection performance. NMSE values decreased dramatically together with the rate of difference between the Nyquist-rate and recovered DSNR values. Recovered ICMCs have almost the same P_d values as the Nyquist-rate ICMC has for $M/N \leq 0.35$ while yielding the same P_d for compression rates $M/N \geq 0.65$ (SNR = 0 dB) and $M/N \geq 0.45$ (SNR = 10 dB). Note that, ICMCs of strongly modulated noise are recovered much better than the ones of moderately modulated noise since the sparsity is higher.

As for the comparison of CoSaMP and IHT, the latter has slightly better recovery performance than the former for $M/N > 0.3$. This might be due to stricter conditions that CoSaMP requires on ξ_K in order for RIP to hold and lower approximation error that IHT guarantees [62]. However all the NMSE curves reveal that both algorithms tend to converge almost to the same performance as the compression rate increases. We have a somewhat similar picture in terms of detection. IHT performs slightly better in approximating the DSNR that the Nyquist-rate ICMC yields with P_d curves confirming

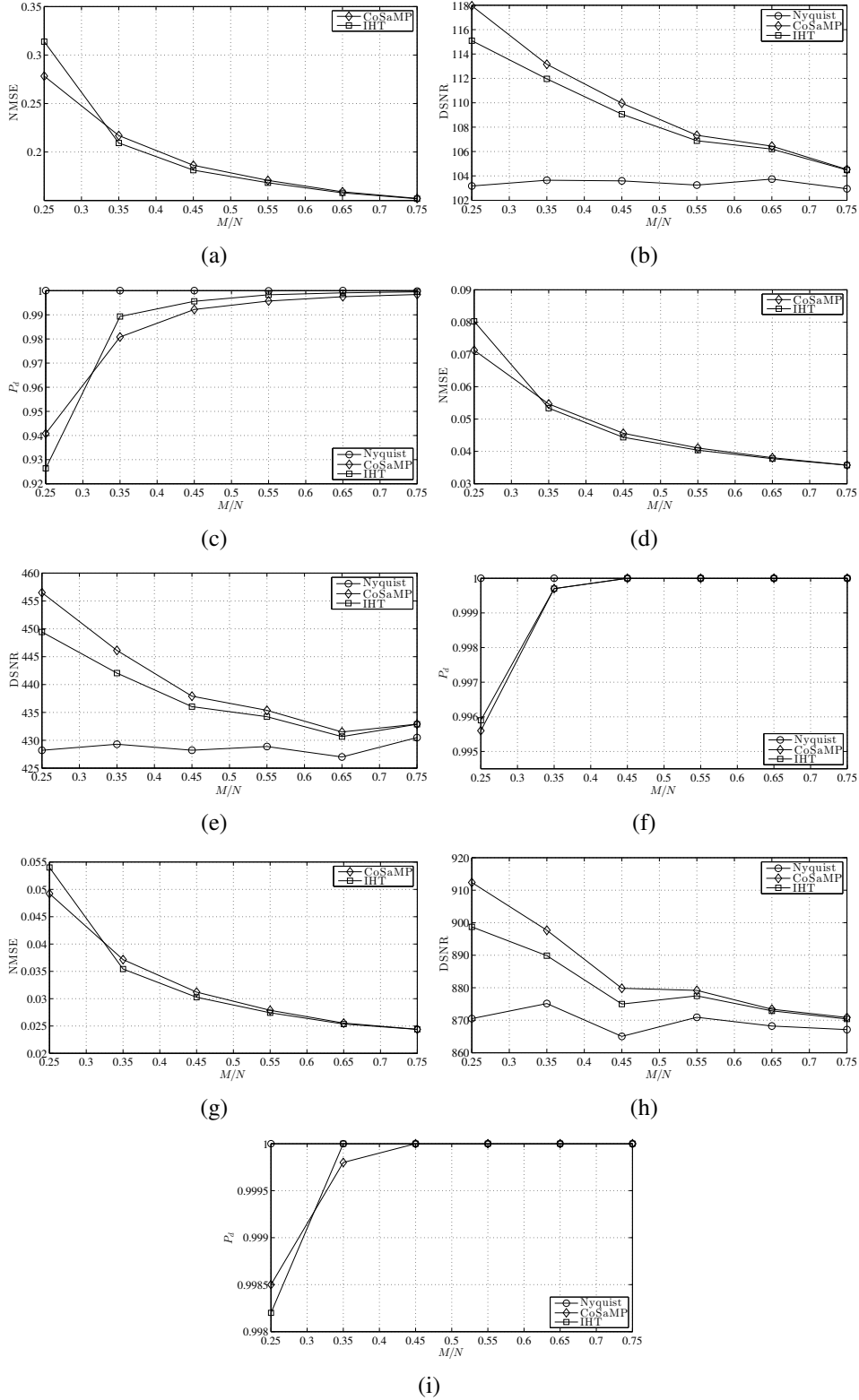


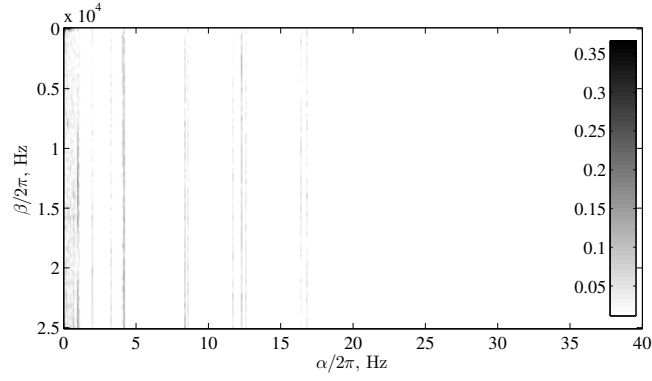
Figure 2.8 : NMSE, DSNR and P_d plots averaged over 1000 trials for SNR = 10 dB of a-b-c) weakly modulated propeller noise ($\mu = 0.25$), d-e-f) moderately modulated propeller noise ($\mu = 0.5$), g-h-i) strongly modulated propeller noise ($\mu = 0.75$), respectively. NMSE, DSNR and P_d curves indicated by 'CoSaMP' and 'IHT' give the results obtained by the ICMCs recovered with Algorithm 1 and 2, respectively. DSNR and P_d curves indicated by 'Nyquist' give the results obtained by the Nyquist-rate ICMC.

this result. Interested readers are referred to [63] and [62] for the bounds on the noisy sparse approximation error as well as other theoretical recovery guarantees for CoSaMP and IHT for SMV case, respectively, while [90] investigates the performance bounds of both methods for an MMV setting.

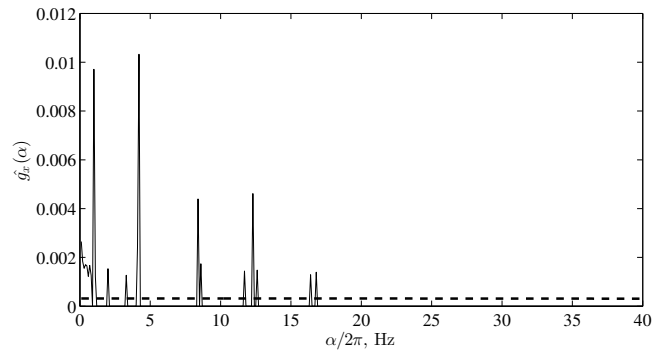
Finally, we give a real-world example regarding an actual ambient noise which contains the radiated noise of a ship of opportunity recorded with BANAS in the Strait of Istanbul [85]. The data consists of a ten-second-long record from a broadband hydrophone at the depth of 20 meters with the sampling frequency $f_s = 50000$ Hz. A small segment of the time signal can be seen in Fig. 2.4. Parameters to calculate the CMS, CMC and ICMC are given in Section 2.2.

Note that, we do not possess all the information on the propeller tonals of this ship since this record is from an uncontrolled experiment. However, we observe some propeller tonals at the cyclic frequencies mentioned in Section 2.2. Thus, we assume merely those components are to recover and detect with our proposed algorithms. Comparing Fig. 2.5 with Fig. 2.9, one can observe that all those propeller tonals which are detected by the Nyquist-rate CMC/ICMC are also detected by the CMC/ICMC recovered with CoSaMP and IHT. DSNR values are higher (117.74 for ICMC recovered by CoSaMP and 118.63 for ICMC recovered by IHT versus 112 for Nyquist-rate ICMC) possibly due to overestimation of ICMC components. This is of little importance since the main aim is to detect the propeller tonals which is succeeded. Note also that, the spectral dimensions of the recovered and Nyquist-rate CMCs agree very well at the cyclic frequencies of the propeller tonals. This is by virtue of the MMV approach which allows to impose a better (joint) sparsity constraint while enabling our proposed algorithms to select the whole spectral band when reconstructing the CMS estimates.

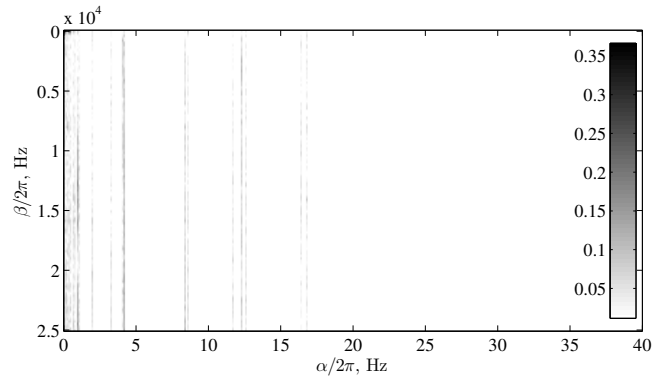
On the other hand, algorithms yield relatively higher NMSEs which suggest a poor recovery performance. However, this result is due to the nonstationarity of the real-world noise causing a dense ICMC vector. That is to say, it acts like the observation noise in noisy sparse approximation problem mentioned above. As a consequence, this unrecoverable energy yields larger NMSE.



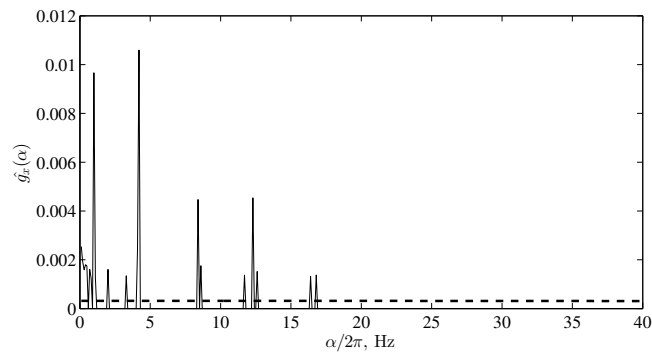
(a)



(b)



(c)



(d)

Figure 2.9 : CMC and ICMC recovered with a,b) Algorithm 1 (BCoSaMP), NMSE = 0.4734, DSNR = 117.74, c,d) Algorithm 2 (BIHT), NMSE = 0.4750, DSNR = 118.63, respectively. Compression rate is $M/N = 0.5$. For Nyquist-rate CMC and ICMC, see Fig. 2.5. Dotted line indicates the statistical threshold with %0.1 level of significance.

In Fig. 2.9, we observe some additional detections in both ICMC recoveries of CoSaMP and IHT at the cyclic frequencies of 2 Hz, 3.2 Hz and 7.7 Hz which are not anticipated to be recovered. The component at 2 Hz might be the first harmonic of the PSR while the other two might indicate either the propeller tonals shifted in frequency by an unprecedented effect or the cyclostationarity caused by another source at the recording site. Nevertheless they are in accordance with the detections of the Nyquist-rate ICMC.

Note also that, there are detections spanning under 1 Hz, explicitly seen in Fig. 2.9, which also agrees with the picture of Fig. 2.5. Recall that, the recording site is a highly reverberant environment with a heavy ship traffic which might contribute to this nonstationarity.

As a final remark of marginal importance, CoSaMP performs slightly better (it yields lower NMSE than IHT does and DSNR obtained is closer to Nyquist-rate DSNR) than IHT which contradicts with the above simulation results of synthesized data. However, the outputs of this real-world example are based on a single experiment while the simulation results are generated from the mean values of 1000 realizations. Thus, this specific situation should not be generalized as a performance statistic.

2.5 Discussion

In Section 2.1, we stated that the amplitude modulated propeller noise yields a sparse SCF which enables the CS to mitigate the negative effects of an inefficient Nyquist-rate sampling scheme. While this is not completely groundless, as the results from the previous section suggest, perfect sparse approximation of the Nyquist-rate CMS seems not possible because it lacks the sufficient sparsity. On the other hand, detection with the recovered samples is still possible depending on the sparsity level and compression rate.

In the light of the obtained results, a possible future direction would be to seek the ways to maximize the sparsity by adjusting the parameters to calculate the CMC. Another one would be the determination of the optimum approximation sparsity that minimizes the reconstruction error on which an upper bound should be derived.

Investigating the results on real-world data obtained by controlled experiments, i.e., the availability of ground truth information on the propeller tonals would help to clarify the precision of our proposed scheme. In addition, open and deep water performance of this detector would be probably better since this environment suggest less nonstationarity due to the lighter ship traffic and less reverberation. Thus, real-world experiments should also include the data acquisition in this type of setting.

As a final remark, the scheme we propose can be applied not only to propeller tonals recovery and detection but also to many areas involving CS of second-order cyclostationary statistics such as spectrum sensing [65], TF analysis [68,69] and machine diagnostics [18].

3. HIGHER-ORDER CYCLIC SPECTRA AND COMPRESSIVE SENSING

3.1 Introduction

Ship-radiated noise caused by the propeller cavitation exhibits cyclostationary characteristics as investigated in Chapter 2, [19,52,91]. DEMON [8,12,13,55,59,60,73,74] is traditionally utilized for acquiring the propeller tonals which are the frequency components representing the propeller revolution rate. Other approaches to get these tonals are based on maximum likelihood estimation [13,59,82] and empirical mode decomposition [58]. There are studies that focus on the compelling problems of the effects of the ship roll and pitch [56], impulsive noise [60] and multi path propagation [55]. Most of the above works are based on SOS, where it is assumed that ship-radiated and ambient noise are Gaussian and/or stationary random processes [8,19,59,82]. However, many real world measurements show that underwater noise could be nonstationary [21,22,83,84,92]–[95] and non-Gaussian [21,22,83,84,92]–[102].

In [21], non-Gaussianity and nonlinearity of ship-radiated and ambient noise are estimated from real-world data. It is reported that the ship-radiated noise yields nonzero bispectrum while the ambient noise does not contain any significant bispectral components. Nonzero bispectrum is due to the cavitation bubbles forming in a nonlinear fashion. In [22], ambient noise in a “quiet region” showed the closest characteristic to the usual stationary Gaussian assumption. Main contributors to this type of ambient noise are the wind and distant shipping noise. Thus, in the absence of close noise sources the Central Limit Theorem (CLT) drives any non-normality toward Gaussian. On the other hand, data from a “noisy region”, where heavy distant shipping traffic dominates, diminishes the convergence of the CLT, i.e., causing a departure from normality. This departure becomes even more significant for the merchant ship

This chapter is based on the paper “U. Firat and T. Akgül, Compressive Sensing of Cyclic Bispectrum, submitted to IEEE Journal of Oceanic Engineering in February 2023”.

noise, where the machinery and propeller cavitation noise dominate the ambient noise. Data from seismic explorations and biological activity contain impulsive noise bursts causing heavy-tailed distributions, which yield the largest deviations from normality.

These real-world examples show that stationarity and Gaussianity assumptions might cause a performance degradation in detecting ship-radiated noise. Therefore, robust signal processing methods based on HOS should be considered when deviations from normality occurs. In underwater acoustic signal processing, HOS based methods are only considered for transient, periodic or narrowband signals and broadband ship-radiated noise [21,93,101]–[103].

We propose CMBC for robust detection of the higher-order cyclostationary ship-radiated noise and extracting propeller tonals. It is based on a second-order method, CMC, suggested in [19]. We assume that the propeller noise is non-Gaussian while the ambient noise is Gaussian yielding zero bispectrum. This brings two advantages: i) cyclic part eliminates Gaussian or non-Gaussian stationary noise; ii) HOS part yields zero bispectrum for cyclostationary or stationary Gaussian components.

Furthermore, we derive the cyclic third-order cumulant spectrum of a cyclostationary signal model, i.e., amplitude modulated broadband propeller noise, and show its sparsity in cyclic frequency domain. We then propose a HOS based CS scheme which enables the synchronous non-Gaussian signal sensing and compression for sparse signals [23,25] such as the propeller tonals. We utilize greedy pursuit methods [52,62,63,90] to recover these tonals and compare it with the ones obtained by Nyquist-rate samples.

3.2 Higher-Order Cyclostationary Statistics

Considering a single sinusoid representing the propeller tonal, we can model the propeller noise measurement as

$$x(t) = [1 + \mu \cos(\alpha_0 t)]c(t) + v(t) \quad (3.1)$$

where $[1 + \mu \cos(\alpha_0 t)]c(t)$ is the propeller noise and $v(t)$ is the ambient noise [8,13,55]–[60]. The envelope $[1 + \mu \cos(\alpha_0 t)]$ modulates the amplitude of the

broadband propeller noise $c(t)$ with the modulation index μ . The frequency of the propeller tonal is α_0 rad/s.

3.2.1 Cyclic bispectrum

The cyclic third-order cumulant spectrum, i.e., CBS, can be derived using the instantaneous third-order cumulant [64]. Assuming $c(t)$ and $v(t)$ as uncorrelated zero-mean wide-sense stationary random processes we obtain it as

$$\begin{aligned}
C_{3x}(t, s, r) &\triangleq \mathbb{E}\{x(t)x(s)x(r)\} \\
&= [1 + \mu \cos(\alpha_0 t) + \mu \cos(\alpha_0(t + \tau_1)) + \mu \cos(\alpha_0(t + \tau_2)) \\
&\quad + \mu^2 \cos(\alpha_0 t) \cos(\alpha_0(t + \tau_1)) + \mu^2 \cos(\alpha_0 t) \cos(\alpha_0(t + \tau_2)) \\
&\quad + \mu^2 \cos(\alpha_0(t + \tau_1)) \cos(\alpha_0(t + \tau_2)) \\
&\quad + \mu^3 \cos(\alpha_0 t) \cos(\alpha_0(t + \tau_1)) \cos(\alpha_0(t + \tau_2))] C_{3c}(\tau_1, \tau_2) \\
&\quad + C_{3v}(\tau_1, \tau_2) = C_{3x}(t, \tau_1, \tau_2)
\end{aligned} \tag{3.2}$$

where $\mathbb{E}\{\cdot\}$ is the expected value operator, $\tau_1 = s - t$, $\tau_2 = r - t$ with third order cumulants $C_{3c}(\tau_1, \tau_2) = \mathbb{E}\{c(t)c(s)c(r)\}$ and $C_{3v}(\tau_1, \tau_2) = \mathbb{E}\{v(t)v(s)v(r)\}$. Note that $C_{3x}(t, \tau_1, \tau_2) = C_{3x}(t + nT, \tau_1, \tau_2)$, thus $x(t)$ is cyclostationary with the period $T = 2\pi/\alpha_0$ and $n \in \mathbb{Z}$. Then, the CBS $B_{3x}(\alpha, \omega_1, \omega_2)$ can be found by applying FS expansion over t and FT over τ_1 and τ_2 to $C_{3x}(t, \tau_1, \tau_2)$. Fig. 3.1 shows relations of random processes in their third-order statistics, where $C_{3x}(t, \tau_1, \tau_2)$ has FS relation with the third-order cyclic cumulant $C_{3x}(\alpha, \tau_1, \tau_2)$ and FT relation with the third-order time-varying bispectrum $B_{3x}(t, \omega_1, \omega_2)$. Here, α and $\omega_{1,2}$ are the cyclic and spectral frequency variables, respectively. The CBS $B_{3x}(\alpha, \omega_1, \omega_2)$ has FS relation with $B_{3x}(t, \omega_1, \omega_2)$ and FT relation with $C_{3x}(\alpha, \tau_1, \tau_2)$. Clearly, $C_{3x}(\alpha, \tau_1, \tau_2)$ boils down to the third-order cumulant and $B_{3x}(\alpha, \omega_1, \omega_2)$ to the classical bispectrum, when there is no cyclostationarity ($\alpha = 0$).

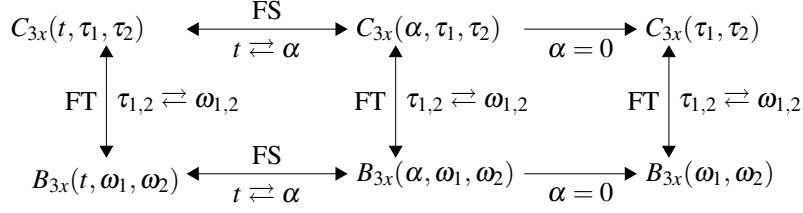


Figure 3.1 : Relations between third-order statistics.

Using these relations we can write the CBS of $x(t)$ as

$$\begin{aligned}
& B_{3x}(\alpha, \omega_1, \omega_2) \\
&= \left\{ B_{3c}(\omega_1, \omega_2) + B_{3v}(\omega_1, \omega_2) + \frac{\mu^2}{4} \left[B_{3c}(\omega_1 - \alpha_0, \omega_2 + \alpha_0) + B_{3c}(\omega_1 + \alpha_0, \omega_2 - \alpha_0) \right. \right. \\
&+ \left. \left. B_{3c}(\omega_1, \omega_2 + \alpha_0) + B_{3c}(\omega_1 + \alpha_0, \omega_2) + B_{3c}(\omega_1, \omega_2 - \alpha_0) + B_{3c}(\omega_1 - \alpha_0, \omega_2) \right] \right\} \delta(\alpha) \\
&+ \left\{ \frac{\mu}{2} \left[B_{3c}(\omega_1, \omega_2 - \alpha_0) + B_{3c}(\omega_1 - \alpha_0, \omega_2) + B_{3c}(\omega_1, \omega_2) \right] + \frac{\mu^3}{8} \left[B_{3c}(\omega_1 - \alpha_0, \omega_2 + \alpha_0) \right. \right. \\
&+ \left. \left. B_{3c}(\omega_1 + \alpha_0, \omega_2 - \alpha_0) + B_{3c}(\omega_1 - \alpha_0, \omega_2 - \alpha_0) \right] \right\} \delta(\alpha - \alpha_0) \\
&+ \left\{ \frac{\mu}{2} \left[B_{3c}(\omega_1, \omega_2 + \alpha_0) + B_{3c}(\omega_1 + \alpha_0, \omega_2) + B_{3c}(\omega_1, \omega_2) \right] \right. \\
&+ \left. \frac{\mu^3}{8} \left[B_{3c}(\omega_1 + \alpha_0, \omega_2 - \alpha_0) + B_{3c}(\omega_1 - \alpha_0, \omega_2 + \alpha_0) + B_{3c}(\omega_1 + \alpha_0, \omega_2 + \alpha_0) \right] \right\} \delta(\alpha + \alpha_0) \\
&+ \frac{\mu^2}{4} \left\{ B_{3c}(\omega_1 - \alpha_0, \omega_2 - \alpha_0) + B_{3c}(\omega_1, \omega_2 - \alpha_0) + B_{3c}(\omega_1 - \alpha_0, \omega_2) \right\} \delta(\alpha - 2\alpha_0) \\
&+ \frac{\mu^2}{4} \left\{ B_{3c}(\omega_1 + \alpha_0, \omega_2 + \alpha_0) + B_{3c}(\omega_1, \omega_2 + \alpha_0) + B_{3c}(\omega_1 + \alpha_0, \omega_2) \right\} \delta(\alpha + 2\alpha_0) \\
&+ \frac{\mu^3}{8} B_{3c}(\omega_1 - \alpha_0, \omega_2 - \alpha_0) \delta(\alpha - 3\alpha_0) + \frac{\mu^3}{8} B_{3c}(\omega_1 + \alpha_0, \omega_2 + \alpha_0) \delta(\alpha + 3\alpha_0) \quad (3.3)
\end{aligned}$$

where $B_{3c}(\omega_1, \omega_2)$ and $B_{3v}(\omega_1, \omega_2)$ are the FTs of $C_{3c}(\tau_1, \tau_2)$ and $C_{3v}(\tau_1, \tau_2)$, respectively. One-sided spectral support of (3.3) is shown in Fig. 3.2, where one can observe the sparsity of the propeller noise appearing in the cyclic frequency α due to the modulating signal. Note that, broadband propeller noise causes a dense support in the spectral frequencies $\omega_{1,2}$.

3.2.2 Cyclic modulation bispectrum

Estimating the CBS can be a cumbersome task since the real-world measurements are of finite length. Thus, we propose the CMBS based on the CMS [19]. CMBS offers a fast and reliable approximation of the CBS relying only on DFT.

Let $x[l] \triangleq x(lT_s), l = 0, \dots, D - 1$, be the D -long signal, which is the discretized counterpart of $x(t)$ given in (3.1) with the sampling frequency $f_s = 1/T_s$. An L -long analysis window $w[l]$ is used to take overlapped snapshots from the signal yielding

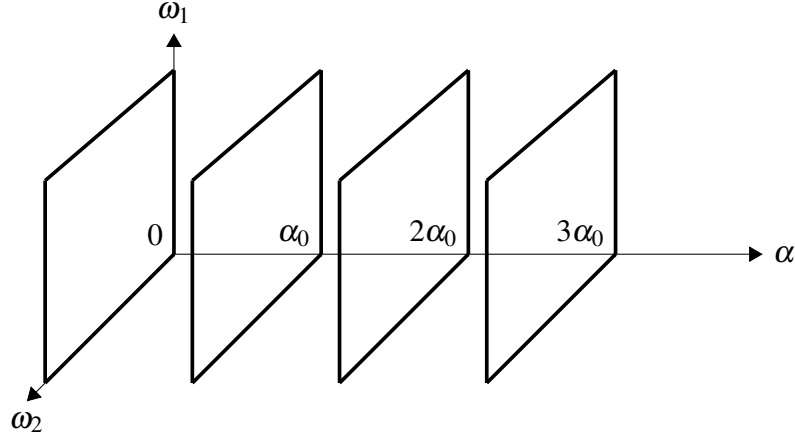


Figure 3.2 : Spectral support of the cyclic bispectrum of the propeller noise model given in (3.1).

$N = \lfloor \frac{D-L}{V} \rfloor + 1$ snapshots, where V is the shifting size. Then, the short-time DFT of the windowed signal can be calculated as

$$X_{\Delta\omega}(t_n, \omega) = T_s \sum_{l=nV}^{nV+L-1} x[l]w[l-nV]e^{-j\omega l T_s} \quad (3.4)$$

which returns the filtered signal in a narrow band with center frequency ω and width $\Delta\omega \sim 2\pi/LT_s$ at times $t_n = nVT_s$, $n = 0, \dots, N-1$ [19].

The direct bispectrum estimator [104] of the signal $x[l]$ is given as

$$\hat{B}_{3x}(\omega_1, \omega_2) = X(\omega_1)X(\omega_2)X^*(\omega_1 + \omega_2) \quad (3.5)$$

where $X(\omega)$ is the FT of $x[l]$. The CBS estimator [105] using this direct estimator can be calculated as

$$\hat{B}_{3x}(\alpha, \omega_1, \omega_2) = X(\omega_1)X(\omega_2)X^*(\omega_1 + \omega_2 - \alpha). \quad (3.6)$$

However, in terms of propeller tonals, the typical cyclic frequency $\alpha \ll \Delta\omega$ which is the spectral resolution of $X(\omega)$. This makes the utilization of the direct estimator impractical. Therefore, we propose to calculate the time-varying bispectrum using the short-time DFT in (3.4) as

$$\hat{B}_{3x}(t_n, \omega_1, \omega_2) = X_{\Delta\omega}(t_n, \omega_1)X_{\Delta\omega}(t_n, \omega_2)X_{\Delta\omega}^*(t_n, \omega_1 + \omega_2). \quad (3.7)$$

Similar to CMS, we can then formulate the CMBS as

$$P_{3x}(\alpha, \omega_1, \omega_2) = \frac{1}{N} \sum_{n=0}^{N-1} |\hat{B}_{3x}(t_n, \omega_1, \omega_2)| e^{-j\alpha t_n}. \quad (3.8)$$

Although CMBS represents the cyclostationarity, colored nature of the propeller noise causes lower spectral levels with increasing spectral frequency. We can define CMBC based on CMC [19] as

$$G_{3x}(\alpha, \omega_1, \omega_2) = \frac{P_{3x}(\alpha, \omega_1, \omega_2)}{P_{3x}(0, \omega_1, \omega_2)}. \quad (3.9)$$

which reveals the cyclic components independent of the spectral energy distribution the signal conveys. Notice that $P_{3x}(0, \omega_1, \omega_2)$ is the averaged bispectrum estimate of the signal. ICMBC enables rejecting the ambient noise by averaging over the spectral bands, where cyclostationarity is dominant. It can be defined as

$$g_{3x}(\alpha) = \frac{1}{\beta_1 \beta_2} \sum_{i=i_1}^{i_2} \sum_{k=k_1}^{k_2} |G_{3x}(\alpha, \omega_{1_i}, \omega_{2_k})|^2 \quad (3.10)$$

where i_1, i_2, k_1 and k_2 are the spectral frequency indices which define the bands with $\beta_1 = i_2 - i_1 + 1$ and $\beta_2 = k_2 - k_1 + 1$, respectively. ICMBC is also a useful quantity to enforce sparsity in a CS scheme as will be introduced in the next section.

3.3 Compressive Sensing of Cyclic Modulation Bispectrum

CS enables the acquisition and compression of the propeller tonals simultaneously since the CMBS exhibits sparsity in the cyclic frequency dimension. An incoherent basis is needed to transform the Nyquist-rate CMBS into the compressive one. Partial Fourier matrices are such bases, which satisfy the RIP needed to assess the fitness of a sensing matrix in CS [88].

Let us stack the windowed signal $x_w[l] = x[l]w[l - nR]$ into a matrix as

$$\mathbf{X} = \begin{bmatrix} x_w[0] & x_w[1] & \dots & x_w[L-1] \\ x_w[V] & x_w[V+1] & \dots & x_w[V+L-1] \\ \vdots & \vdots & \ddots & \vdots \\ x_w[D-L] & x_w[D-L+1] & \dots & x_w[D-1] \end{bmatrix}.$$

Note that \mathbf{X} is an $N \times L$ matrix. Now let us form a CS scheme by uniformly choosing M random rows of \mathbf{X} with an $M \times N$ permutation matrix \mathbf{O} multiplied by $\sqrt{N/M}$. We can form an $M \times L$ matrix as

$$\mathbf{Y} = \sqrt{N/M} \mathbf{O} \mathbf{X} \quad (3.11)$$

where each row of \mathbf{O} contains a single one and zeros elsewhere. Then we can form the time-varying bispectrum matrix $\mathbf{B}_{3x}^{\omega_2}$ where its entry in n th row and l th column is

$$[\mathbf{B}_{3x}^{\omega_2}]_{nl} = X_{\Delta\omega}(t_n, \omega_{1l})X_{\Delta\omega}(t_n, \omega_2)X_{\Delta\omega}^*(t_n, \omega_{1l} + \omega_2). \quad (3.12)$$

Here, ω_2 is fixed at each entry of the matrix and $\omega_{1l} = (l-1)\Delta\omega, l = 0, 1, \dots, L-1$. As a result, (3.11) implies that

$$\mathbf{B}_{3y}^{\omega_2} = \sqrt{N/M}\mathbf{O}\mathbf{B}_{3x}^{\omega_2} \quad (3.13)$$

where $\mathbf{B}_{3y}^{\omega_2}$ is the compressive time-varying bispectrum matrix. The FT of the magnitude of this matrix becomes

$$\mathbf{F}_M|\mathbf{B}_{3y}^{\omega_2}| = \mathbf{P}_{3y}^{\omega_2} = \sqrt{N/M}\mathbf{F}_M\mathbf{O}|\mathbf{B}_{3x}^{\omega_2}| \quad (3.14)$$

where \mathbf{F}_M is the $M \times M$ DFT matrix and $\mathbf{P}_{3y}^{\omega_2}$ is the compressive CMBS matrix. Similarly we can write the CMBS matrix of Nyquist samples as

$$\mathbf{P}_{3x}^{\omega_2} = \mathbf{F}_N|\mathbf{B}_{3x}^{\omega_2}| \quad (3.15)$$

where \mathbf{F}_N is the $N \times N$ DFT matrix. Since \mathbf{F}_N is a unitary matrix

$$|\mathbf{B}_{3x}^{\omega_2}| = \mathbf{F}_N^H \mathbf{P}_{3x}^{\omega_2} \quad (3.16)$$

where $(\cdot)^H$ is the Hermitian transpose operator. Combining (3.14) and (3.16) we get

$$\mathbf{P}_{3y}^{\omega_2} = \mathbf{\Psi}\mathbf{P}_{3x}^{\omega_2} \quad (3.17)$$

where $\mathbf{\Psi} = \sqrt{N/M}\mathbf{F}_M\mathbf{O}\mathbf{F}_N^H$ is the sensing matrix that transforms the Nyquist CMBS into the compressive CMBS. In [52] it is shown that $\mathbf{\Psi}$ satisfies the RIP of order K for the condition

$$M = \mathcal{O}(K \log^2 K \log N) \quad (3.18)$$

where K is the signal sparsity. Finally, we can write the sparse recovery problem

$$\min_{\hat{\mathbf{P}}_{3x}^{\omega_2}} \|\mathbf{P}_{3y}^{\omega_2} - \mathbf{\Psi}\hat{\mathbf{P}}_{3x}^{\omega_2}\|_F \quad \text{subject to} \quad \|\hat{\mathbf{g}}_{3x}^{\omega_2}\|_1 \leq K \quad (3.19)$$

where $\|\cdot\|_F$ is the Frobenius norm operator, $\|\cdot\|_1$ is the ℓ_1 norm operator and $\hat{\mathbf{g}}_{3x}^{\omega_2}$ is the ICMBC vector with the entries

$$\hat{\mathbf{g}}_{3x}^{\omega_2} = [\hat{g}_{3x}^{\omega_2}(0) \quad \hat{g}_{3x}^{\omega_2}(\Delta\alpha) \quad \dots \quad \hat{g}_{3x}^{\omega_2}((N-1)\Delta\alpha)]^T. \quad (3.20)$$

Here, $\hat{\mathbf{g}}_{3x}^{\omega_2}(\cdot)$ is calculated using (3.10) for a fixed ω_2 . Note also that, (3.19) should be solved for each value of ω_2 .

ICMBC used as a sparsity constraint brings a two-way advantage: i) It reflects the cyclostationarity independent from the spectral energy, and ii) it can be calculated over the spectral bands, where the broadband propeller noise is dominant, hence rejecting unwanted additive noise and maximizing the magnitude of the propeller tonals, i.e., sparsity.

Note that, (3.19) is an MMV problem, which can be solved by greedy pursuit methods such as BCoSaMP and BIHT [52,62,63,90]. Essentially, BCoSaMP and BIHT are the algorithms given in Algorithm 1 and Algorithm 2, respectively. We merely adapt these algorithms for CMBS recovery leading to Algorithms 3 and 4. Parameters used in both algorithms are given in Table 3.1.

Algorithm 3: BCoSaMP for CMBS recovery

Input: $\mathbf{P}_{3y}^{\omega_2}, \Psi, K, \varepsilon, I$
Output: $\hat{\mathbf{P}}_{3x}^{\omega_2}$

- 1 $\hat{\mathbf{P}}_{3x}^{\omega_2}[0] = \mathbf{0}, \mathbf{Z} = \mathbf{P}_{3y}^{\omega_2}, \eta = \emptyset$
- 2 **for** $i = 0, \dots, I - 1$ **do**
- 3 $\tilde{\mathbf{P}}_{3x}^{\omega_2} = \Psi^H \mathbf{Z}$
- 4 $\rho = \eta \cup \text{supp}(\tilde{\mathbf{g}}_{3x}^{\omega_2})_{2K}$
- 5 $\hat{\mathbf{P}}_{3x}^{\omega_2} = \Psi_{\rho}^{\dagger} \mathbf{P}_{3y}^{\omega_2}$
- 6 $\eta = \text{supp}(\hat{\mathbf{g}}_{3x}^{\omega_2})_K$
- 7 $\hat{\mathbf{P}}_{3x}^{\omega_2}[i + 1] = [\hat{\mathbf{P}}_{3x}^{\omega_2}]_{\eta}$
- 8 $\mathbf{Z} = \mathbf{P}_{3y}^{\omega_2} - \Psi \hat{\mathbf{P}}_{3x}^{\omega_2}[i + 1]$
- 9 **if** $\|\mathbf{Z}\|_F / \|\mathbf{P}_{3y}^{\omega_2}\|_F \leq \varepsilon$ **or** $i \geq I$ **then**
- 10 **break**
- 11 **end**
- 12 **end**

3.4 Experimental Results

In this section we present preliminary results on CS of CMBS and compare it to SOS, i.e., CS of CMS. First, we recover the CMBS from compressive samples via (3.19) using Algorithms 3 and 4, where the approximation sparsity is determined according to (3.18). Then, we calculate the corresponding ICMBCs and compare it to the ICMBC

Algorithm 4: BIHT for CMBS recovery

Input: $\mathbf{P}_{3y}^{\omega_2}$, Ψ , K , ε , I
Output: $\hat{\mathbf{P}}_{3x}^{\omega_2}$
 1 $\hat{\mathbf{P}}_{3x}^{\omega_2}[0] = \mathbf{0}$, $\mathbf{Z} = \mathbf{P}_{3y}^{\omega_2}$
 2 **for** $i = 0, \dots, I - 1$ **do**
 3 $\tilde{\mathbf{P}}_{3x}^{\omega_2} = \hat{\mathbf{P}}_{3x}^{\omega_2}[i] + \Psi^H \mathbf{Z}$
 4 $\eta = \text{supp}(\tilde{\mathbf{g}}_{3x}^{\omega_2})_K$
 5 $\hat{\mathbf{P}}_{3x}^{\omega_2}[i + 1] = [\tilde{\mathbf{P}}_{3x}^{\omega_2}]_{\eta}$
 6 $\mathbf{Z} = \mathbf{P}_{3y}^{\omega_2} - \Psi \hat{\mathbf{P}}_{3x}^{\omega_2}[i + 1]$
 7 **if** $\|\mathbf{Z}\|_F / \|\mathbf{P}_{3y}^{\omega_2}\|_F \leq \varepsilon$ **or** $i \geq I$ **then**
 8 **break**
 9 **end**
 10 **end**

Table 3.1 : Parameters used in the Algorithms 3 and 4

$\Psi \in \mathbb{C}^{M \times N}$	Measurement matrix
$\Psi_{\rho} \in \mathbb{C}^{M \times 3K}$	Subset of measurement matrix
$\mathbf{P}_{3y}^{\omega_2} \in \mathbb{C}^{M \times L}$	Measured CMBS
$\hat{\mathbf{P}}_{3x}^{\omega_2}[i] \in \mathbb{C}^{N \times L}$	Recovered CMBS at i th iteration
$\hat{\mathbf{P}}_{3x}^{\omega_2} \in \mathbb{C}^{N \times L}$	Recovered CMBS with minimum residual norm
$\tilde{\mathbf{P}}_{3x}^{\omega_2} \in \mathbb{C}^{N \times L}$	CMBS projection estimate
$\dot{\mathbf{P}}_{3x}^{\omega_2} \in \mathbb{C}^{N \times L}$	CMBS least-squares estimate
$\tilde{\mathbf{g}}_{3x}^{\omega_2} \in \mathbb{R}^N$	ICMBC projection estimate
$\dot{\mathbf{g}}_{3x}^{\omega_2} \in \mathbb{R}^N$	ICMBC least-squares estimate
$\mathbf{Z} \in \mathbb{C}^{M \times L}$	Residual
$\text{supp}(\cdot)_K$	Support with K largest values
$[\cdot]_{\eta}$	Selects the rows with the set of indices η
K	Approximation sparsity
ε	Error tolerance
I	Maximum number of iterations
\dagger	Pseudo inverse symbol

obtained with Nyquist-rate samples, i.e., Nyquist-rate ICMBC. Similarly, we recover CMS and obtain ICMC using the Algorithms 1 and 2.

One of our main assumptions in this chapter is the non-Gaussianity of the ship-radiated propeller noise which justifies the utilization of HOS. However, it is important to know whether HOS is worth the higher computational burden. For example, to obtain (3.8),

more calculations are needed compared to computing (2.6). In terms of CS, solving (3.19) also takes more time than solving (2.25). Thus, we run experiments not just for determining the potential of HOS but also for comparing it to SOS in terms of tonal representation capacity and CS.

First, we present an example using a real-world record of a ship of opportunity. It is a 3-second-long segment at $f_s = 50$ kHz with several propeller tonals at approximately 1.67 Hz and its harmonics. Fig. 3.3 shows normalized ICMC and ICMBC in the same graphic to compare their ability to represent the propeller tonals. ICMBC yields a more prominent tonal structure using HOS. However, the theoretical sparsity of CBS (see Fig. 3.2) cannot be met due to having finite number of samples, additive noise and nonstationarity introduced by the real world conditions. This is also the case for the ICMC. On the other hand, it seems that the signal is compressible, i.e., it yields an ICMC/ICMBC that, when sorted, decay according to a power law.

To quantitatively compare the recovery performances of BCoSaMP and BIHT we define the Reconstruction SNR (RSNR) as

$$\text{RSNR} = 20 \log_{10} \frac{\|\mathbf{g}_{3x}\|_2}{\|\hat{\mathbf{g}}_{3x} - \mathbf{g}_{3x}\|_2} \quad (3.21)$$

where the Nyquist-rate ICMBC vector \mathbf{g}_{3x} and recovered one $\hat{\mathbf{g}}_{3x}$ are calculated with (3.10) for every α and over the inner triangle in the $\omega_{1,2}$ domain, i.e., $0 \leq \omega_1 \leq \pi$, $\omega_2 \leq \omega_1$ and $\omega_2 \leq \pi - \omega_1$. RSNR for ICMC is calculated similarly.

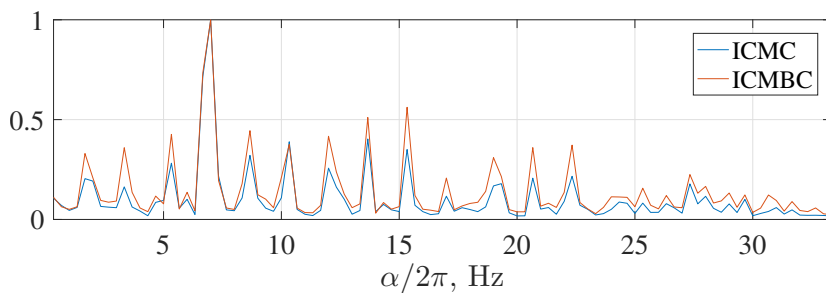


Figure 3.3 : ICMC and ICMBC with their maxima normalized to one.

For $M = 0.1N$, we observe in Fig. 3.4(a) that the recovered ICMBCs agree well with the Nyquist-rate ICMBC in terms of the frequencies of the propeller tonals. Both sparse approximation method manages to reconstruct almost all the prominent frequency peaks. However, they fail to accurately estimate the magnitudes due to

Table 3.2 : RSNR values for SOS and HOS

M	BCoSaMP (SOS)	BCoSaMP (HOS)	BIHT (SOS)	BIHT (HOS)
$0.1N$	3.88	4.64	4.72	5.88
$0.3N$	8.82	9.28	8.59	9.21
$0.5N$	13.76	11.43	13.13	11.33

insufficient number of compressive samples. Recovered ICMCs in Fig. 3.4(b) fail to represent some of the tonals that are close to noise floor.

Fig. 3.4(c) displays that increasing the number of compressive samples improves the recovery performance both in terms of tonal frequencies and magnitudes. The higher number of correctly identified tonals are due to the increased M , which enables a higher approximation sparsity K according to (3.18). This is also the case for ICMCs in Fig. 3.4(d).

Increasing M further, as given in Fig. 3.4(e), improves the recovery performance as the reconstruction error decreases. However, the sparse recovery methods still fail to accurately estimate all the magnitudes even if M is relatively high. SOS performs better for $M = 0.5N$ (Fig. 3.4(f)) which might be due to recovering less energy with a relatively high number of compressive samples. This can be observed from Table 3.2 where SOS yields better RSNR for $M = 0.5N$.

Second example involves RSNR calculations for different SNRs, modulation indices and number of compressive samples. Simulations are run for a 3-second-long signal at $f_s = 5$ kHz with 5 propeller tonals with the fundamental frequency of 5 Hz. Fig. 3.5 presents the simulation results where each RNSR value is averaged over 100 realizations. RSNR values increase with increasing μ and SNR for $M \geq 0.3$ and $\mu \geq 0.3$ since both contribute to the compressibility of the tonals by boosting the tonal magnitudes. On the other hand, insufficient number of compressive samples and weak cyclostationarity (lower μ and SNR) yield higher reconstruction errors. HOS methods yield higher RSNR values which might be due to failing to generate stationary synthetic noise. BCoSaMP and BIHT converge to almost the same performance with increasing μ and M .

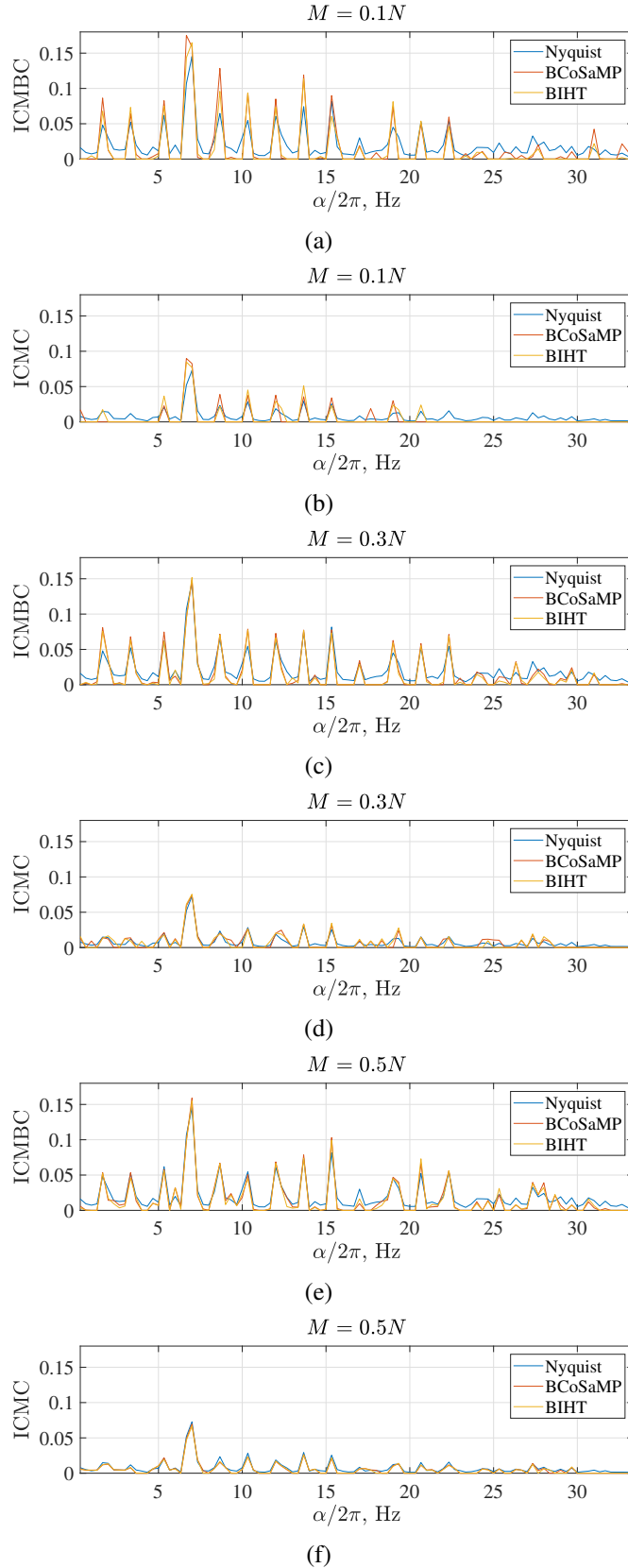


Figure 3.4 : ICMCs and ICMBCs obtained by Nyquist-rate samples, recovered with BCoSaMP and BIHT for a) ICMC with $M = 0.1N$, b) ICMBC with $M = 0.1N$, c) ICMC with $M = 0.3N$, d) ICMBC with $M = 0.3N$, e) ICMC with $M = 0.5N$, and f) ICMBC with $M = 0.5N$.

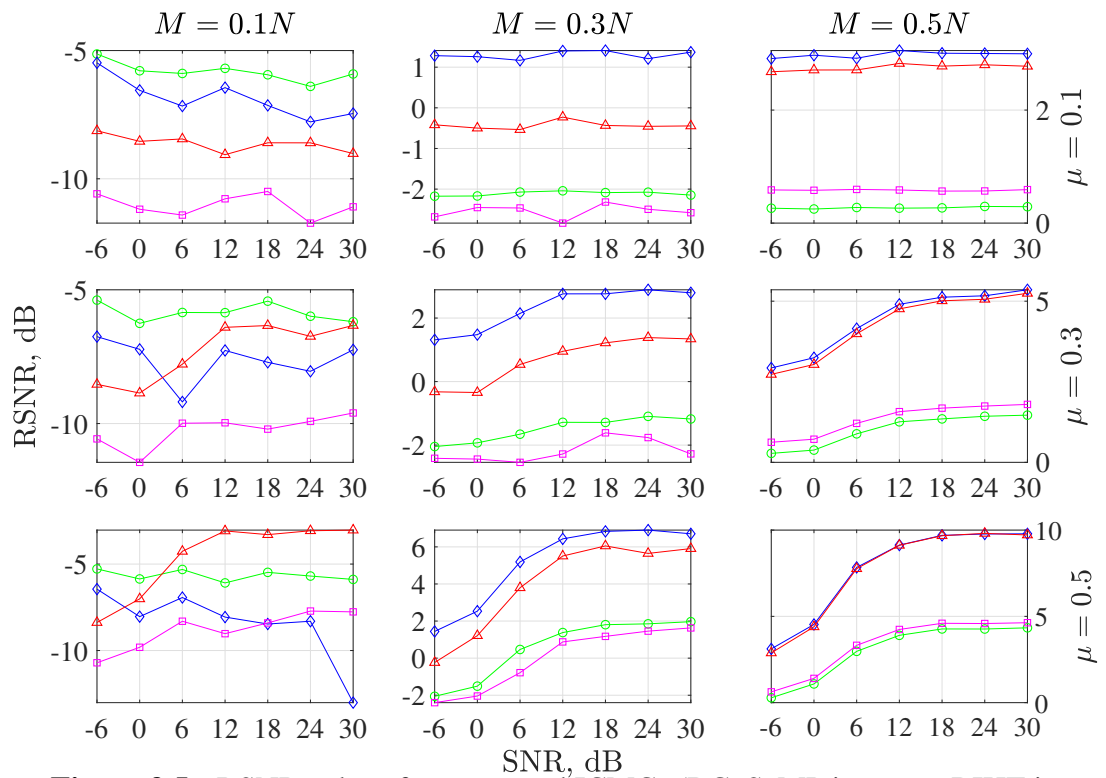


Figure 3.5 : RSNR values for recovered ICMCs (BCoSaMP in green, BIHT in magenta) and ICMBCs (BCoSaMP in blue, BIHT in red). Sub-figures in each column represent the same number of compressive samples (labeled on top) whereas each row shows the same modulation index (labeled right).

4. CYCLIC COMPRESSIVE BEAMFORMING

4.1 Introduction

DOA estimation has been an essential part of array signal processing [106] with a broad area of research including various array configurations, different signal or noise assumptions and abundant estimation methods. One of the most significant problems is the DOA estimation of a plane wave impinging on a Uniform Linear Array (ULA). While the most common application is the estimation of a monochromatic wave direction, it is not suitable when the signal of interest is of broadband nature. Underwater ship-radiated noise¹ is such a signal caused by the propeller cavitation which yields pure second-order cyclostationary signal as investigated in Chapter 2, [18,19]. It is often modeled as an amplitude modulation [8,13] where the stationary broadband part acts as the carrier modulated by the periodic part due to the propeller revolution.

Discrete-time signals can be sensed compressively and reconstructed perfectly with high probability from its samples acquired below the Nyquist-rate [23,25,30,77]. A condition needed to achieve this is that the signal must be sparse, i.e., it has smaller number of degrees of freedom compared to its length. Another condition is that the basis which transforms the signal to compressive observations should be sufficiently incoherent [30]. The mathematical model behind DOA estimation fits above conditions where sparsity emerges as there are much fewer sources compared to the whole DOA grid and the array manifold matrix acts as an incoherent basis.

CS and its application in DOA estimation, i.e., Compressive Beamformer (CB) [32]–[49] introduces many advantages over classical methods such as the conventional

This chapter is based on the paper “U. Firat and T. Akgül, Compressive Beamformer for Direction-of-Arrival Estimation of Cyclostationary Propeller Noise, in *Signal Processing*, Volume 214, 2024, 109221, ISSN 0165-1684, <https://doi.org/10.1016/j.sigpro.2023.109221>.”

¹The signal radiated underwater is called noise due to its stochastic nature.

beamformer [107], the Minimum Variance Distortionless Response (MVDR) [108] and Multiple Signal Classification (MUSIC) [109] in terms of resolution, performing under correlated sources and limited number of snapshots.

In [32], authors propose a convex optimization approach with ℓ_1 minimization to estimate DOAs for narrowband and broadband signals. They also utilize Singular Value Decomposition (SVD) for robustness to noise and to reduce the computational complexity. Performance of their so-called ℓ_1 -SVD is compared to the classical methods in terms of numerical bias and variance together with source separation and number of sources. Authors of [39] introduce a similar CB based on an ℓ_1 minimization reweighed to enhance sparsity. Additionally, they investigate the limitations of their approach for coherence, resolution and basis mismatch which is one of the main challenges in CB. It arises when DOAs do not coincide with the spatial grid points which can be overcome by grid refinement [32] or replacing the discrete ℓ_1 norm with its continuous counterpart, i.e., total variation or atomic norm [43,46,47,110,111].

Unlike the classical methods, CB performs even with a single snapshot [38,40,42] which sometimes becomes crucial in sonar signal processing due to physical drawbacks such as the limitations in underwater sound propagation [40].

All these methods assume either deterministic (narrowband) or stationary (broadband) source signals which may cause degraded performance in case of closely-spaced cyclostationary sources. Although there are several cyclic DOA estimation methods such as Cyclic MUSIC [112] introduced for telecommunication signals, it is mandatory to know the carrier frequency beforehand to estimate cyclic statistics. On the other hand, propeller tonals (frequency components caused by propeller revolution) are unknown prior to DOA estimation which creates a need to a novel cyclic DOA estimation method.

We propose to utilize a cyclic CS method which seeks sparsity both in spatial and cyclic frequency domains using CMS [19]. This enables better resolution and less estimation error by seeking sparsity in cyclic frequency domain where different sources are assumed to have different propeller tonals. Moreover, the proposed Cyclic CB (CCB) enjoys other advantages that CB offers such as performing under correlated

sources and limited number of snapshots. Fig. 4.1 shows an example, comparing the classical and compressive methods for both uncorrelated and correlated cyclostationary sources.

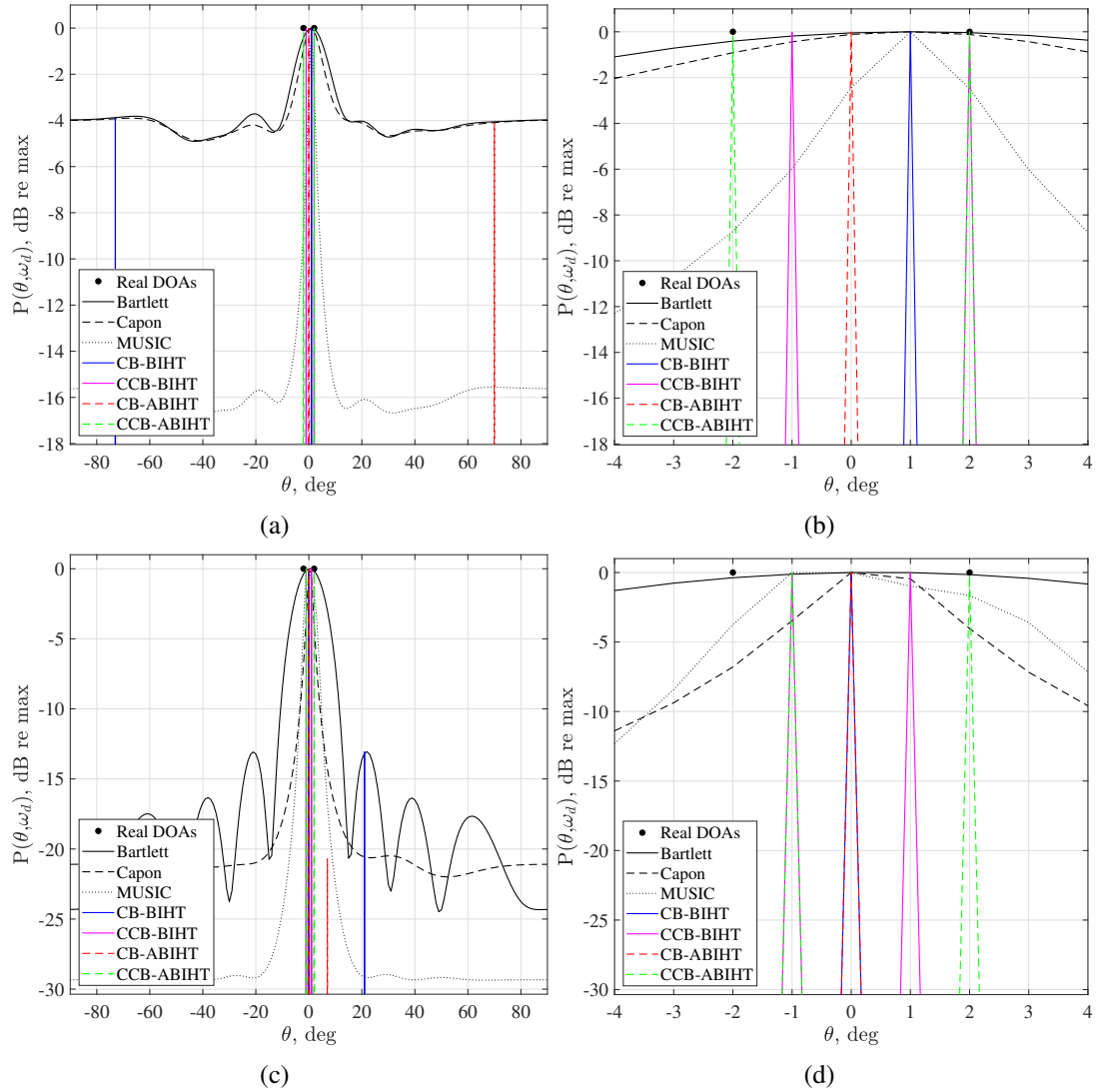


Figure 4.1 : Comparison of DOA estimation methods with an 8-sensor ULA for two closely-spaced sources, i.e., $\theta_0 = -2^\circ$ and $\theta_1 = 2^\circ$ with equal modulation indices of 0.5. The spatial power spectra are shown for SNR=0 dB with a) equally powered uncorrelated sources and b) the grid magnified around the true DOAs; for SNR=20 dB with c) equally powered correlated sources and again d) the grid magnified around the true DOAs.

To summarize, our main contributions are

- 1) the proposal of a novel method for DOA estimation of second-order cyclostationary sources;
- 2) the analytical derivation of the MSE of CCB;

3) the performance comparison of classical and compressive DOA estimators.

The remainder of this chapter is as follows. We give the DOA estimation problem in Section 4.2. In Section 4.3, we provide a brief introduction to CS and its use in DOA estimation via compressive beamforming. We propose our method CCB in Section 4.4. In Section 4.5 and 4.6 we present the analytical results on the performance of the CCB and give numerical examples, respectively. Finally, we discuss our findings in Section 4.7.

4.2 DOA Estimation

4.2.1 The narrowband model

Consider a plane wave impinging on a linear array of hydrophone sensors with a DOA angle $\theta \in [-90^\circ, 90^\circ]$ with respect to the array axis. The propagation delay from the k th potential source to each sensor is described as simple phase shifts by the steering vector

$$\mathbf{a}(\theta_k) = \frac{1}{\sqrt{M}} [e^{j(2\pi/\lambda)r_0 \sin \theta_k} \quad e^{j(2\pi/\lambda)r_1 \sin \theta_k} \quad \dots \quad e^{j(2\pi/\lambda)r_{M-1} \sin \theta_k}]^T \quad (4.1)$$

where λ is the wavelength and $r_m = md$, $m = 0, 1, \dots, M-1$, comprises the sensor locations for a ULA with M being the number of sensors and d is the distance between two sensors. Then, the array manifold matrix can be formed as

$$\mathbf{A} = [\mathbf{a}(\theta_0) \quad \mathbf{a}(\theta_1) \quad \dots \quad \mathbf{a}(\theta_{Q-1})] \quad (4.2)$$

where Q is the number of possible source directions.

In the presence of additive noise and multiple snapshots the measurements can be written as

$$\mathbf{X} = \mathbf{A}\mathbf{S} + \mathbf{N} \quad (4.3)$$

where $\mathbf{S} \in \mathbb{C}^{Q \times L}$ contains Q source signals with the length L while $\mathbf{X} \in \mathbb{C}^{M \times L}$, $\mathbf{N} \in \mathbb{C}^{M \times L}$ represent the sensor measurements and additive noise, respectively. This model is based on the narrowband assumption where the steering matrix is formed using the angular frequency $\omega = 2\pi c/\lambda$ with c being the sound speed.

One of the simplest nonparametric source localization methods is the conventional beamformer (Bartlett's method) [107] which coherently combines the sensor outputs to enhance the signal yielding the spatial power spectrum

$$P_{\text{Bartlett}}(\theta) = \mathbf{a}(\theta)^H \hat{\mathbf{R}}_x \mathbf{a}(\theta) \quad (4.4)$$

where $\hat{\mathbf{R}}_x = \mathbf{X}\mathbf{X}^H/L$ is the sample cross covariance matrix estimate. Bartlett's method is quite simple yet suffers from presence of sidelobes and Rayleigh resolution limit, i.e., two plane waves are resolvable if they are at least $\Delta\theta = \arcsin(\lambda/Md)^\circ$ apart [106, Ch. 2].

Another nonparametric method, MVDR, also known as, "Capon's method" assumes a filter that minimizes the variance at its output [108]. It is shown that Capon's method does not depend on the filter coefficients leading to the spatial power spectrum

$$P_{\text{Capon}}(\theta) = \frac{1}{\mathbf{a}(\theta)^H \hat{\mathbf{R}}_x^{-1} \mathbf{a}(\theta)}. \quad (4.5)$$

Empirical analysis show that Capon's method is expected to provide better resolution compared to Bartlett's method, e.g., resolving closely-spaced sources, due to its higher statistical stability [113, Ch. 5].

Eigenanalysis based methods rely on the property that the noise subspace eigenvectors of a Toeplitz covariance matrix are orthogonal to the signal subspace vectors. In the earliest subspace based method which is called Pisarenko Harmonic Decomposition (PHD), the eigenvector associated with the minimum eigenvalue of the estimated autocorrelation matrix is used for spectrum estimation [114]. MUSIC method outperforms PHD using all the noise subspace [109]. MUSIC spatial power spectrum is given as

$$P_{\text{MUSIC}}(\theta) = \frac{1}{\sum_{m=M_0+1}^M |\mathbf{a}(\theta)^H \mathbf{v}_m|^2} \quad (4.6)$$

where \mathbf{v}_m is the m th eigenvector associated with the m th eigenvalue of $\hat{\mathbf{R}}_x$ and M_0 is the signal subspace dimension. MUSIC promises higher resolution however the sources need to be sufficiently uncorrelated for the covariance matrix to be nonsingular [113, Ch. 6].

4.2.2 The broadband model

Since ship-radiated noise is of broadband nature narrowband assumption of (4.3) does not hold, i.e., the delays cannot be represented as simple phase shifts as in (4.1). Thus, we need to reformulate the narrowband model to estimate DOAs in multiple frequency bands. Such a model is readily available via DFT beamformer [106, Ch. 6]. By transforming the sensor measurements into frequency domain we can rewrite (4.3) as

$$\mathbf{X}(\omega, t_i) = \mathbf{A}(\omega)\mathbf{S}(\omega, t_i) + \mathbf{N}(\omega, t_i) \quad (4.7)$$

where $\mathbf{X}(\omega, t_i) \in \mathbb{C}^{M \times I}$, $\mathbf{S}(\omega, t_i) \in \mathbb{C}^{Q \times I}$ and $\mathbf{N}(\omega, t_i) \in \mathbb{C}^{M \times I}$ are Short-Time FT (STFT) matrices of observations, sources and noise, respectively. By using N -point DFT at each time snapshot with a shifting size of R , one obtains $I = \lfloor \frac{L-N}{R} \rfloor + 1$ snapshots at times $t_i = iRT_s, i = 0, 1, \dots, I-1$ where T_s is the sampling period.

All the methods aforementioned in Section 4.2.1 are applicable to solve for (4.7) at each frequency ω , separately.

4.3 Compressive Sensing

4.3.1 Sparse approximation

Sparse approximation in DOA estimation seeks to recover the sources which are sparse in spatial dimension. Given the sensor observations $\mathbf{x} \in \mathbb{C}^M$, the manifold (measurement) matrix $\mathbf{A} \in \mathbb{C}^{M \times Q}$ and the sparse source vector $\mathbf{s} \in \mathbb{C}^Q$ with $M < Q$ one can write the SMV sparse approximation problem as

$$\min_{\mathbf{s}} \|\mathbf{s}\|_0 \quad \text{subject to} \quad \|\mathbf{x} - \mathbf{A}\mathbf{s}\|_2 \leq \varepsilon \quad (4.8)$$

where $\|\cdot\|_0$ is the ℓ_0 pseudo-norm operator and $\varepsilon > 0$ is the error tolerance [31]. The noisy sparse approximation in (4.8) can be reformulated as

$$\min_{\mathbf{s}} \|\mathbf{x} - \mathbf{A}\mathbf{s}\|_2 \quad \text{subject to} \quad \|\mathbf{s}\|_0 \leq K \quad (4.9)$$

where K is the number of sources to be sought for.

The problems in (4.8) and (4.9) are non-deterministic polynomial-time hard problems which reduce to a tractable one by relaxing the combinatorial ℓ_0 pseudo-norm to its closest convex counterpart, i.e., ℓ_1 norm [31]. In DOA estimation, convex optimization and greedy pursuits are most commonly utilized methods to solve for (4.8) and (4.9) as in CS for data compression. Again, we adopt the greedy pursuit methods due to their ease of use and speed.

4.3.2 Sensing matrix

There are random matrices satisfying the RIP formed by sampling i.i.d. entries from the normal, Bernoulli or another sub-Gaussian distribution [86] and partial DFT matrices [26,87,88]. However in problems like DOA estimation on a ULA, the array manifold matrix acts as a deterministic sensing matrix which might not satisfy the RIP where coherence is utilized for the fitness of the matrix for CS. The coherence of the orthonormal matrix \mathbf{A} is defined as

$$\psi(\mathbf{A}) = \max_{0 \leq i \neq j \leq Q-1} |\mathbf{a}_i^H \mathbf{a}_j| \quad (4.10)$$

where the maximum inner product between the column vectors \mathbf{a}_i of \mathbf{A} is searched over all Q columns.

RIP and coherence are related by the following lemma from [29]

Lemma 1 *If \mathbf{A} has unit-norm columns and coherence $\psi(\mathbf{A}) = \psi$, then \mathbf{A} satisfies the RIP of order K with $\xi_K = (K - 1)\psi$ for all $K < 1/\psi$.*

4.3.3 Compressive beamformer

Suppose we rewrite (4.8) as an MMV problem by convexly relaxing it to solve (4.3) leading to

$$\min_{\hat{\mathbf{s}}_{\ell_2}} \|\hat{\mathbf{s}}_{\ell_2}\|_1 \quad \text{subject to} \quad \|\mathbf{X} - \mathbf{A}\hat{\mathbf{S}}\|_F \leq \varepsilon \quad (4.11)$$

where

$$\hat{\mathbf{s}}_{\ell_2} = \text{diag}(\hat{\mathbf{S}}\hat{\mathbf{S}}^H)^{\circ 1/2} \quad (4.12)$$

represents the vector formed by the ℓ_2 norms of the row vectors of $\hat{\mathbf{S}}$, $(\cdot)^{\circ 1/2}$ is the Hadamard (element-wise) square-root of a vector and $\varepsilon > 0$ is the error tolerance.

Since the SMV problem is transformed into an MMV problem ℓ_2 norm in (4.8) becomes the Frobenius matrix norm. While CB for SMV has been studied in a number of papers [33,34,38]–[44,47]–[49] the problem in (4.11) suits to the MMV DOA estimation and has been treated in several papers [32,35]–[37,39,42,45,46]. This approach is also useful to exploit block-sparsity of the sources, i.e., the columns in $\hat{\mathbf{S}}$ are jointly sparse for the rows representing source directions.

Now let us assess the fitness of the array manifold matrix for sparse recovery by inspecting the Gram matrix of \mathbf{A} , i.e., $\mathbf{G}_\mathbf{A} = \mathbf{A}^H \mathbf{A}$. Fig. 4.2 shows $|\mathbf{G}_\mathbf{A}|$ of a ULA at array design frequency ω_d , such that $d = \lambda/2$ and $\omega_d/2$ with $M = 8$ and $M = 64$ sensors, respectively.

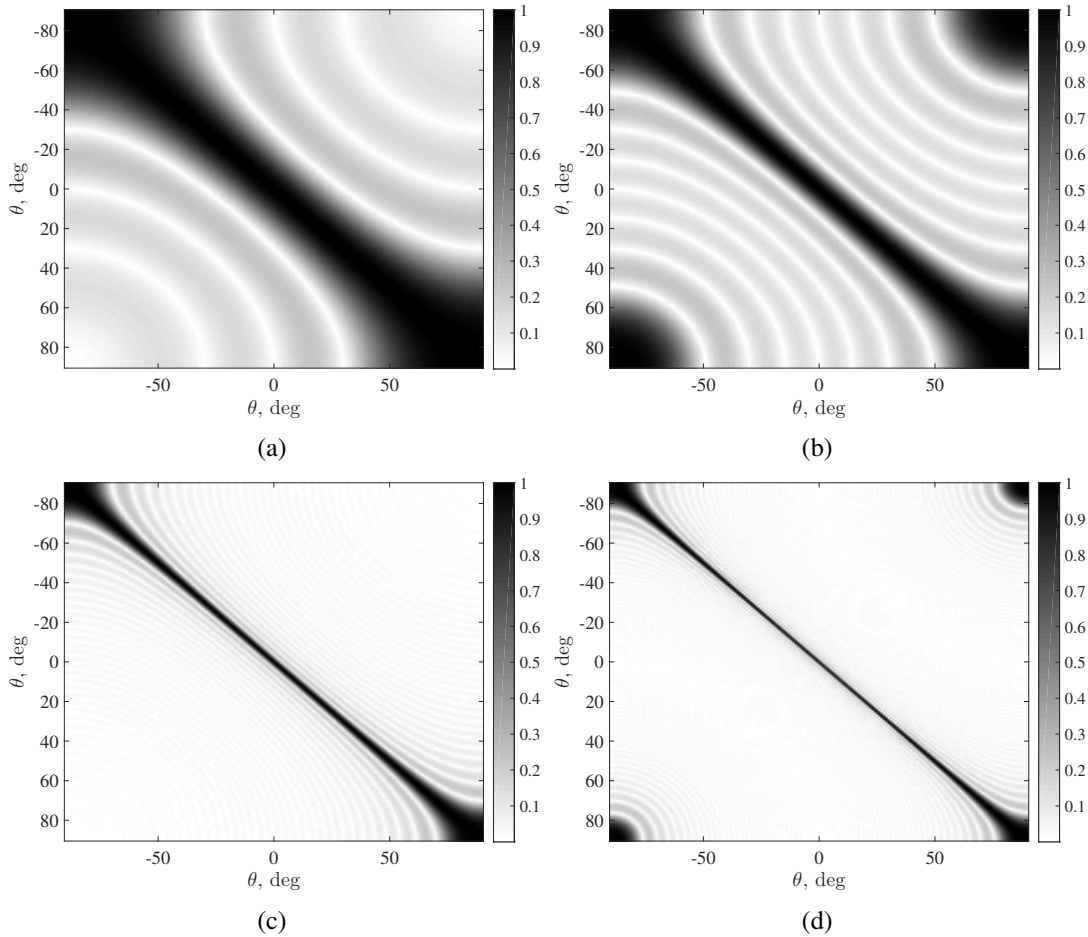


Figure 4.2 : Absolute Gram matrices for a ULA with a) $M = 8$ at $\omega_d/2$, b) $M = 8$ at ω_d , c) $M = 64$ at $\omega_d/2$, and d) $M = 64$ at ω_d .

Notice the effect of the frequency and number of sensors on the mutual coherence of \mathbf{A} . It becomes much smaller with increasing number of sensors and frequency. This in turn yields a lower RIC which ensures better sparse recovery.

While convex optimization is utilized to solve for (4.11) greedy pursuits are faster alternatives for which we can rewrite (4.11) as

$$\min_{\hat{\mathbf{S}}} \|\mathbf{X} - \mathbf{A}\hat{\mathbf{S}}\|_F \quad \text{subject to} \quad \|\hat{\mathbf{s}}_{\ell_2}\|_1 \leq K \quad (4.13)$$

which gives the solution to narrowband DOA estimation problem. In order to solve for the broadband model given in (4.7), we consider each spectral band separately such as

$$\min_{\hat{\mathbf{S}}(\omega, t_i)} \|\mathbf{X}(\omega, t_i) - \mathbf{A}(\omega)\hat{\mathbf{S}}(\omega, t_i)\|_F \quad \text{subject to} \quad \|\hat{\mathbf{s}}_{\ell_2}(\omega)\|_1 \leq K. \quad (4.14)$$

Note that ℓ_2 norms are computed for every ω .

4.4 Cyclic Compressive Beamformer

4.4.1 Cyclostationary propeller noise

The propeller noise is often modeled with amplitude modulation when propeller cavitation occurs [8,13,52,55]–[60]. Here, we consider the modulating signal as a single tonal to easily derive the CCB. However, it is straightforward to generalize the problem when there are multiple propeller tonals. We can write the complex-valued propeller noise model as

$$s(t) = [1 + \mu \cos(\alpha_0 t)]c(t) \quad (4.15)$$

where $[1 + \mu \cos(\alpha_0 t)]$ modulates the amplitude of the broadband propeller noise $c(t)$ with the modulation index μ and the propeller tonal frequency α_0 rad/s [8]. Under the assumption that $c(t)$ is a zero-mean wide-sense stationary random process [8,11,13,19,59,83,84] and using (4.15) with Euler's formula we can write the instantaneous autocorrelation function of $s(t)$ as

$$\begin{aligned} \mathbf{R}_s(v, t) &\triangleq \mathbb{E}\{s(v)s(t)^*\} \\ &= \left[1 + \frac{\mu}{2} e^{j\alpha_0 t} e^{-j\alpha_0 \tau} + \frac{\mu}{2} e^{-j\alpha_0 t} e^{j\alpha_0 \tau} + \frac{\mu}{2} e^{j\alpha_0 t} + \frac{\mu}{2} e^{-j\alpha_0 t} + \frac{\mu^2}{4} e^{j2\alpha_0 t} e^{-j\alpha_0 \tau} \right. \\ &\quad \left. + \frac{\mu^2}{4} e^{-j2\alpha_0 t} e^{j\alpha_0 \tau} + \frac{\mu^2}{4} e^{j\alpha_0 \tau} + \frac{\mu^2}{4} e^{-j\alpha_0 \tau} \right] \mathbf{R}_c(\tau) = \mathbf{R}_s(\tau, t) \end{aligned} \quad (4.16)$$

where $\mathbb{E}\{\cdot\}$ is the expected value operator, $\mathbf{R}_c(\tau)$ is the autocorrelation function of $c(t)$ and $\tau = t - v$. Note that $s(t)$ is nonstationary, i.e., $\mathbf{R}_s(v, t) = \mathbf{R}_s(\tau, t)$ depends both on the time index t and the lag τ . However, $\mathbf{R}_s(\tau, t) = \mathbf{R}_s(\tau, t + \zeta T)$, thus $s(t)$

is cyclostationary (periodically stationary) with the period $T = 2\pi/\alpha_0$ sec and $\zeta \in \mathbb{Z}$. Since the periodicity is in the second order autocorrelation function, $s(t)$ is said to be second order wide-sense cyclostationary.

In order to show the sparsity in the cyclic frequency domain the SCF of $s(t)$,

$$\begin{aligned} S_s(\omega, \alpha) = & \left[S_c(\omega) + \frac{\mu^2}{4} \left(S_c(\omega - \alpha_0) + S_c(\omega + \alpha_0) \right) \right] \delta(\alpha) \\ & + \frac{\mu}{2} \left(S_c(\omega + \alpha_0) + S_c(\omega) \right) \delta(\alpha - \alpha_0) + \frac{\mu}{2} \left(S_c(\omega - \alpha_0) + S_c(\omega) \right) \delta(\alpha + \alpha_0) \\ & + \frac{\mu^2}{4} S_c(\omega + \alpha_0) \delta(\alpha - 2\alpha_0) + \frac{\mu^2}{4} S_c(\omega - \alpha_0) \delta(\alpha + 2\alpha_0) \end{aligned} \quad (4.17)$$

can be utilized [52] which is related to $R_s(\tau, t)$ through FS expansion over t and FT over τ [18] with $S_c(\omega)$ being the PSD of $c(t)$. Here, t and τ are transformed into their dual frequency variables α and ω , respectively.

4.4.2 Cyclic modulation spectrum

CMS offers a fast and reliable approximation of the SCF depending only on the DFT which enables the matrix operations in developing a cyclic beamformer. Let $s[n] \triangleq s(nT_s), n = 0, \dots, L-1$, be the L -long source signal which is the discretized counterpart of $s(t)$ given in (4.15) with the sampling frequency of $f_s = 1/T_s$. An N -long analysis window $w[n]$ is used to take R -sample-apart overlapped snapshots from the signal yielding I snapshots. Then the STFT of the windowed signal can be calculated as

$$S_{\Delta\omega}(\omega, t_i) = T_s \sum_{n=iR}^{iR+N-1} s[n]w[n-iR]e^{-j\omega nT_s} \quad (4.18)$$

which returns the filtered signal in a narrow band with center frequency ω and width $\Delta\omega \sim 2\pi/NT_s$ at times $t_i = iRT_s, i = 0, \dots, I-1$ [19]. By taking the DFT of the $|S_{\Delta\omega}(\omega, t_i)|^2$ over its time variable that transforms t_i to its dual cyclic frequency variable α we arrive at the CMS given as

$$P_s(\omega, \alpha) = \frac{1}{I} \sum_{i=0}^{I-1} |S_{\Delta\omega}(\omega, t_i)|^2 e^{-j\alpha t_i} \quad (4.19)$$

which is basically the DFT of the spectrogram of the signal. Here, the spectral and cyclic frequency resolutions are $\Delta\omega$ and $\Delta\alpha \sim 2\pi/LT_s$, respectively [19]. Note that, the maximum cyclic frequency cannot exceed $\Delta\omega$ by the uncertainty principle, i.e., $\Delta T \Delta\omega \geq 2\pi$ where the time resolution is $\Delta T = 2\pi/\alpha$.

Note that, in earlier chapters, CMS matrix was calculated for a signal to represent its sparsity in cyclic frequency domain. It is then used to derive a linear relationship between compressive and Nyquist-rate CMS matrices to develop a CS scheme for data compression. Here, CMS will be used to form matrices of several source signals for array signal processing. Thus, these matrices represent both spatial and cyclic sparsity for high resolution DOA estimation.

4.4.3 Cyclic sparse approximation

Since the signal given in (4.15) is cyclostationary, we employ the broadband model (4.7) for DOA estimation with (4.14) modified as

$$\min_{\hat{\mathbf{S}}(\omega, t_i)} \|\mathbf{X}(\omega, t_i) - \mathbf{A}(\omega)\hat{\mathbf{S}}(\omega, t_i)\|_F \quad \text{subject to} \quad \|\hat{\mathbf{s}}_\alpha(\omega)\|_1 \leq K \quad (4.20)$$

where $\hat{\mathbf{s}}_\alpha(\omega)$ is the vector containing information on cyclostationarity on each row of $\hat{\mathbf{S}}(\omega, t_i)$. In order to form such a vector, we can utilize the CMS matrix of $\hat{\mathbf{S}}(\omega, t_i)$ given as

$$\hat{\mathbf{P}}_s(\omega, \alpha) = |\hat{\mathbf{S}}(\omega, t_i)|^{\circ 2} \mathbf{F}_I^H \quad (4.21)$$

where $(\cdot)^{\circ 2}$ is the Hadamard (element-wise) square of a matrix and \mathbf{F}_I is $I \times I$ DFT matrix. Notice that (4.21) represents the matrix formed by applying (4.19) at each row of $|\hat{\mathbf{S}}(\omega, t_i)|^{\circ 2}$. Now that we have $\hat{\mathbf{P}}_s(\omega, \alpha)$ with rows representing the spatial dimension and columns containing the cyclic frequency components at the spectral frequency ω , we can form a spatial vector containing cyclostationary source directions. Assume that we have multiple cyclostationary sources impinging on a ULA at different angles with different cyclic frequencies. Then we can define the vector

$$\hat{\mathbf{s}}_\alpha(\omega) = \max_{\alpha} |\hat{\mathbf{P}}_s(\omega, \alpha)| \quad (4.22)$$

consisting of maximum cyclic components at each direction.

There are many greedy pursuit methods [31,62,63,90] readily available to solve for (4.20). We select BIHT [52,62,90] for its computational efficiency and lower approximation error [62]. Our adaptation of BIHT for source matrix estimation is presented in Algorithm 5.

Algorithm 5: BIHT for source matrix estimation

Input: $\mathbf{X}(\omega_n, t_i)$ and $\mathbf{A}(\omega_n)$, $n \in [0, N-1]$, K , ε , J

Output: $\hat{\mathbf{S}}(\omega_n, t_i)$, $n \in [0, N-1]$

```

1  $\hat{\mathbf{S}}(\omega_n, t_i)^{[0]} = \mathbf{0}$ ,  $\mathbf{B}_n = \mathbf{X}(\omega_n, t_i)$ 
2 for  $j = 0, \dots, J-1$  do
3    $\tilde{\mathbf{S}}(\omega_n, t_i) = \hat{\mathbf{S}}(\omega_n, t_i)^{[j]} + \mathbf{A}(\omega_n)^H \mathbf{B}_n$ 
4    $\eta = \text{supp}[\gamma]_K$ 
5    $\hat{\mathbf{S}}(\omega_n, t_i)^{[j+1]} = [\tilde{\mathbf{S}}(\omega_n, t_i)]_\eta$ 
6    $\mathbf{B}_n = \mathbf{X}(\omega_n, t_i) - \mathbf{A}(\omega_n) \hat{\mathbf{S}}(\omega_n, t_i)^{[j+1]}$ 
7   if  $\|\mathbf{B}_n\|_F / \|\mathbf{X}(\omega_n, t_i)\|_F \leq \varepsilon$  or  $j \geq J$  then
8     break
9   end
10 end

```

BIHT starts with a projection estimate given as

$$\tilde{\mathbf{S}}(\omega, t_i) = \mathbf{A}(\omega)^H \mathbf{X}(\omega, t_i) \quad (4.23)$$

which is essentially the array output of the conventional beamformer. Likewise (4.21) we can write the CMS matrix of the projection estimate as

$$\tilde{\mathbf{P}}_s(\omega, \alpha) = |\tilde{\mathbf{S}}(\omega, t_i)|^{\circ 2} \mathbf{F}_I^H. \quad (4.24)$$

Using (4.7) and (4.23) we can rewrite (4.24) as

$$\tilde{\mathbf{P}}_s(\omega, \alpha) = |\mathbf{A}(\omega)^H \mathbf{A}(\omega) \mathbf{S}(\omega, t_i) + \mathbf{A}(\omega)^H \mathbf{N}(\omega, t_i)|^{\circ 2} \mathbf{F}_I^H. \quad (4.25)$$

Notice that $\mathbf{A}(\omega)^H \mathbf{A}(\omega)$ is the Gram matrix of the array for ω . Apart from the mutual coherence it has a critical role in estimating the source directions. For a single source, the Gram matrix has no effect on the estimated DOA since the true STFT matrix of the sources has a single nonzero row. However, when there are multiple sources, the product $\mathbf{A}(\omega)^H \mathbf{A}(\omega) \mathbf{S}(\omega, t_i)$ causes each source to contribute to every other source which eventually bias the estimator [115, Ch. 2]. This negative effect inherent to the conventional beamformer can be eased via spectral averaging. We can make use of the block-sparsity in every spectral frequency, i.e., the signal is broadband yet impinges on the same angle. Hence, Algorithm 5 can be improved yielding the Averaged BIHT (ABIHT) given in Algorithm 6. The sparsity is sought after averaging spectral components of the CMS matrices as

$$\tilde{s}_\alpha = \max_\alpha \left| \frac{1}{N} \sum_{n=0}^{N-1} \tilde{\mathbf{P}}_s(\omega_n, \alpha) \right| \quad (4.26)$$

where we call the term inside the absolute value operator, the Averaged CMS (ACMS) matrix.

The same approach can be applied to the CB where $\tilde{\mathbf{s}}_{\ell_2}(\omega_n)$ should be averaged over spectral frequencies

$$\tilde{\mathbf{s}}_{\ell_2} = \frac{1}{N} \sum_{n=0}^{N-1} \tilde{\mathbf{s}}_{\ell_2}(\omega_n). \quad (4.27)$$

Note that in Algorithm 5, the sparsity is searched over $\gamma = \tilde{\mathbf{s}}_{\ell_2}(\omega_n)$ for CB or $\gamma = \tilde{\mathbf{s}}_{\alpha}(\omega_n)$ for CCB and in Algorithm 6 over $\gamma = \tilde{\mathbf{s}}_{\ell_2}$ for CB or $\gamma = \tilde{\mathbf{s}}_{\alpha}$ for CCB. The definitions of the parameters used in both algorithms are given in Table 4.1.

Estimated STFT matrix of the sources from both algorithms, is used to obtain the spatial power spectrum which should reveal the DOAs as distinct peaks. Then we utilize, as in [32], a grid refinement process to overcome the basis mismatch. Briefly, after estimating the DOA with a uniform rough grid, we split the grid around the rough estimate in N_p subgrid points and repeat this process N_r times leading to a fine DOA estimate.

Algorithm 6: ABIHT for source matrix estimation

Input: $\mathbf{X}(\omega_n, t_i)$'s and $\mathbf{A}(\omega_n)$'s $\forall n \in [0, N-1], K, \varepsilon, J$
Output: $\hat{\mathbf{S}}(\omega_n, t_i)$'s $\forall n \in [0, N-1]$

- 1 **for** $n = 0, \dots, N-1$ **do**
- 2 | $\hat{\mathbf{S}}(\omega_n, t_i)^{[0]} = \mathbf{0}, \mathbf{B}_n = \mathbf{X}(\omega_n, t_i)$
- 3 **end**
- 4 **for** $j = 0, \dots, J-1$ **do**
- 5 | **for** $n = 0, \dots, N-1$ **do**
- 6 | $\tilde{\mathbf{S}}(\omega_n, t_i) = \hat{\mathbf{S}}(\omega_n, t_i)^{[j]} + \mathbf{A}(\omega_n)^H \mathbf{B}_n$
- 7 | **end**
- 8 | $\eta = \text{supp}[\gamma]_K$
- 9 | **for** $n = 0, \dots, N-1$ **do**
- 10 | $\hat{\mathbf{S}}(\omega_n, t_i)^{[j+1]} = [\tilde{\mathbf{S}}(\omega_n, t_i)]_{\eta}$
- 11 | $\mathbf{B}_n = \mathbf{X}(\omega_n, t_i) - \mathbf{A}(\omega_n) \hat{\mathbf{S}}(\omega_n, t_i)^{[j+1]}$
- 12 | **end**
- 13 | **for** $n = 0, \dots, N-1$ **do**
- 14 | $y_n = \|\mathbf{B}_n\|_F / \|\mathbf{X}(\omega_n, t_i)\|_F$
- 15 | **end**
- 16 | **if** $\|y\|_2 \leq \varepsilon$ **or** $j \geq J$ **then**
- 17 | **break**
- 18 | **end**
- 19 **end**

Table 4.1 : Parameters used in the Algorithms 5 and 6

$\mathbf{A}(\omega_n) \in \mathbb{C}^{M \times Q}$	Sensing/manifold matrix
$\mathbf{X}(\omega_n, t_i) \in \mathbb{C}^{M \times I}$	Observations STFT matrix
$\hat{\mathbf{S}}(\omega_n, t_i)^{[j]} \in \mathbb{C}^{Q \times I}$	Estimated source STFT matrix at j th iteration
$\hat{\mathbf{S}}(\omega_n, t_i) \in \mathbb{C}^{Q \times I}$	Estimated source STFT matrix with minimum residual norm
$\tilde{\mathbf{S}}(\omega_n, t_i) \in \mathbb{C}^{Q \times I}$	Projection estimate of source STFT matrix
$\mathbf{B}_n \in \mathbb{C}^{M \times I}$	Residual
γ	Sparsity representation vector
y_n	Ratio of the residual and sensor Frobenius norm for ω_n
$\mathbf{y} \in \mathbb{R}^N$	Vector consisting of y_n for all ω_n
$\text{supp}[\cdot]_K$	Support with K largest values
$[\cdot]_\eta$	Selects the rows with the set of indices η
K	Approximation sparsity
ε	Error tolerance
J	Maximum number of iterations

4.4.4 Computational complexity of the CCB

Computational complexity of the CCB realized with Algorithm 5 is mainly based on matrix multiplications. In Step 3, $\mathbf{A}(\omega_n)^H \mathbf{B}_n$ is $\mathcal{O}(QIM)$. To obtain γ in step 4, CMS matrix can be calculated with the Fast FT (FFT) applied to each row of $|\tilde{\mathbf{S}}(\omega, t_i)|^2$ leading to $\mathcal{O}(QI \log I)$ operations. Similar to step 3, $\mathbf{A}(\omega_n) \hat{\mathbf{S}}(\omega_n, t_i)^{[j+1]}$ in step 6 is $\mathcal{O}(QIM)$. When we neglect norm calculations and finding support of γ , which is essentially a sort algorithm, overall complexity reaches approximately to $\mathcal{O}(NJQI[M + \log I])$ for N spectral bands and J iterations. CCB with Algorithm 6 has a similar complexity with a minor difference, i.e., batch processing of N spectral bands in J iterations. CB with Algorithm 5 and 6 requires the same operations except the calculation of sparsity vector γ which is approximately $\mathcal{O}(Q^2I)$ by (4.12).

Table 4.2 summarizes approximate computational complexity of several DOA estimation methods. Classical techniques mainly consist of matrix multiplications, inversion and eigenvalue decomposition [116,117]. Number of sensors M and dimension of the DOA grid Q play critical role for classical methods since they appear

in quadratic and cubic forms in the complexity. Main disadvantage of compressive techniques is that they require multiple number of iterations (up to J) until the stopping criteria is met. CCB is expected to be faster than CB since $\log I \ll Q$, i.e., the logarithm of number of snapshots is usually much less than a fine DOA grid size.

Table 4.2 : Computational complexity of DOA estimation methods

Method	Operations	Complexity
Bartlett	Matrix multiplications	$\mathcal{O}(N[M^2I + QM^2 + Q^2M])$
Capon	Matrix multiplications and inversion	$\mathcal{O}(N[M^2I + M^3 + QM^2 + Q^2M])$
MUSIC	Matrix multiplications and eigenvalue decomposition	$\mathcal{O}(N[M^2I + M^3 + M^2Q])$
CB	Matrix multiplications	$\mathcal{O}(NJQI[M + Q])$
CCB	Matrix multiplications and FFT	$\mathcal{O}(NJQI[M + \log I])$

4.5 Analytical Performance of the CCB

4.5.1 Asymptotic CMS

Since the CCB is based on the conventional beamformer (4.4) it is asymptotically biased [115, Ch. 2], [118]. To define the asymptotic CMS each entry of (4.25) can be simply written as

$$\tilde{P}(\theta_k, \omega, \alpha_l) = \frac{1}{I} \sum_{i=0}^{I-1} |Z(\theta_k, \omega, t_i)|^2 e^{-j\alpha_l t_i} \quad (4.28)$$

where

$$Z(\theta_k, \omega, t_i) = \sum_{q=0}^{Q-1} D_M(\omega d(\sin \theta_q - \sin \theta_k)/c) S_q(\omega, t_i) + \frac{1}{\sqrt{M}} \sum_{m=0}^{M-1} e^{j\frac{\omega}{c} m d \sin \theta_k} N_m(\omega, t_i) \quad (4.29)$$

with $S_q(\omega, t_i)$ and $N_m(\omega, t_i)$ being the STFT of q th source signal $s_q(t)$ and the m th sensor noise $n_m(t)$, respectively. The Dirichlet kernel is defined as

$$D_M(y) = \frac{1}{M} \sum_{m=0}^{M-1} e^{-jym}. \quad (4.30)$$

Assuming cycloergodicity [19], we can define the expected value of (4.28) as the asymptotic CMS,

$$P(\theta_k, \omega, \alpha_l) = \frac{1}{I} \sum_{i=0}^{I-1} \mathbb{E}\{|Z|^2\} e^{-j\alpha_l t_i} \quad (4.31)$$

where we can write

$$\mathbb{E}\{|Z|^2\} = \sum_{q=0}^{Q-1} |D_M(\omega d(\sin \theta_q - \sin \theta_k)/c)|^2 \mathbb{E}\{|S_q(\omega, t_i)|^2\} + \frac{1}{M} \sum_{m=0}^{M-1} \mathbb{E}\{|N_m(\omega, t_i)|^2\}. \quad (4.32)$$

Here, $Z = Z(\theta_k, \omega, t_i)$ and the following assumptions are made: i) the source signals and noise are uncorrelated, $\mathbb{E}\{S_q(\omega, t_i)N_m(\omega, t_i)\} = 0$, ii) the source signals are spatially uncorrelated, $\mathbb{E}\{S_{q_1}(\omega, t_i)S_{q_2}(\omega, t_i)\} = 0, q_1 \neq q_2$, iii) noise is spatially uncorrelated, $\mathbb{E}\{N_{m_1}(\omega, t_i)N_{m_2}(\omega, t_i)\} = 0, m_1 \neq m_2$.

The Fourier transform of the amplitude modulation model given in (4.15) for each source signal leads to

$$S_q(\omega, t_i) = C_q(\omega, t_i) + \frac{\mu_q}{2} C_q(\omega - \alpha_q, t_i) + \frac{\mu_q}{2} C_q(\omega + \alpha_q, t_i) \quad (4.33)$$

where $C_q(\omega, t_i)$ is the STFT of the q th broadband propeller noise $c_q(t)$. Assuming that it is a zero-mean stationary random process, we can write its STFT as

$$C_q(\omega, t_i) = \int_0^{2\pi} e^{j(u-\omega)t_i} dW_{c_q}(u) \quad (4.34)$$

using Cramér spectral representation [119]. Here, $W_{c_q}(u)$ is the orthogonal increment process with

$$\mathbb{E}\{dW_{c_q}(u)dW_{c_q}(v)^*\} = S_{c_q}(u)\delta(u-v)dudv \quad (4.35)$$

where $S_{c_q}(u)$ is the PSD of $c_q(t)$. Under the same assumptions, STFT of the sensor noise $n_m(t)$ can be written similarly as

$$N_m(\omega, t_i) = \int_0^{2\pi} e^{j(u-\omega)t_i} dW_{n_m}(u) \quad (4.36)$$

with

$$\mathbb{E}\{dW_{n_m}(u)dW_{n_m}(v)^*\} = S_{n_m}(u)\delta(u-v)dudv. \quad (4.37)$$

Using (4.33), (4.34) and (4.35),

$$\mathbb{E}\{|S_q(\omega, t_i)|^2\} = \sigma_{c_q}^2 \left(1 + \frac{\mu_q^2}{2} + \mu_q e^{-j\alpha_q t_i} + \mu_q e^{j\alpha_q t_i} + \frac{\mu_q^2}{4} e^{-j2\alpha_q t_i} + \frac{\mu_q^2}{4} e^{j2\alpha_q t_i} \right), \quad (4.38)$$

and using (4.36) and (4.37)

$$\mathbb{E}\{|N_m(\omega, t_i)|^2\} = \sigma_{n_m}^2 \quad (4.39)$$

where $\sigma_{c_q}^2$ and $\sigma_{n_m}^2$ are the variance of the broadband propeller noise of q th source signal and m th sensor noise, respectively. Finally, we can write the asymptotic CMS with the spatially uncorrelated noise, i.e., $\sigma_{n_m}^2 = \sigma_n^2$ as

$$P(\theta_k, \omega, \alpha_l) = \sum_{q=0}^{Q-1} |D_M(\omega d(\sin \theta_q - \sin \theta_k)/c)|^2 W_q(\alpha_l) + \sigma_n^2 D_I(\alpha_l RT_s) \quad (4.40)$$

where

$$W_q(\alpha_l) = \sigma_{c_q}^2 \left\{ \left(1 + \frac{\mu_q^2}{2}\right) D_I(\alpha_l RT_s) + \mu_q \left[D_I((\alpha_l - \alpha_q) RT_s) + D_I((\alpha_l + \alpha_q) RT_s) \right] + \frac{\mu_q^2}{4} \left[D_I((\alpha_l - 2\alpha_q) RT_s) + D_I((\alpha_l + 2\alpha_q) RT_s) \right] \right\}. \quad (4.41)$$

Here, notice the bias effect mentioned in Section 4.4.3 when there are multiple sources, i.e., for $Q \geq 2$, each source at θ_q weighted by the Dirichlet kernel contributes to the summation in (4.40). This causes the maxima of $P(\theta_k, \omega, \alpha_l)$ to drift away from the true DOA which in turn produces a bias increasing with the decreasing number of sensors and angle difference between DOAs. This effect becomes even more prominent in finite-sample CMS in (4.28) due to the cross-terms introduced by (4.29).

4.5.2 Averaged CMS

The bias of the CCB indicated by (4.40) cannot be eliminated but may be mitigated through spectral averaging. Notice for the scalar case that the ACMS can be written as

$$\tilde{Y}(\theta_k, \alpha_l) = \frac{1}{N} \sum_{n=0}^{N-1} \tilde{P}(\theta_k, \omega_n, \alpha_l) \quad (4.42)$$

with the asymptotic ACMS as

$$Y(\theta_k, \alpha_l) = \frac{1}{N} \sum_{n=0}^{N-1} P(\theta_k, \omega_n, \alpha_l). \quad (4.43)$$

Then, we can use the results on the asymptotic CMS with straightforward calculations giving

$$Y(\theta_k, \alpha_l) = \frac{1}{N} \sum_{n=0}^{N-1} \sum_{q=0}^{Q-1} |D_M(\omega_n d(\sin \theta_q - \sin \theta_k)/c)|^2 W_q(\alpha_l) + \sigma_n^2 D_I(\alpha_l RT_s). \quad (4.44)$$

Comparing this with (4.40), one can see that averaging over ω_n reduces the drift in maxima of $Y(\theta_k, \alpha_l)$ since the average of the magnitude Dirichlet kernels has lower

contribution for closely-spaced sources as shown in Fig. 4.3 calculated using (4.30), (A.8) and (A.10). Similarly, the finite-sample ACMS in (4.42) has the advantage of averaging where the effect of cross terms caused by (4.29) mitigates for the same reason.

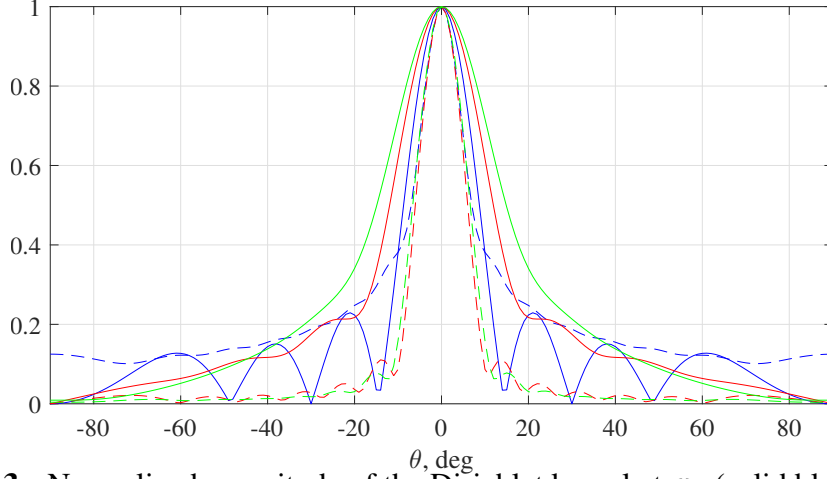


Figure 4.3 : Normalized magnitude of the Dirichlet kernel at ω_d (solid blue), its first derivative (solid red) and second derivative (solid green) have higher contributions for closely-spaced sources compared to averaging it over ω_n 's (dashed blue) with the average of its first derivatives (dashed red) and second derivatives (dashed green).

4.5.3 MSE of the CCB

Asymptotic CMS can be utilized to arrive at the asymptotic estimate $\tilde{\theta}_k$ which differs from the true DOA θ_k with the asymptotic bias $\Delta\theta_k = \tilde{\theta}_k - \theta_k$. Since the asymptotic CMS is a complex function its magnitude is used to obtain the asymptotic bias approximately by the Taylor series expansion [118,120] which then yields

$$\Delta\theta_k \approx -\frac{\frac{\partial}{\partial\theta_k}|\mathbf{P}(\theta_k, \omega, \alpha_l)|}{\frac{\partial^2}{\partial\theta_k^2}|\mathbf{P}(\theta_k, \omega, \alpha_l)|}. \quad (4.45)$$

Here, the derivatives can be found straightforwardly by evaluating the derivatives of the magnitude-squared Dirichlet kernels with respect to θ_k as shown in Appendix B.

Additionally, CMS given in (4.28) introduces a bias due to its estimation using limited number of samples. This adverse effect causes the final estimate $\hat{\theta}_k$ to deviate from the asymptotic estimate $\tilde{\theta}_k$ with $\Delta\tilde{\theta}_k = \hat{\theta}_k - \tilde{\theta}_k$ [118,120]. Thus, the total MSE reads

$$\text{MSE}(\hat{\theta}_k) = \text{E}\{(\hat{\theta}_k - \theta_k)^2\} = \text{E}\{\Delta\tilde{\theta}_k^2\} + \Delta\theta_k^2 \quad (4.46)$$

since $E\{\Delta\tilde{\theta}_k\} = 0$ as shown in Appendix C presented together with the derivation of the finite-sample variance² as

$$E\{\Delta\tilde{\theta}_k^2\} \approx \frac{E\{\text{Re}(\tilde{P}\dot{P}^*)^2\} + 2E\{\text{Re}(\tilde{P}\dot{P}^*)\text{Re}(P\dot{P}^*)\} + E\{\text{Re}(P\dot{P}^*)^2\}}{|P|^2\left(\frac{\partial^2}{\partial\theta_k^2}|P|\right)^2} \quad (4.47)$$

where $P = P(\tilde{\theta}_k, \omega, \alpha_l)$, $\dot{P} = \frac{\partial}{\partial\theta_k}P(\tilde{\theta}_k, \omega, \alpha_l)$, $\tilde{P} = \tilde{P}(\tilde{\theta}_k, \omega, \alpha_l)$ and $\dot{\tilde{P}} = \frac{\partial}{\partial\theta_k}\tilde{P}(\tilde{\theta}_k, \omega, \alpha_l)$. Then the total MSE in (4.46) can be calculated explicitly.

When we utilize the ACMS, the asymptotic bias reads

$$\Delta\theta_k \approx -\frac{\frac{\partial}{\partial\theta_k}|Y(\theta_k, \omega, \alpha_l)|}{\frac{\partial^2}{\partial\theta_k^2}|Y(\theta_k, \omega, \alpha_l)|} \quad (4.48)$$

and the finite-sample variance becomes

$$E\{\Delta\tilde{\theta}_k^2\} \approx \frac{E\{\text{Re}(\tilde{Y}\dot{Y}^*)^2\} + 2E\{\text{Re}(\tilde{Y}\dot{Y}^*)\text{Re}(Y\dot{Y}^*)\} + E\{\text{Re}(Y\dot{Y}^*)^2\}}{|Y|^2\left(\frac{\partial^2}{\partial\theta_k^2}|Y|\right)^2} \quad (4.49)$$

as shown in Appendices B and C, respectively.

4.6 Experimental Results

Consider two synthetically generated, uncorrelated and closely-spaced sources at $\theta_0 = -2^\circ$ and $\theta_1 = 2^\circ$ both with $10\log(1 + \mu^2/2)\sigma_c^2/\sigma_n^2 = 0$ dB SNR, and modulation index $\mu = 0.5$. The cyclic frequencies of the source signals are $\alpha_0 = 10.2\pi$ rad/s and $\alpha_1 = 16.2\pi$ rad/s, for the sources at θ_0 and θ_1 , respectively. Sampling frequency is $f_s = 4096$ Hz, array design frequency is $f_d = 2048$ Hz and $M = 8$. Initially, the grid is formed with 1° of spacing which is then refined using the parameters, $N_p = 10$ and $N_r = 10$. The parameters of BIHT and ABIHT algorithms are set to $K = 2$, $\varepsilon = 0.001$ and $J = 3$.

First, Fig. 4.4 shows the DOA estimates of the classical methods. We observe that all of the classical methods fail to resolve two closely-spaced sources at all frequencies. Bartlett beamformer suffers from Rayleigh resolution limit while the SNR is insufficient for Capon and MUSIC methods. CB methods, CB-BIHT and

²Detailed algebraic manipulations to calculate the finite-sample variance is presented in Appendix D.

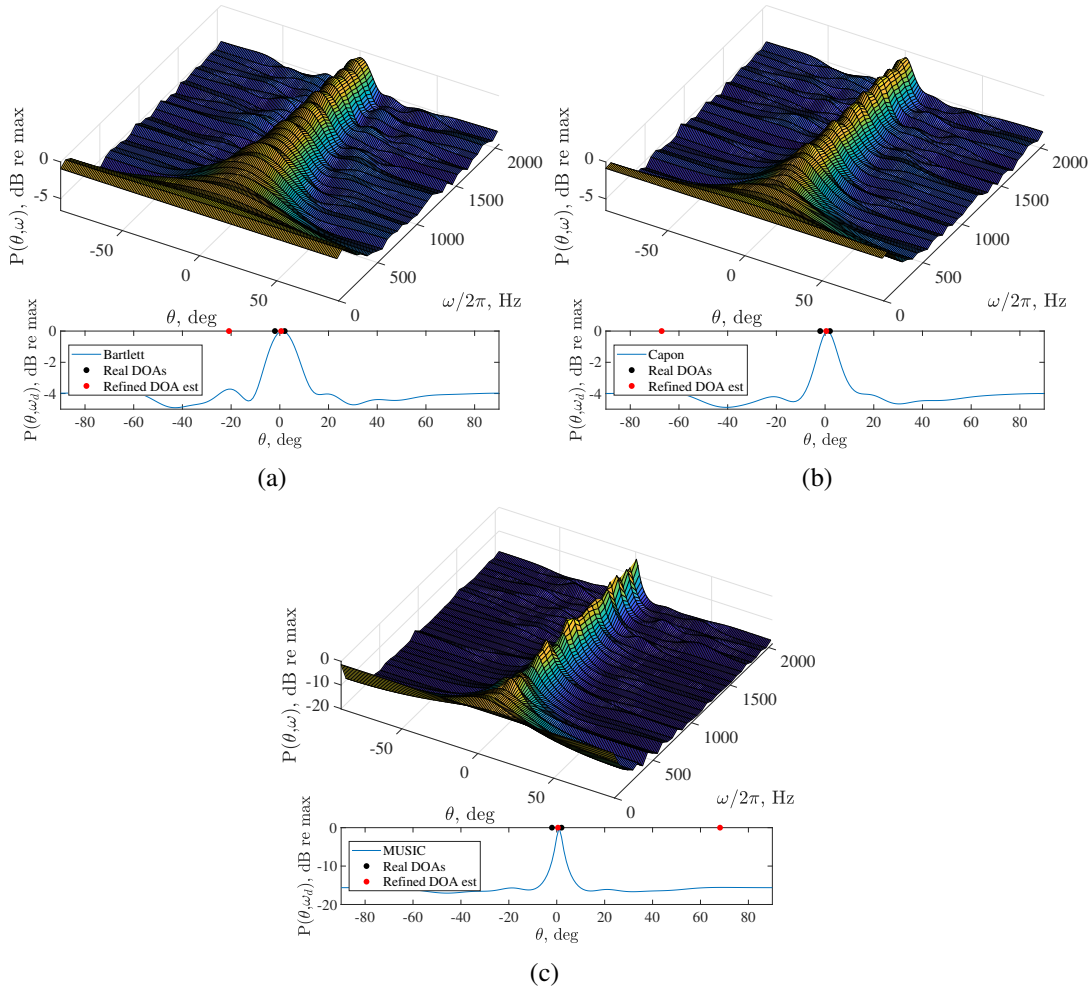


Figure 4.4 : Spatial power spectra of classical beamforming methods a) Bartlett, b) Capon and c) MUSIC under uncorrelated sources along with real DOAs and refined estimates. Two sources are at $\theta_0 = -2^\circ$ and $\theta_1 = 2^\circ$ both with 0 dB SNR, and $\mu = 0.5$.

CB-ABIHT given in Fig. 4.5(a) and Fig. 4.5(b), respectively, also fail to resolve the sources since they are based on the conventional beamformer, i.e., assuming stationary sources and limited by the Rayleigh resolution limit. CCB methods resolve the sources relying on different cyclic frequencies. However CCB-BIHT estimates (Fig. 4.5(c)) spread at lower-than-design frequencies and yield higher error at the design frequency. Utilizing the block-sparsity, CCB-ABIHT given in Fig. 4.5(d) outperforms every method as suggested.

The same experiment is run with the same parameters except the sources are highly correlated and the SNR is set to 20 dB as shown in Figs. 4.6 and 4.7. Despite the higher SNR, correlated sources cause almost singular covariance matrices yielding higher spectrum levels but unresolvable sources for classical methods. Although CB

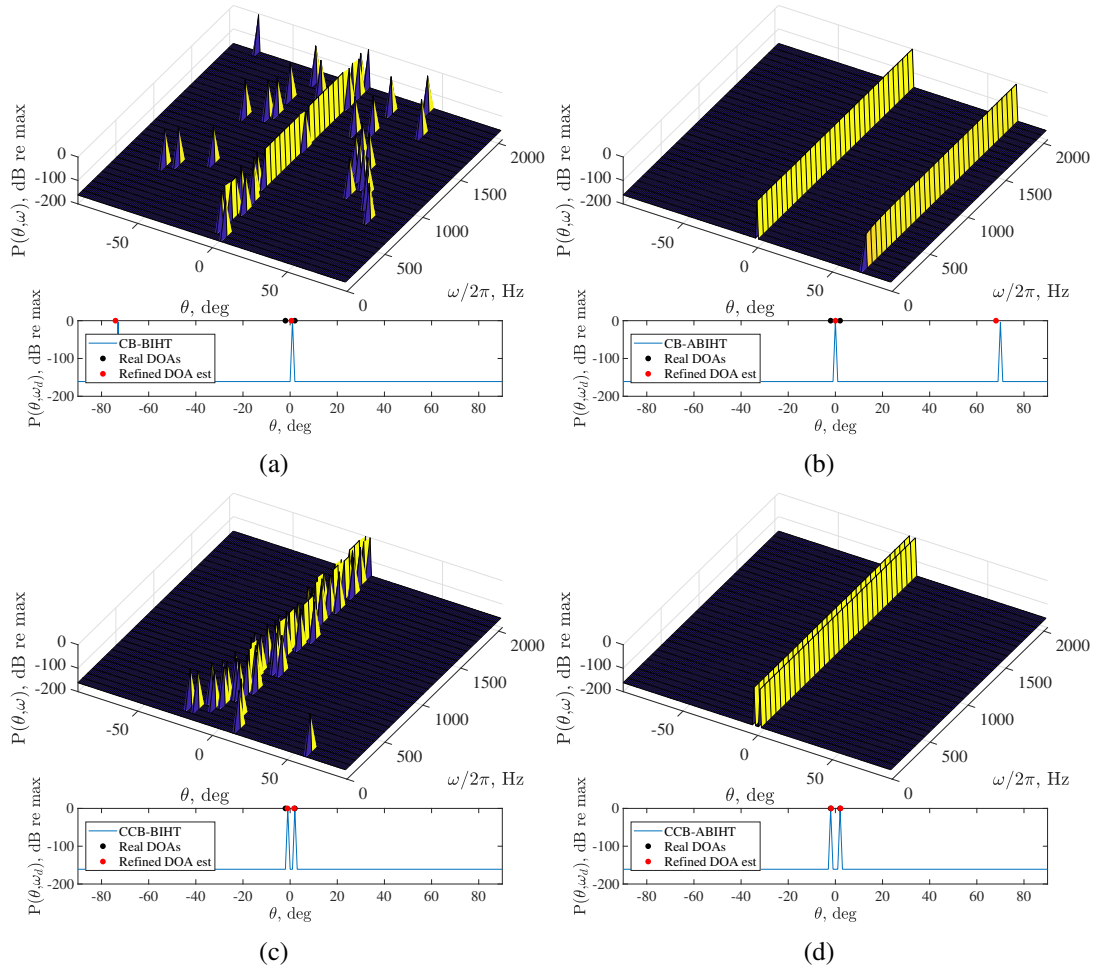


Figure 4.5 : Spatial power spectra of compressive beamforming methods under uncorrelated sources along with real DOAs and refined estimates a) CB-BIHT, b) CB-ABIHT, c) CCB-BIHT and d) CCB-ABIHT. Two sources are at $\theta_0 = -2^\circ$ and $\theta_1 = 2^\circ$ both with 0 dB SNR, and $\mu = 0.5$.

methods are immune to the correlated sources and, estimation errors become smaller with higher SNR, they are still unable to resolve two sources due to their dependence on the conventional beamformer. CCB methods seem unaffected of the correlatedness and still resolve two sources. For both uncorrelated and correlated cases, Fig. 4.1 shows spectra of all the methods at the design frequency.

Let us now present the results of the Monte Carlo simulations to compare the numerical performance of all the methods together with analytical errors derived for the CCB methods. Numerical MSE (NMSE) is calculated as

$$\text{NMSE}(\hat{\boldsymbol{\theta}}) = \frac{1}{KN_s} \sum_{n=0}^{N_s-1} \sum_{k=0}^{K-1} (\hat{\theta}_{nk} - \theta_k)^2 \quad (4.50)$$

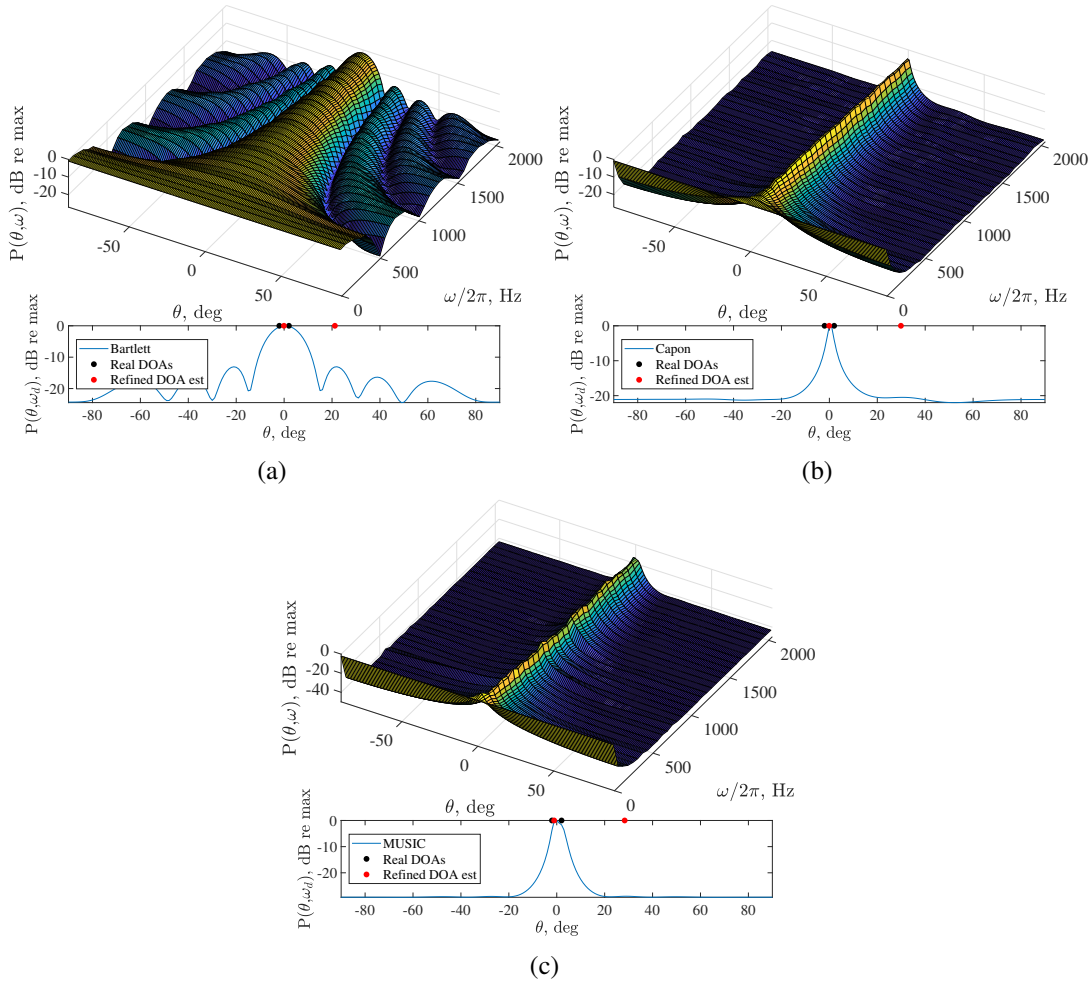


Figure 4.6 : Spatial power spectra of classical beamforming methods a) Bartlett, b) Capon and c) MUSIC under highly correlated sources along with real DOAs and refined estimates. Two sources are at $\theta_0 = -2^\circ$ and $\theta_1 = 2^\circ$ both with 20 dB SNR, and $\mu = 0.5$.

where $\hat{\boldsymbol{\theta}} = [\hat{\theta}_0 \quad \hat{\theta}_1 \quad \dots \quad \hat{\theta}_{K-1}]$ and $\hat{\theta}_{nk}$ is the DOA estimate of the k th source at n th simulation which is repeated N_s times. Analytical MSE (AMSE) given for a single source in (4.46) is used to calculate the total error by averaging over all the sources. Figs. 4.8-4.12 show MSEs of uncorrelated sources for significant signal and array parameters with $N_s = 500$. Other signal and array parameters are the same as in the previous experiments except the SNR which is set to 10 dB.

Fig. 4.8(a) shows NMSEs versus SNR from -10 to 60 dB. Bartlett and CBs have higher errors since the sources are within the Rayleigh resolution limit. However, exploiting the block-sparsity CB-ABIHT yields lower error compared to the Bartlett's method and CB-BIHT. MUSIC and Capon's method meet Cramér-Rao Bound (CRB)

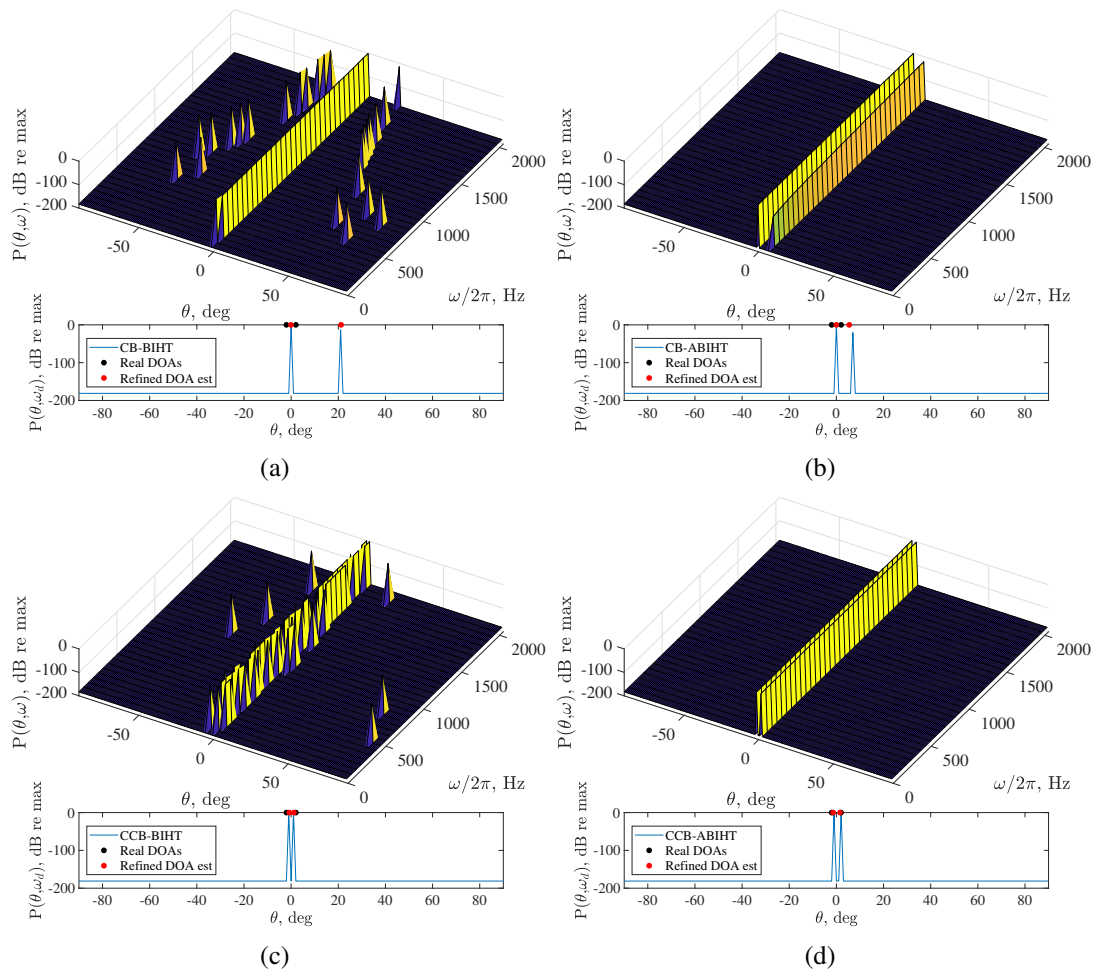


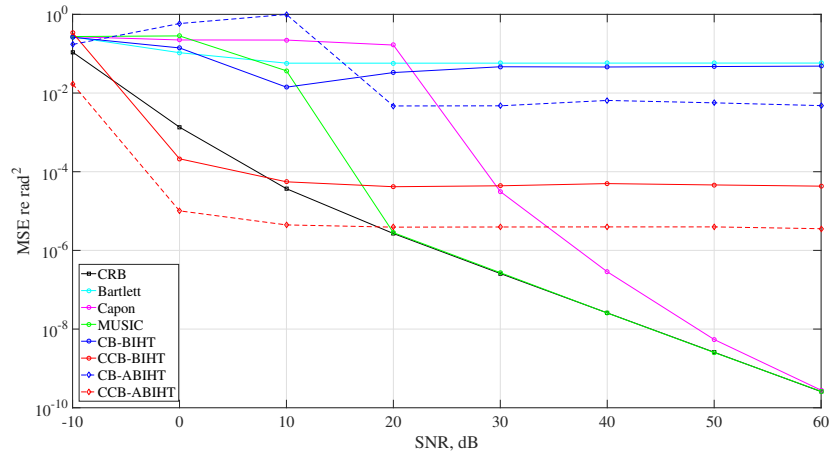
Figure 4.7 : Spatial power spectra of compressive beamforming methods under highly correlated sources along with real DOAs and refined estimates, a) CB-BIHT, b) CB-ABIHT, c) CCB-BIHT and d) CCB-ABIHT. Two sources are at $\theta_0 = -2^\circ$ and $\theta_1 = 2^\circ$ both with 20 dB SNR, and $\mu = 0.5$.

at 20 dB and 60 dB SNRs, respectively. Despite yielding lower NMSEs for lower SNRs with CCB-ABIHT producing the lowest error under 20 dB, CCB methods fail to follow the CRB. Indeed, Fig. 4.8(b) shows both asymptotic MSE (squared asymptotic bias) and finite-sample MSE (variance), thus total AMSEs, reach a plateau. This is caused by the coupling of the two sources through the spatial Dirichlet kernels as mentioned in Section 4.4.3 and observed in (4.28), (4.40), (4.42) and (4.44). Note that, while AMSE and NMSE seem to agree well for CCB-ABIHT there is a minor difference between AMSE and NMSE of CCB-BIHT. One reason might be the synthetic signal generation which, in some simulations³, does not fully meet the assumptions causing the spectral component at the design frequency to fail to act as a smooth carrier. Moreover, the above mentioned coupling effect deteriorates this situation. This is not the case for CCB-ABIHT which averages all the spectral components developing an immunity to such signals.

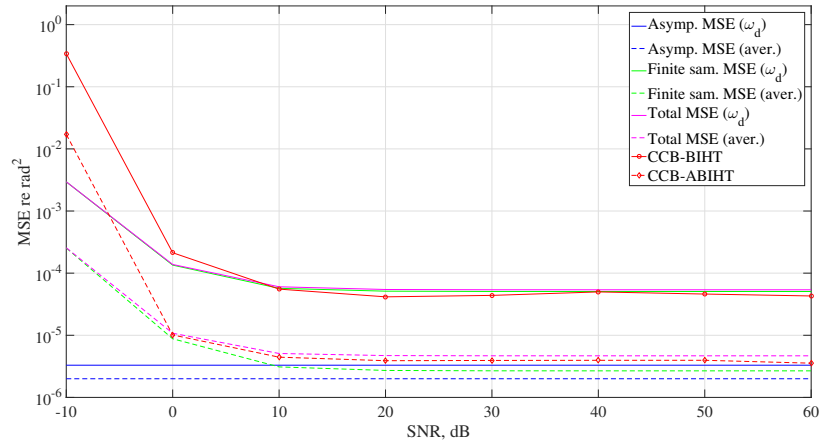
In Fig 4.9 we demonstrate the results of the effect of the modulation index since it is the source of the cyclostationarity, i.e., for $\mu = 0$ the signal in (4.15) is stationary. As expected, all the methods assuming stationary sources give the same error for different modulation indices while CCB methods produce lower errors with increasing modulation index. CCB methods outperform the methods relying on stationarity even for low modulation indices. Thus CCB can be utilized even for weakly cyclostationary signals. However there is a difference between AMSE and NMSE of CCB-BIHT especially for lower modulation indices. This might be due to the weak modulation decreasing the degree of cyclostationarity which in turn causes a mismatch between the synthetic signal and the assumptions.

An important parameter in DOA estimation is the number of sources for which the MSEs are shown in Fig 4.10. Note that, in this example each one of the K sources are 4° apart which turns out to be challenging especially for the classical methods. In some cases they fail to resolve all the K sources for which we do not compute the MSEs. Although CB-ABIHT cannot resolve multiple sources, its performance misleadingly

³Although it would be possible to neglect the outliers (a few percent of the simulations) causing the difference in MSEs, it is our preference to present the results as they are to give an insight about the CCB-BIHT method.



(a)

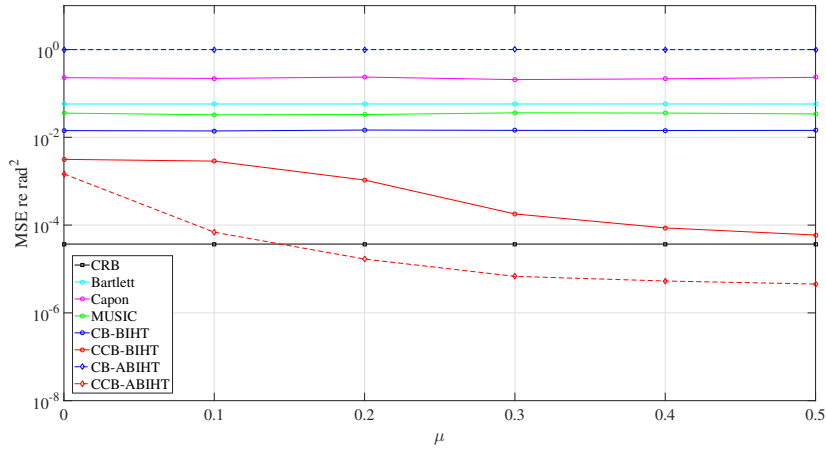


(b)

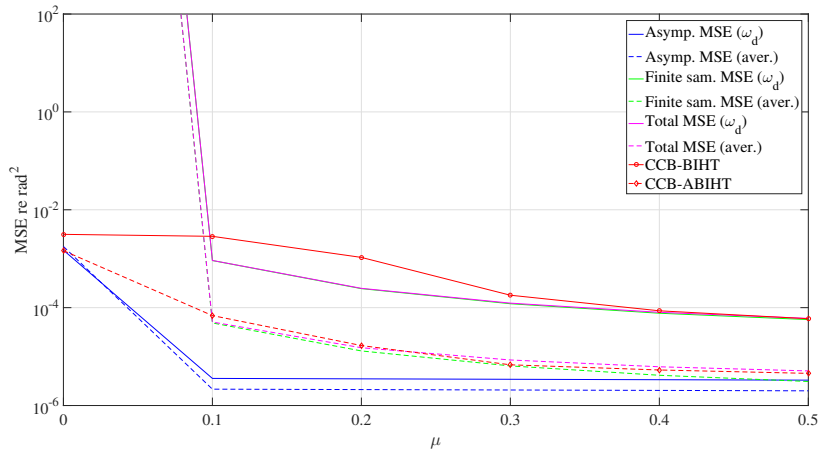
Figure 4.8 : MSE vs. SNR for two sources at $\theta_0 = -2^\circ$ and $\theta_1 = 2^\circ$ both with $\mu = 0.5$. a) NMSEs for all methods, b) AMSEs with NMSEs for CCB methods.

improves for $K = 3$ where Algorithm 6 numerically yields closer estimates to the true DOAs for odd number of sources. While CB methods generally perform better than the classical ones CCB methods succeed to resolve all the sources for all K with a slight increase in NMSE. For a single source, NMSE and AMSE for CCB methods agree well. However, with increasing K , they start to diverge which might be due to adding up of the synthetic noise generation effect. Here, it is relevant to mention that the asymptotic bias, argued so far, occurs for two or more sources as observed in Fig. 4.10(b).

Increasing the angle difference $\Delta\theta$ between DOAs has a positive effect for all the methods especially for CB and classical ones as shown in Fig. 4.11(a). Notice from Fig. 4.2 that with increasing angle difference, *Grammian* of the ULA decreases resulting better resolving capability. CCB methods perform also well for small angle



(a)



(b)

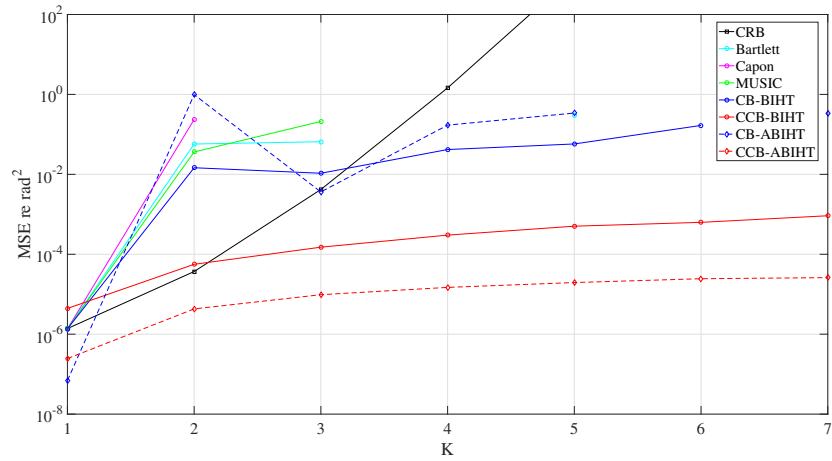
Figure 4.9 : MSE vs. modulation index for two sources at $\theta_0 = -2^\circ$ and $\theta_1 = 2^\circ$ both with 10 dB SNR. a) NMSEs for all methods, b) AMSEs with NMSEs for CCB methods. (Finite sample MSEs are too large (approx. 10^{26}) to display for $\mu = 0$ since the denominators of (4.47) and (4.49) are much smaller than their numerators, i.e., (4.41) is very small.)

differences by exploiting the cyclostationarity. AMSEs agree well with the NMSEs as displayed in Fig. 4.11(b) except $\Delta\theta = 2^\circ$ for CCB-BIHT.

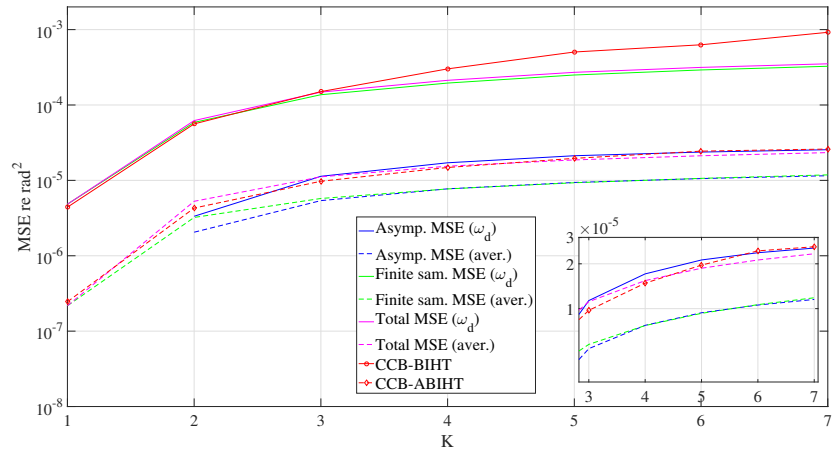
Finally, we present the performance with respect to the number of sensors M in Fig. 4.12. All the methods improve with increasing M as evidenced by the *Grammian* improvement again shown in Fig. 4.2. NMSEs agree well with the AMSEs except CCB-BIHT when $M = 32$ in Fig. 4.12(b).

4.7 Discussion

The advantages introduced by the CB methods, e.g., high resolution capability, do not apply in above numerical examples due to the reformulation of (4.11) to (4.13) in order



(a)



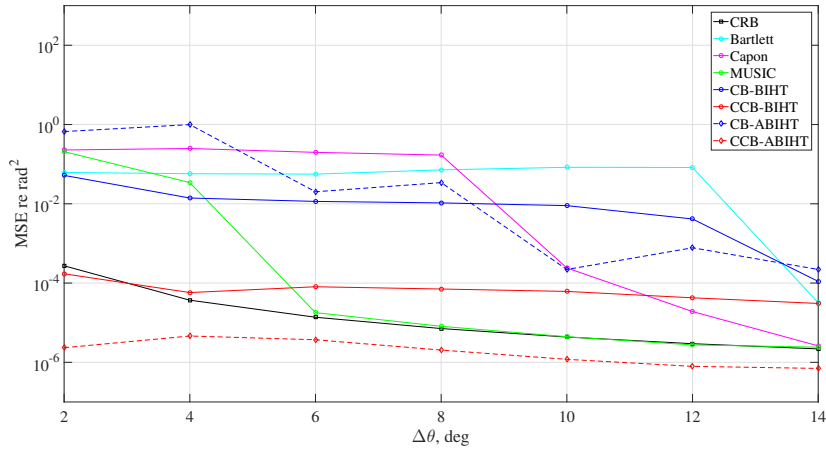
(b)

Figure 4.10 : MSE vs. number of sources for 4° -apart sources all with 10 dB SNR and $\mu = 0.5$. a) NMSEs for all methods, b) AMSEs with NMSEs for CCB methods (with a zoom to the overlapping lines for $K \geq 3$ and $\text{MSE} \leq 3 \times 10^{-5}$).

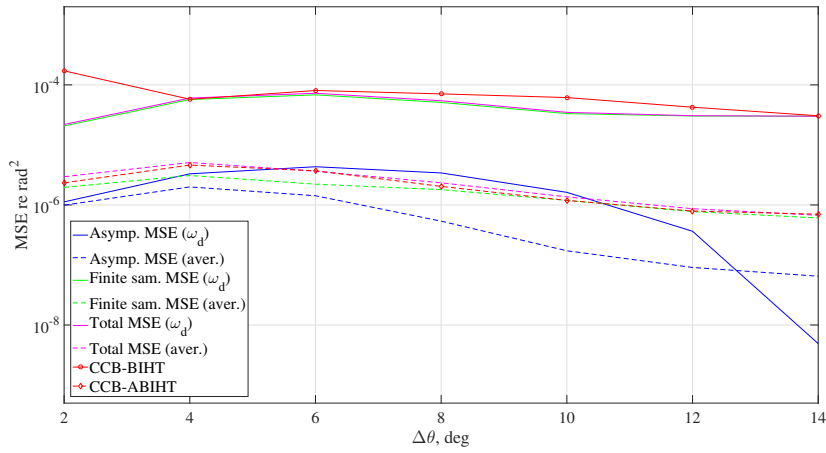
to utilize a greedy pursuit method. While a convex optimization approach could yield better recovery guarantees [32,39], we choose to leave it out of the scope of this work since our main aim is to show the significance of the CCB when the sources are of cyclostationary nature.

Spectral averaging utilized in ABIHT is not applied for classical DOA estimation methods due to their lower resolution capability at lower frequencies. Clearly, these methods perform better at the design frequency which is the very reason we exclude averaging for fair comparison with ABIHT.

Another point worth mentioning is that, in sonar signal processing source SNRs are typically low [8] which justifies the CCB approach since it outperforms other methods for low SNRs.



(a)

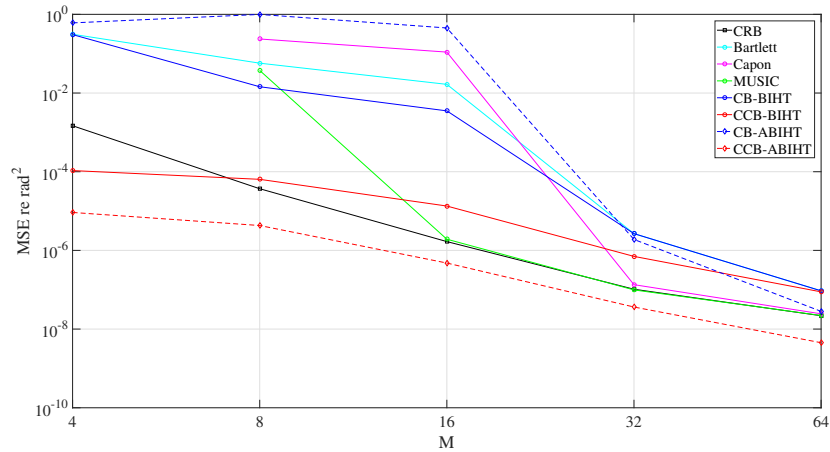


(b)

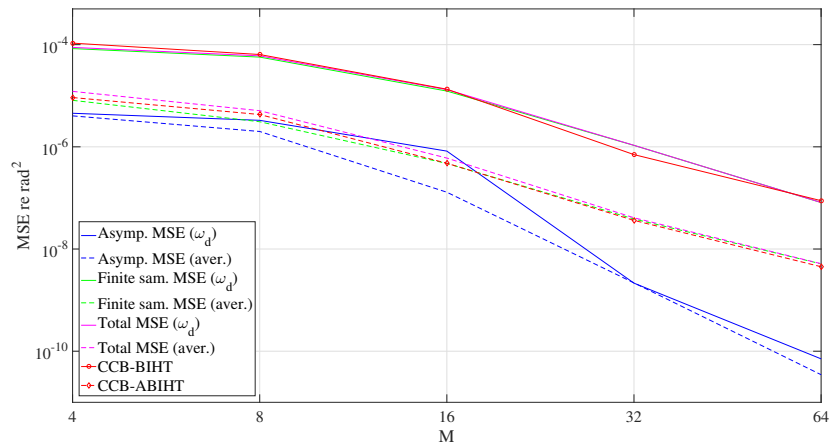
Figure 4.11 : MSE vs. angle difference between DOAs for two sources both with 10 dB SNR and $\mu = 0.5$. a) NMSEs for all methods, b) AMSEs with NMSEs for CCB methods.

CCB inherits the cyclic beamformer in (4.21) which by itself can be used as a conventional beamformer for cyclostationary sources where the Rayleigh resolution limit is overcome by exploiting the information in the cyclic frequency domain. Besides, the cyclic beamformer is a nonparametric method like its stationary counterpart, the conventional beamformer, with just the cyclostationarity assumption which could make it a desirable approach when the number of sources are unknown.

The scheme we propose can be applied to the DOA estimation of second-order cyclostationary signals of any domain such as telecommunication signals with known carrier frequencies directly used in (4.21) or unknown ones which can be determined by (4.22).



(a)



(b)

Figure 4.12 : MSE vs. number of sensors for two sources at $\theta_0 = -2^\circ$ and $\theta_1 = 2^\circ$ both with 10 dB SNR and $\mu = 0.5$. a) NMSEs for all methods, b) AMSEs with NMSEs for CCB methods.

In Chapter 2, we investigate the utilization of CS to propose an efficient sampling scheme for detecting cyclostationary propeller noise. The motivation is to compress the CMS which is then recovered to measure the detection capability. We demonstrate that detection with original and recovered samples compare well unless the sparsity and number of compressive samples are too low. Whereas, in this chapter, we exploit the sparsity of the CMS matrix both in cyclic frequency and spatial domains to localize (not detect) the cyclostationary sources. Although detection and localization are two essential and consecutive stages of sonar signal processing this work does not investigate this use case. The reason behind this limitation is that CS for detection and localization are separate problems. While detection part seeks compression of data, localization part treats the data as it is already compressed, i.e., there are

much less sensors than the number of possible source locations. Having argued that, the possibility of a compressive sonar is here to stay at least for cyclostationary sources. The first phase of this sonar can be to compress the signals acquired by each hydrophone of the array as presented in Section 2.3.3. Naturally, this compression should occur in the same time intervals in order to form the measurements to be used by CCB presented in this chapter.

5. CONCLUSIONS AND RECOMMENDATIONS

A CS and sparse recovery scheme is presented on the so-called propeller tonals to reduce the data size required for detecting ships emanating second-order cyclostationary signatures in Chapter 2. SCF of the amplitude modulated propeller noise is derived, which is sparse along its cyclic frequency dimension. A linear relationship is further derived between the Nyquist-rate and compressive CMS, which is a fast and reliable SCF approximation enabling the matrix operations required for CS. This derivation relies on the partial Fourier matrices satisfying the RIP and unitary transforms. For the sparse recovery task, CoSaMP and IHT are adapted for solving the MMV problem imposed by the CMS measurement model. ICMC is utilized to represent the joint-sparsity in this MMV setting. In practice, CMS does not reflect the theoretical sparsity of the SCF due to finite signal observations and nonstationarity of the ambient noise. However, it can still be compressible unless the modulation is weak and SNR is low, which drastically degrades the sparse recovery performance. Nevertheless, results on synthetic data as well as a real-world record from a ship of opportunity indicate that the proposed scheme yields a detection capability comparable to the Nyquist-rate processing even for lower sparsity. Future work includes seeking of quantities that further maximize the sparsity to improve the recovery and detection performance. Study of real-world data from controlled experiments and giving a theoretical bound on CMS reconstruction error will also help to assess the ultimate performance limits of the proposed scheme.

CBS of the propeller noise measurement model is derived and its theoretical sparsity is demonstrated in Chapter 3. To approximate the CBS, CMBS is proposed for which a CS scheme is developed based on the partial Fourier matrices. Preliminary results are given on estimating the Nyquist-rate ICMBC and its comparison to the ICMBCs recovered from compressive samples. Since the theoretical sparsity of CBS does not hold for real-world signals, the number of compressive samples should be high

for the near exact recovery of CMBS. However, it is still possible to acquire the prominent propeller tonals with sampling remarkably below the Nyquist rate. CMBS can be utilized not only for propeller tonals but also for general cyclostationary signals with non-Gaussian characteristics. If these signals convey information in their cyclic frequency components, which exhibit sparsity/compressibility, then it is also possible to overcome the inefficient Nyquist-rate sampling via the proposed CS scheme. Comparisons with the second-order ICMC indicates that higher-order ICMBC might yield a more prominent tonal structure since the propeller noise exhibits non-Gaussian characteristics. Future work includes the statistical analysis of the CMBS, which is needed to develop a robust detector of cyclostationarity. The compressibility analysis of CMBS is another research question to improve the sparse recovery performance.

In Chapter 4, a novel method is presented for DOA estimation of cyclostationary signals, especially originating from the propeller cavitation, encountered in sonar signal processing. The broadband model used by the DFT beamformer is adopted in the CS scheme to meet the requirement of the DOA estimation of broadband sources. A cyclic beamformer is proposed via CMS and its AMSE is derived. It is further proposed to exploit the block-sparsity of the spectral components with ACMS mitigating MSE and its derivation is shown. A well-known greedy pursuit algorithm, BIHT, is chosen due to its speed and low recovery error. It is improved with ABIHT and NMSEs obtained by both algorithms are compared where AMSEs are derived for both CMS and ACMS. Numerical examples are given for uncorrelated and correlated closely-spaced sources. Further results of numerical examples are presented, where each method is compared in terms of SNR, modulation index, number of sources, angle difference between DOAs and number of sensors. CCB, depending on the conventional beamformer, introduces an asymptotic bias for multiple DOA estimation and a variance due to limited number of observations which are revealed by the analytical derivations. Nevertheless, it has many desirable properties such as high resolution capability, being immune to correlated sources, overachieving CRB for low SNRs and high number of sources. All these make CCB eligible for cyclostationary sources compared to the methods that require stationarity assumption. Future work includes further investigation of CCB for several signal parameters such as multiple

propeller tonals and under different array settings like circular or random arrays. Applying CCB to real-world underwater sound data would be another future direction where the signals are more complex due to the physical challenges.

This thesis investigates an efficient sampling scheme to detect and localize water crafts with cyclostationary signatures. Although detection and localization are two essential and consecutive stages of sonar signal processing this thesis does not consider this use case. The reason behind this limitation is that compressive sensing for detection and localization are separate problems. While detection part seeks compression of data, localization part treats the data as it is already compressed. Having argued that, the possibility of a *compressive sonar* is here to stay at least for cyclostationary sources. The first phase of compressive sonar can be to compress the signals acquired by each sensor of the array as presented in Chapter 2. Naturally, the compression should occur in the same time intervals in order to form the source matrix to be used by CCB presented in Chapter 4.

This work also demonstrates the possible use cases of the proposed methods in compressive sensing of general cyclostationary signals. For instance, compressive CMS can be used to compress analog/digital communication signals, radar signals, time-frequency distributions and vibration signals exhibiting cyclostationarity. Then, the proposed sparse recovery methods reconstruct the Nyquist-rate CMS from which ICMC is calculated for automatic detection purposes. Should these signals be of non-Gaussian nature ICMBC serves a similar goal, except the open research question of its variance required to build an automatic detector. DOA estimation is another research topic for this type of signals, where CCB would be useful to overcome Rayleigh resolution limit. Besides, CCB accepts cyclic frequencies both known and unknown depending on the application.

REFERENCES

- [1] **Urlick, R.J.** (1983). *Principles of underwater sound 3rd edition*, Peninsula Publishing.
- [2] **Richardson, W.J., Greene Jr, C.R., Malme, C.I. and Thomson, D.H.** (2013). *Marine mammals and noise*, Academic Press.
- [3] **Firat, U., Akgül, T. and Dede, A.** (2018). *Ambient, ship-radiated and biologic noise in bosporus and gokceada*, unpublished abstract and presentation in 1st National Bioacoustics Workshop, Gökçeada, Çanakkale, Turkey.
- [4] **Seol, H., Jung, B., Suh, J.C. and Lee, S.** (2002). Prediction of non-cavitating underwater propeller noise, *Journal of Sound and Vibration*, 257(1), 131–156.
- [5] **Rayleigh, L.** (1917). VIII. On the pressure developed in a liquid during the collapse of a spherical cavity, *The London, Edinburgh, and Dublin Philosophical Magazine and Journal of Science*, 34(200), 94–98.
- [6] **Harrison, M.** (1952). An experimental study of single bubble cavitation noise, *The Journal of the Acoustical Society of America*, 24(6), 776–782.
- [7] **Ross, D.** (1976). *Mechanics of underwater noise*, Pergamon Press, New York, NY.
- [8] **Nielsen, R.O.** (1999). Cramer-Rao lower bounds for sonar broad-band modulation parameters, *IEEE Journal of Oceanic Engineering*, 24(3), 285–290.
- [9] **McKenna, M.F., Ross, D., Wiggins, S.M. and Hildebrand, J.A.** (2012). Underwater radiated noise from modern commercial ships, *The Journal of the Acoustical Society of America*, 131(1), 92–103.
- [10] **Wittekind, D. and Schuster, M.** (2016). Propeller cavitation noise and background noise in the sea, *Ocean Engineering*, 120, 116–121.
- [11] **d'Assumpcao, H.** (1970). Theoretical assessment of DEMON performance, **Technical Report**, Weapons Research Establishment.
- [12] **Kummert, A.** (1993). Fuzzy technology implemented in sonar systems, *IEEE Journal of Oceanic Engineering*, 18(4), 483–490.
- [13] **Kirsteins, I., Clark, P. and Atlas, L.** (2011). Maximum-likelihood estimation of propeller noise modulation characteristics, *Proc. 4th International Conference and Exhibition on Underwater Acoustic Measurements: Technologies & Results*, pp.355–362.

- [14] **Firat, U. and Akgül, T.** (2017). Ship acoustic signature analysis (in turkish), *EMO Bilimsel Dergi*, 7(13), 25–31.
- [15] **Bennett, W.** (1958). Statistics of regenerative digital transmission, *Bell System Technical Journal*, 37(6), 1501–1542.
- [16] **Gardner, W. and Franks, L.** (1975). Characterization of cyclostationary random signal processes, *IEEE Transactions on Information Theory*, 21(1), 4–14.
- [17] **Gardner, W.A.** (1994). Cyclostationarity in communications and signal processing, **Technical Report**, Statistical Signal Processing Inc., Yountville, CA.
- [18] **Antoni, J.** (2009). Cyclostationarity by examples, *Mechanical Systems and Signal Processing*, 23(4), 987–1036.
- [19] **Antoni, J. and Hanson, D.** (2012). Detection of surface ships from interception of cyclostationary signature with the cyclic modulation coherence, *IEEE Journal of Oceanic Engineering*, 37(3), 478–493.
- [20] **Gardner, W.** (1990). Spectral characterization of N-th order cyclostationarity, *Fifth ASSP Workshop on Spectrum Estimation and Modeling*, IEEE, pp.251–255.
- [21] **Hinich, M.J., Marandino, D. and Sullivan, E.J.** (1989). Bispectrum of ship-radiated noise, *The Journal of the Acoustical Society of America*, 85(4), 1512–1517.
- [22] **Machell, F.W., Penrod, C.S. and Ellis, G.E.,** (1989). Statistical characteristics of ocean acoustic noise processes, *Topics in Non-Gaussian Signal Processing*, Springer, pp.29–57.
- [23] **Donoho, D.L.** (2006). Compressed sensing, *IEEE Transactions on Information Theory*, 52(4), 1289–1306.
- [24] **Candès, E.J.** (2006). Compressive sampling, *Proceedings of the International Congress of Mathematicians*, volume 3, pp.1433–1452.
- [25] **Candès, E.J., Romberg, J. and Tao, T.** (2006). Robust uncertainty principles: Exact signal reconstruction from highly incomplete frequency information, *IEEE Transactions on Information Theory*, 52(2), 489–509.
- [26] **Candès, E.J. and Tao, T.** (2006). Near-optimal signal recovery from random projections: Universal encoding strategies?, *IEEE Transactions on Information Theory*, 52(12), 5406–5425.
- [27] **Candes, E. and Romberg, J.** (2007). Sparsity and incoherence in compressive sampling, *Inverse Problems*, 23(3), 969.
- [28] **Shannon, C.E.** (1949). Communication in the presence of noise, *Proceedings of the IRE*, 37(1), 10–21.

- [29] **Davenport, M.A., Duarte, M.F., Eldar, Y.C. and Kutyniok, G.**, (2012). Introduction to compressed sensing, **Y.C. Eldar and G. Kutyniok**, editors, *Compressed Sensing: Theory and Applications*, chapter 1, Cambridge University Press, Cambridge, UK, pp.1–64.
- [30] **Candès, E.J. and Wakin, M.B.** (2008). An introduction to compressive sampling, *IEEE Signal Processing Magazine*, 25(2), 21–30.
- [31] **Tropp, J. and Wright, S.J.** (2010). Computational methods for sparse solution of linear inverse problems, *Proceedings of the IEEE*, 98(6), 948–958.
- [32] **Malioutov, D., Çetin, M. and Willsky, A.S.** (2005). A sparse signal reconstruction perspective for source localization with sensor arrays, *IEEE Transactions on Signal Processing*, 53(8), 3010–3022.
- [33] **Gürbüz, A.C., McClellan, J.H. and Cevher, V.** (2008). A compressive beamforming method, *IEEE International Conference on Acoustics, Speech and Signal Processing (ICASSP 2008)*, pp.2617–2620.
- [34] **Edelmann, G.F. and Gaumont, C.F.** (2011). Beamforming using compressive sensing, *The Journal of the Acoustical Society of America*, 130(4), EL232–EL237.
- [35] **Tang, Z., Blacchiere, G. and Leus, G.** (2011). Aliasing-free wideband beamforming using sparse signal representation, *IEEE Transactions on Signal Processing*, 59(7), 3464–3469.
- [36] **Boufounos, P.T., Smaragdis, P. and Raj, B.** (2011). Joint sparsity models for wideband array processing, *Wavelets and Sparsity XIV*, volume 8138, International Society for Optics and Photonics, pp.124–133.
- [37] **Gretsistas, A.** (2013). *Sparse representations & compressed sensing with application to the problem of direction-of-arrival estimation.*, Queen Mary University of London.
- [38] **Li, X., Ma, X., Yan, S. and Hou, C.** (2013). Single snapshot DOA estimation by compressive sampling, *Applied Acoustics*, 74(7), 926–930.
- [39] **Xenaki, A., Gerstoft, P. and Mosegaard, K.** (2014). Compressive beamforming, *The Journal of the Acoustical Society of America*, 136(1), 260–271.
- [40] **Fortunati, S., Grasso, R., Gini, F., Greco, M.S. and LePage, K.** (2014). Single-snapshot DOA estimation by using compressed sensing, *EURASIP Journal on Advances in Signal Processing*, 2014(1), 1–17.
- [41] **Wiese, T., Weiland, L. and Utschick, W.** (2015). DOA estimation and array registration with joint sparse reconstruction methods, *2015 IEEE 16th International Workshop on Signal Processing Advances in Wireless Communications (SPAWC)*, IEEE, pp.500–504.

- [42] **Gerstoff, P., Xenaki, A. and Mecklenbräuker, C.F.** (2015). Multiple and single snapshot compressive beamforming, *The Journal of the Acoustical Society of America*, 138(4), 2003–2014.
- [43] **Xenaki, A. and Gerstoff, P.** (2015). Grid-free compressive beamforming, *The Journal of the Acoustical Society of America*, 137(4), 1923–1935.
- [44] **Xenaki, A., Gerstoff, P. and Fernandez-Grande, E.** (2015). Sparse DOA estimation with polynomial rooting, *2015 3rd International Workshop on Compressed Sensing Theory and its Applications to Radar, Sonar and Remote Sensing (CoSeRa)*, IEEE, pp.104–108.
- [45] **Zhao, W., Li, G., Zheng, C. and Ge, F.** (2016). Capon cepstrum weighted l_{2,1} minimization for wideband DOA estimation with sonar arrays, *OCEANS 2016-Shanghai*, IEEE, pp.1–4.
- [46] **Park, Y., Choo, Y. and Seong, W.** (2018). Multiple snapshot grid free compressive beamforming, *The Journal of the Acoustical Society of America*, 143(6), 3849–3859.
- [47] **Raj, A.G. and McClellan, J.H.** (2018). Single snapshot super-resolution DOA estimation for arbitrary array geometries, *IEEE Signal Processing Letters*, 26(1), 119–123.
- [48] **Park, Y., Seong, W. and Gerstoff, P.** (2020). Block-sparse two-dimensional off-grid beamforming with arbitrary planar array geometry, *The Journal of the Acoustical Society of America*, 147(4), 2184–2191.
- [49] **Yang, Y., Du, Z., Wang, Y., Guo, X., Yang, L. and Zhou, J.** (2021). Convex compressive beamforming with nonconvex sparse regularization, *The Journal of the Acoustical Society of America*, 149(2), 1125–1137.
- [50] **Nielsen, R.O.** (1991). *Sonar signal processing*, Artech House, Inc.
- [51] **Hodges, R.P.** (2011). *Underwater acoustics: Analysis, design and performance of sonar*, John Wiley & Sons.
- [52] **Firat, U. and Akgül, T.** (2017). Compressive sensing for detecting ships with second-order cyclostationary signatures, *IEEE Journal of Oceanic Engineering*, 43(4), 1086–1098.
- [53] **Firat, U. and Akgül, T.** (2023). Compressive sensing of cyclic bispectrum (submitted to IEEE Journal of Oceanic Engineering, February 2023).
- [54] **Firat, U. and Akgül, T.** (2024). Compressive beamforming for direction-of-arrival estimation of cyclostationary propeller noise, *Signal Processing*, 214, 109221.
- [55] **Amindavar, H. and Moghaddam, P.P.** (2000). Estimation of propeller shaft rate and vessel classification in multipath environment, *Proceedings in IEEE Sensor Array and Multichannel Signal Processing Workshop*, pp.125–128.

- [56] **Kudryavtsev, A., Luginets, K. and Mashoshin, A.** (2003). Amplitude modulation of underwater noise produced by seagoing vessels, *Acoustical Physics*, 49(2), 184–188.
- [57] **Bao, F., Wang, X., Tao, Z., Wang, Q. and Du, S.** (2009). Adaptive extraction of modulation for cavitation noise, *The Journal of the Acoustical Society of America*, 126(6), 3106–3113.
- [58] **Bao, F., Wang, X., Tao, Z., Wang, Q. and Du, S.** (2010). EMD-based extraction of modulated cavitation noise, *Mechanical Systems and Signal Processing*, 24(7), 2124–2136.
- [59] **Clark, P., Kirsteins, I. and Atlas, L.** (2010). Multiband analysis for colored amplitude-modulated ship noise, *IEEE International Conference on Acoustics Speech and Signal Processing (ICASSP 2010) Proc.*, pp.3970–3973.
- [60] **Firat, U. and Akgül, T.** (2013). Spectral estimation of cavitation related narrow-band ship radiated noise based on fractional lower order statistics and multiple signal classification, *Proceedings of MTS/IEEE OCEANS 2013 San Diego*, pp.960–965.
- [61] **Gardner, W.A.** (1986). The spectral correlation theory of cyclostationary time-series, *Signal Processing*, 11(1), 13–36.
- [62] **Blumensath, T. and Davies, M.E.** (2009). Iterative hard thresholding for compressed sensing, *Applied and Computational Harmonic Analysis*, 27(3), 265–274.
- [63] **Needell, D. and Tropp, J.A.** (2009). CoSaMP: Iterative signal recovery from incomplete and inaccurate samples, *Applied and Computational Harmonic Analysis*, 26(3), 301–321.
- [64] **Dandawate, A.V. and Giannakis, G.B.** (1994). Nonparametric polyspectral estimators for kth-order (almost) cyclostationary processes, *IEEE Transactions on Information Theory*, 40(1), 67–84.
- [65] **Tian, Z., Tafesse, Y. and Sadler, B.M.** (2012). Cyclic feature detection with sub-Nyquist sampling for wideband spectrum sensing, *IEEE Journal of Selected Topics in Signal Processing*, 6(1), 58–69.
- [66] **Lim, C.W. and Wakin, M.B.** (2015). Compressive temporal higher order cyclostationary statistics, *IEEE Transactions on Signal Processing*, 63(11), 2942–2956.
- [67] **Romero, D., Ariananda, D.D., Tian, Z. and Leus, G.** (2016). Compressive covariance sensing: Structure-based compressive sensing beyond sparsity, *IEEE Signal Processing Magazine*, 33(1), 78–93.

- [68] **Flandrin, P. and Borgnat, P.** (2010). Time-frequency energy distributions meet compressed sensing, *IEEE Transactions on Signal Processing*, 58(6), 2974–2982.
- [69] **Jung, A., Taubock, G. and Hlawatsch, F.** (2013). Compressive spectral estimation for nonstationary random processes, *IEEE Transactions on Information Theory*, 59(5), 3117–3138.
- [70] **Sun, X., Zhou, Z., Zhao, C. and Zou, W.** (2012). A compressed sensing radar detection scheme for closing vehicle detection, *2012 IEEE International Conference on Communications (ICC)*, IEEE, pp.6371–6375.
- [71] **Napolitano, A.** (2016). Cyclostationarity: New trends and applications, *Signal processing*, 120, 385–408.
- [72] **Gardner, W.A.** (1991). Exploitation of spectral redundancy in cyclostationary signals, *IEEE Signal Processing Magazine*, 8(2), 14–36.
- [73] **Lourens, J.G. and Coetzer, M.W.** (1987). Detection of mechanical ship features from underwater acoustic sound, *IEEE International Conference on Acoustics, Speech, and Signal Processing (ICASSP'87)*, volume 12, pp.1700–1703.
- [74] **Lourens, J.G.**, (1989). Classification of ships using underwater radiated noise, **Y.T. Chan**, editor, *Underwater Acoustic Data Processing*, volume 161, Springer Netherlands, 1 edition, pp.591–596.
- [75] **Li, S. and Yang, D.** (2007). DEMON feature extraction of acoustic vector signal based on 3/2-D spectrum, *2nd IEEE Conference on Industrial Electronics and Applications (ICIEA 2007) Proc.*, pp.2239–2243.
- [76] **Shi, G.z. and Hu, J.c.** (2007). Ship noise demodulation line spectrum fusion feature extraction based on the wavelet packet, *Proceedings of the International Conference on Wavelet Analysis and Pattern Recognition (ICWAPR'07)*, volume 2, pp.846–850.
- [77] **Baraniuk, R.G.** (2007). Compressive sensing, *IEEE Signal Processing Magazine*, 24(4).
- [78] **Foucart, S. and Rauhut, H.**, (2013). An invitation to compressive sensing, *A Mathematical Introduction to Compressive Sensing*, chapter 1, Springer, Basel, Switzerland, pp.1–39.
- [79] **Elad, M.**, (2010). Prologue, *Sparse and Redundant Representations - From Theory to Applications in Signal and Image Processing*, chapter 1, Springer, New York, NY, pp.3–15.
- [80] **Duarte, M.F. and Baraniuk, R.G.** (2013). Spectral compressive sensing, *Applied and Computational Harmonic Analysis*, 35(1), 111–129.

- [81] **Chung, K.W., Sutin, A., Sedunov, A. and Bruno, M.** (2011). DEMON acoustic ship signature measurements in an urban harbor, *Advances in Acoustics and Vibration, 2011*.
- [82] **Lourens, J.G. and du Preez, J.** (1998). Passive sonar ML estimator for ship propeller speed, *IEEE Journal of Oceanic Engineering, 23*(4), 448–453.
- [83] **Urlick, R.J.** (1984). Ambient noise in the sea, **Technical Report**, Undersea Warfare Technology Office, Naval Sea Systems Command, Dept. of the Navy.
- [84] **Bouvet, M. and Schwartz, S.C.** (1988). Underwater noises: Statistical modeling, detection, and normalization, *The Journal of the Acoustical Society of America, 83*(3), 1023–1033.
- [85] **Ulug, U., Akgul, T. and Gezer, C.** (2008). Ambient noise measurements in the strait of Istanbul, *Proceedings of the Institute of Acoustics, Conference on Underwater Noise Measurement, Impact and Mitigation*, pp.35–42.
- [86] **Baraniuk, R., Davenport, M., DeVore, R. and Wakin, M.** (2008). A simple proof of the restricted isometry property for random matrices, *Constructive Approximation, 28*(3), 253–263.
- [87] **Rudelson, M. and Vershynin, R.** (2008). On sparse reconstruction from Fourier and Gaussian measurements, *Communications on Pure and Applied Mathematics, 61*(8), 1025–1045.
- [88] **Haviv, I. and Regev, O.** (2016). The restricted isometry property of subsampled Fourier matrices, *Proceedings of the Twenty-Seventh Annual ACM-SIAM Symposium on Discrete Algorithms*, pp.288–297.
- [89] **Cotter, S.F., Rao, B.D., Engan, K. and Kreutz-Delgado, K.** (2005). Sparse solutions to linear inverse problems with multiple measurement vectors, *IEEE Transactions on Signal Processing, 53*(7), 2477–2488.
- [90] **Blanchard, J.D., Cermak, M., Hanle, D. and Jing, Y.** (2014). Greedy algorithms for joint sparse recovery, *IEEE Transactions on Signal Processing, 62*(7), 1694–1704.
- [91] **Byun, S.H., Kim, S.M., Park, C., Kim, K. and Lee, C.M.** (2016). Cyclostationary analysis of underwater noise for vehicle propeller monitoring, *OCEANS 2016 MTS/IEEE Monterey*, IEEE, pp.1–4.
- [92] **Machell, F.W. and Penrod, C.S.** (1985). Energy detection in the ocean acoustic environment, *The Journal of the Acoustical Society of America, 77*(S1), S70–S70.
- [93] **Frazer, G.J. and Boashash, B.** (1991). Detection of underwater transient acoustic signals using time-frequency distributions and higher-order spectra, *Conference Record of the Twenty-Fifth Asilomar Conference on Signals, Systems and Computers.*, IEEE, pp.1103–1107.

- [94] **Boashash, B. and Frazer, G.** (1992). Time-varying higher-order spectra, generalised Wigner-Ville distribution and the analysis of underwater acoustic data, *IEEE International Conference on Acoustics, Speech, and Signal Processing*, volume 5, IEEE, pp.193–196.
- [95] **Ioup, G.E., Iopu, J.W. et al.** (1998). The effects of ambient shipping noise on the performance of single and multiple channel moment detectors for unknown transient signals, **Technical Report**, Naval Research Lab Stennis Space Center MS Shallow Water Coastal Acoustics Section.
- [96] **Dwyer, R.F.** (1983). A technique for improving detection and estimation of signals contaminated by under ice noise, *The Journal of the Acoustical Society of America*, 74(1), 124–130.
- [97] **Dwyer, R.** (1983). Detection of non-Gaussian signals by frequency domain kurtosis estimation, *IEEE International Conference on Acoustics, Speech, and Signal Processing.*, volume 8, IEEE, pp.607–610.
- [98] **Dwyer, R.** (1984). Use of the kurtosis statistic in the frequency domain as an aid in detecting random signals, *IEEE Journal of Oceanic Engineering*, 9(2), 85–92.
- [99] **Brockett, P.L., Hinich, M. and Wilson, G.R.** (1989). Bispectral characterization of ocean acoustic time series: nonlinearity and non-Gaussianity, *Topics in Non-Gaussian Signal Processing*, 2–16.
- [100] **Bouvet, M. and Schwartz, S.C.** (1989). Comparison of adaptive and robust receivers for signal detection in ambient underwater noise, *IEEE Transactions on Acoustics, Speech, and Signal Processing*, 37(5), 621–626.
- [101] **Regazzoni, C.S., Tesei, A. and Tacconi, G.** (1994). A comparison between spectral and bispectral analysis for ship detection from acoustical time series, *IEEE International Conference on Acoustics, Speech, and Signal Processing.*, volume 2, IEEE, pp.II–289.
- [102] **Richardson, A. and Hodgkiss, W.** (1994). Bispectral analysis of underwater acoustic data, *The Journal of the Acoustical Society of America*, 96(2), 828–837.
- [103] **Lennartsson, R.K., Robinson, J.W.C., Persson, L., Hinich, M.J. and McLaughlin, S.** (2000). Passive sonar signature estimation using bispectral techniques, *Proceedings of the Tenth IEEE Workshop on Statistical Signal and Array Processing (Cat. No.00TH8496)*, pp.281–285.
- [104] **Nikias, C.L. and Raghuvver, M.R.** (1987). Bispectrum estimation: A digital signal processing framework, *Proceedings of the IEEE*, 75(7), 869–891.

- [105] **Dandawate, A.V. and Giannakis, G.B.** (1992). Detection and classification of cyclostationary signals via cyclic-HOS: A unified approach, *Advanced Signal Processing Algorithms, Architectures, and Implementations III*, volume 1770, SPIE, pp.315–326.
- [106] **Van Trees, H.L.** (2002). *Optimum array processing, Part IV of Detection, Estimation, and Modulation Theory*, John Wiley & Sons, Inc., New York.
- [107] **Bartlett, M.S.** (1948). Smoothing periodograms from time series with continuous spectra, *Nature*, 161(4096), 686–687.
- [108] **Capon, J.** (1969). High-resolution frequency-wavenumber spectrum analysis, *Proceedings of the IEEE*, 57(8), 1408–1418.
- [109] **Schmidt, R.** (1986). Multiple emitter location and signal parameter estimation, *IEEE Transactions on Antennas and Propagation*, 34(3), 276–280.
- [110] **Yang, Y., Chu, Z. and Ping, G.** (2019). Two-dimensional multiple-snapshot grid-free compressive beamforming, *Mechanical Systems and Signal Processing*, 124, 524–540.
- [111] **Ang, Y.Y., Nguyen, N. and Gan, W.S.** (2020). Multiband grid-free compressive beamforming, *Mechanical Systems and Signal Processing*, 135, 106425.
- [112] **Schell, S.V., Calabretta, R.A., Gardner, W.A. and Agee, B.G.** (1989). Cyclic MUSIC algorithms for signal-selective direction estimation, *International Conference on Acoustics, Speech, and Signal Processing*, IEEE, pp.2278–2281.
- [113] **Stoica, P. and Moses, R.** (2005). *Spectral analysis of signals*, Prentice Hall, New Jersey.
- [114] **Pisarenko, V.F.** (1973). The retrieval of harmonics from a covariance function, *International Geophysical Journal*, 33(3), 347–366.
- [115] **Pillai, S.U.** (1989). *Array signal processing*, Springer Science & Business Media.
- [116] **Stoeckle, C., Munir, J., Mezghani, A. and Nossek, J.A.** (2015). Doa estimation performance and computational complexity of subspace-and compressed sensing-based methods, *WSA 2015; 19th International ITG Workshop on Smart Antennas*, VDE, pp.1–6.
- [117] **Gentilho Jr, E., Scalassara, P.R. and Abrão, T.** (2020). Direction-of-arrival estimation methods: A performance-complexity tradeoff perspective, *Journal of Signal Processing Systems*, 92(2), 239–256.
- [118] **Hawkes, M. and Nehorai, A.** (1998). Acoustic vector-sensor beamforming and Capon direction estimation, *IEEE Transactions on Signal Processing*, 46(9), 2291–2304.
- [119] **Cramér, H.** (1992). On harmonic analysis in certain functional spaces, *Breakthroughs in Statistics*, Springer, pp.179–184.

- [120] **Vaidyanathan, C. and Buckley, K.M.** (1995). Performance analysis of the MVDR spatial spectrum estimator, *IEEE Transactions on Signal Processing*, 43(6), 1427–1437.
- [121] **Brillinger, D.R.** (2001). *Time series: data analysis and theory*, SIAM.
- [122] **Isserlis, L.** (1918). On a formula for the product-moment coefficient of any order of a normal frequency distribution in any number of variables, *Biometrika*, 12(1/2), 134–139.

APPENDICES

APPENDIX A: SCF of the Propeller Noise

APPENDIX B: Asymptotic Bias of the CCB

APPENDIX C: Finite-Sample Bias and Variance of the CCB

APPENDIX D: Algebraic Manipulations for Finite-Sample Variance of the CCB

APPENDIX A: SCF of the Propeller Noise

Modeling the propeller noise as in (2.1) with the assumptions given in Section 2.2.2 we can write the autocorrelation function of the real-valued $x(t)$ as

$$\begin{aligned}
R_x(t, s) &\triangleq \mathbb{E}\{x(t)x(s)\} \\
&= \mathbb{E}\{[c(t) + \mu a_0 \cos(\alpha_0 t)c(t) + v(t)] \\
&\quad [c(s) + \mu a_0 \cos(\alpha_0 s)c(s) + v(s)]\} \\
&= \mathbb{E}\{c(t)c(s)\} \\
&\quad + \mu a_0 \cos(\alpha_0 s)\mathbb{E}\{c(t)c(s)\} \\
&\quad + \mu a_0 \cos(\alpha_0 t)\mathbb{E}\{c(t)c(s)\} \\
&\quad + \mu^2 a_0^2 \cos(\alpha_0 t) \cos(\alpha_0 s)\mathbb{E}\{c(t)c(s)\} \\
&\quad + \mathbb{E}\{v(t)v(s)\}.
\end{aligned} \tag{A.1}$$

In the derivation of $R_x(t, s)$, we use the equations $\mathbb{E}\{c(t)\} = \mathbb{E}\{v(t)\} = 0$ and $\mathbb{E}\{c(t)v(s)\} = \mathbb{E}\{c(t)\}\mathbb{E}\{v(s)\} = 0$ as a result of our assumptions. Since we further assume that $c(t)$ and $v(t)$ are wide sense stationary random processes we have $R_c(t, s) = \mathbb{E}\{c(t)c(s)\} = R_c(\tau)$ and $R_v(t, s) = \mathbb{E}\{v(t)v(s)\} = R_v(\tau)$ where $\tau = t - s$. Thus (A.1) becomes

$$\begin{aligned}
R_x(t, \tau) &= R_c(\tau)[1 + \mu a_0 \cos(\alpha_0(t - \tau)) + \mu a_0 \cos(\alpha_0 t) \\
&\quad + \mu^2 a_0^2 \cos(\alpha_0 t) \cos(\alpha_0(t - \tau))] + R_v(\tau).
\end{aligned} \tag{A.2}$$

Then using the Euler's equations we get (2.2). The cyclic autocorrelation function is obtained by FS expansion of (2.2) over t to the cyclic frequency α as

$$\begin{aligned}
C_x(\alpha, \tau) &= \left[\delta(\alpha) + \frac{\mu a_0}{2} e^{-j\alpha_0 \tau} \delta(\alpha - \alpha_0) \right. \\
&\quad + \frac{\mu a_0}{2} e^{j\alpha_0 \tau} \delta(\alpha + \alpha_0) + \frac{\mu a_0}{2} \delta(\alpha - \alpha_0) \\
&\quad + \frac{\mu a_0}{2} \delta(\alpha + \alpha_0) + \frac{\mu^2 a_0^2}{4} e^{-j\alpha_0 \tau} \delta(\alpha - 2\alpha_0) \\
&\quad + \frac{\mu^2 a_0^2}{4} e^{j\alpha_0 \tau} \delta(\alpha + 2\alpha_0) + \frac{\mu^2 a_0^2}{4} e^{j\alpha_0 \tau} \delta(\alpha) \\
&\quad \left. + \frac{\mu^2 a_0^2}{4} e^{-j\alpha_0 \tau} \delta(\alpha) \right] R_c(\tau) + R_v(\tau) \delta(\alpha)
\end{aligned} \tag{A.3}$$

Consequently, we arrive at (2.3) by using the FT relation between the spectral correlation and the cyclic autocorrelation functions where the time difference τ is transformed into the spectral frequency β .

APPENDIX B: Asymptotic Bias of the CCB

The magnitude of the asymptotic CMS given in (4.40) is

$$f(\tilde{\theta}_k, \omega, \alpha_l) = |P(\tilde{\theta}_k, \omega, \alpha_l)| \quad (\text{A.1})$$

which is expected to have a maximum at the asymptotic estimate. Then the asymptotic bias can be calculated using a first-order Taylor series expansion of the first derivative of this function around θ_k [118,120] as

$$\dot{f}(\tilde{\theta}_k) = \dot{f}(\theta_k) + \ddot{f}(\theta_k)\Delta\theta_k + o(\|\Delta\theta_k\|) = 0 \quad (\text{A.2})$$

where we omit the frequency variables for notational convenience. Here, $\dot{f}(\cdot)$ and $\ddot{f}(\cdot)$ represent the first and second-order derivatives with respect to θ_k , respectively. Now we can approximately determine the asymptotic bias, first given in (4.45), as

$$\Delta\theta_k \approx -\frac{\dot{f}(\theta_k)}{\ddot{f}(\theta_k)} \quad (\text{A.3})$$

since the quadratic term $o(\|\Delta\theta_k\|)$ vanishes faster than $\Delta\theta_k$. The first-order derivative can be written as

$$\dot{f}(\theta_k) = \frac{\partial}{\partial \theta_k} |P(\theta_k)| = \frac{\text{Re}(P(\theta_k)\dot{P}(\theta_k)^*)}{|P(\theta_k)|} \quad (\text{A.4})$$

while the second-order derivative becomes

$$\ddot{f}(\theta_k) = \frac{\partial}{\partial \theta_k} \dot{f}(\theta_k) = \frac{|\dot{P}(\theta_k)|^2 + \text{Re}(P(\theta_k)\ddot{P}(\theta_k)^*) - \dot{f}(\theta_k)^2}{|P(\theta_k)|} \quad (\text{A.5})$$

where

$$\begin{aligned} \dot{P}(\theta_k) &= \sum_{q=0}^{Q-1} U_q W_q(\alpha_l) \\ \ddot{P}(\theta_k) &= \sum_{q=0}^{Q-1} V_q W_q(\alpha_l) \end{aligned} \quad (\text{A.6})$$

with

$$\begin{aligned} U_q &= \frac{\partial}{\partial \theta_k} |D_M|^2 = 2\text{Re}(\dot{D}_M D_M^*) \\ V_q &= \frac{\partial^2}{\partial \theta_k^2} |D_M|^2 = 2\text{Re}(\ddot{D}_M D_M^*) + 2|\dot{D}_M|^2 \end{aligned} \quad (\text{A.7})$$

where $D_M = D_M(\omega d(\sin \theta_q - \sin \theta_k)/c)$. Here, \dot{D}_M and \ddot{D}_M are first and second-order derivatives of the Dirichlet kernel with respect to θ_k , respectively. The first-order derivative of the Dirichlet kernel can be explicitly calculated as

$$\dot{D}_M = j\frac{\omega}{c} d \cos \theta_k [(M-1)D_M - \bar{D}_{M-1}] \quad (\text{A.8})$$

where

$$\bar{D}_{M-1} = \frac{1}{M} + \frac{2}{M}D_2 + \cdots + \frac{M-1}{M}D_{M-1}. \quad (\text{A.9})$$

Then, the second-order derivative becomes

$$\begin{aligned} \ddot{D}_M &= -j\frac{\omega}{c}d \sin \theta_k [(M-1)D_M - \bar{D}_{M-1}] \\ &\quad + j\frac{\omega}{c}d \cos \theta_k [(M-1)\dot{D}_M - \dot{\bar{D}}_{M-1}] \end{aligned} \quad (\text{A.10})$$

where

$$\dot{\bar{D}}_{M-1} = \frac{2}{M}\dot{D}_2 + \frac{3}{M}\dot{D}_3 + \cdots + \frac{M-1}{M}\dot{D}_{M-1}. \quad (\text{A.11})$$

The same methodology goes also with the asymptotic ACMS given in (4.44) with its first—and second—order derivatives

$$\begin{aligned} \dot{Y}(\theta_k, \alpha_l) &= \frac{1}{N} \sum_{n=0}^{N-1} \sum_{q=0}^{Q-1} U_{qn} W_q(\alpha_l) \\ \ddot{Y}(\theta_k, \alpha_l) &= \frac{1}{N} \sum_{n=0}^{N-1} \sum_{q=0}^{Q-1} V_{qn} W_q(\alpha_l) \end{aligned} \quad (\text{A.12})$$

respectively, where

$$\begin{aligned} U_{qn} &= 2\text{Re}\{\dot{D}_M D_M^*\} \\ V_{qn} &= 2\text{Re}\{\ddot{D}_M D_M^*\} + 2|\dot{D}_M|^2. \end{aligned} \quad (\text{A.13})$$

Here, the Dirichlet kernel $D_M = D_M(\omega_n d(\sin \theta_q - \sin \theta_k)/c)$ and its derivatives are evaluated at each spectral frequency ω_n . Then we can calculate the asymptotic bias of ACMS using (4.48).

APPENDIX C: Finite-Sample Bias and Variance of the CCB

Apart from the asymptotic bias, CMS given in (4.28) introduces an error due to the estimation using finite number of samples in $\mathbf{X}(\omega, t_i)$. This finite-sample effect causes the final estimate $\hat{\theta}_k$ to deviate from the asymptotic estimate $\tilde{\theta}_k$ with $\Delta\tilde{\theta}_k = \hat{\theta}_k - \tilde{\theta}_k$ [118,120]. Thus, the magnitude of the CMS

$$f(\hat{\theta}_k, \mathbf{X}_{m_1} \mathbf{X}_{m_2}^*) = |\tilde{P}(\hat{\theta}_k, \mathbf{X}_{m_1} \mathbf{X}_{m_2}^*)| \quad (\text{A.1})$$

has a maximum at the final estimate with $\mathbf{X}_m = \mathbf{X}_m(\omega, t_i)$, i.e., the STFT of the m th sensor observations. Then the finite-sample error can be calculated using a first-order Taylor series expansion of the first derivative around $\tilde{\theta}_k$ and $\mathbb{E}\{\mathbf{X}_{m_1} \mathbf{X}_{m_2}^*\}$ as

$$\begin{aligned} & \dot{f}(\hat{\theta}_k, \mathbf{X}_{m_1} \mathbf{X}_{m_2}^*) \\ &= \dot{f}(\tilde{\theta}_k, \mathbb{E}\{\mathbf{X}_{m_1} \mathbf{X}_{m_2}^*\}) + \ddot{f}(\tilde{\theta}_k, \mathbb{E}\{\mathbf{X}_{m_1} \mathbf{X}_{m_2}^*\}) \Delta\tilde{\theta}_k \\ &+ \frac{\partial}{\partial \mathbb{E}\{\mathbf{X}_{m_1} \mathbf{X}_{m_2}^*\}} \dot{f}(\tilde{\theta}_k, \mathbb{E}\{\mathbf{X}_{m_1} \mathbf{X}_{m_2}^*\}) \Delta \mathbb{E}\{\mathbf{X}_{m_1} \mathbf{X}_{m_2}^*\} \\ &+ o(\|\Delta\tilde{\theta}_k\|, \|\Delta \mathbb{E}\{\mathbf{X}_{m_1} \mathbf{X}_{m_2}^*\}\|) = 0 \end{aligned} \quad (\text{A.2})$$

where $\Delta \mathbb{E}\{\mathbf{X}_{m_1} \mathbf{X}_{m_2}^*\} = \mathbb{E}\{\mathbf{X}_{m_1} \mathbf{X}_{m_2}^*\} - \mathbf{X}_{m_1} \mathbf{X}_{m_2}^*$. Since $\dot{f}(\tilde{\theta}_k, \mathbb{E}\{\mathbf{X}_{m_1} \mathbf{X}_{m_2}^*\}) = \dot{f}(\tilde{\theta}_k) = 0$ as given in (A.2) we can approximately determine the finite-sample error as

$$\begin{aligned} \Delta\tilde{\theta}_k &\approx -\frac{\partial}{\partial \mathbb{E}\{\mathbf{X}_{m_1} \mathbf{X}_{m_2}^*\}} \dot{f}(\tilde{\theta}_k, \mathbb{E}\{\mathbf{X}_{m_1} \mathbf{X}_{m_2}^*\}) \Delta \mathbb{E}\{\mathbf{X}_{m_1} \mathbf{X}_{m_2}^*\} \\ &\quad \ddot{f}(\tilde{\theta}_k, \mathbb{E}\{\mathbf{X}_{m_1} \mathbf{X}_{m_2}^*\})^{-1} \end{aligned} \quad (\text{A.3})$$

neglecting the quadratic term $o(\|\Delta\tilde{\theta}_k\|, \|\Delta \mathbb{E}\{\mathbf{X}_{m_1} \mathbf{X}_{m_2}^*\}\|)$. Since $\mathbb{E}\{\Delta \mathbb{E}\{\mathbf{X}_{m_1} \mathbf{X}_{m_2}^*\}\} = 0$, the finite-sample bias $\mathbb{E}\{\Delta\tilde{\theta}_k\} = 0$ which reduces the variance introduced by the finite-sample error to $\mathbb{E}\{\Delta\tilde{\theta}_k^2\}$. Notice that using (A.4) and $\dot{f}(\tilde{\theta}_k, \mathbb{E}\{\mathbf{X}_{m_1} \mathbf{X}_{m_2}^*\}) = 0$ yield

$$\frac{\partial}{\partial \mathbb{E}\{\mathbf{X}_{m_1} \mathbf{X}_{m_2}^*\}} \dot{f}(\tilde{\theta}_k, \mathbb{E}\{\mathbf{X}_{m_1} \mathbf{X}_{m_2}^*\}) \mathbb{E}\{\mathbf{X}_{m_1} \mathbf{X}_{m_2}^*\} = 0 \quad (\text{A.4})$$

and

$$\begin{aligned} & \frac{\partial}{\partial \mathbb{E}\{\mathbf{X}_{m_1} \mathbf{X}_{m_2}^*\}} \dot{f}(\tilde{\theta}_k, \mathbb{E}\{\mathbf{X}_{m_1} \mathbf{X}_{m_2}^*\}) \mathbf{X}_{m_1} \mathbf{X}_{m_2}^* \\ &= \frac{\text{Re}(\tilde{P}\dot{P}^* + P\dot{P}^*)}{|P|} \end{aligned} \quad (\text{A.5})$$

where we dropped $\tilde{\theta}_k$ for notational convenience. Thus

$$\Delta\tilde{\theta}_k \approx \frac{\text{Re}(\tilde{P}\dot{P}^* + P\dot{P}^*)}{|P|\ddot{f}(\tilde{\theta}_k, \mathbb{E}\{\mathbf{X}_{m_1} \mathbf{X}_{m_2}^*\})} \quad (\text{A.6})$$

and finally we arrive at (4.47) using the fact that $\dot{f}(\tilde{\theta}_k, E\{X_{m_1} X_{m_2}^*\}) = \frac{\partial^2}{\partial \tilde{\theta}_k^2} |\mathbf{P}|$.

Similarly, we can obtain the finite-sample variance for ACMS in (4.49) with a final assumption that DFT components are asymptotically independent for stationary random processes [121, Ch. 4], i.e., $C_q(\omega_n, t_i)$'s are independent so that

$$E\{S_q(\omega_{n_1}, t_i) S_q(\omega_{n_2}, t_i)^*\} = \begin{cases} E\{|S_q(\omega_n, t_i)|^2\}, & n_{1,2} = n \\ 0, & \text{otherwise.} \end{cases} \quad (\text{A.7})$$

APPENDIX D: Algebraic Manipulations for Finite-Sample Variance of the CCB
 In Section 4.5.3 we arrive at the approximate finite-sample variance (4.47) where

$$\begin{aligned}
 E\{\text{Re}(\tilde{P}\dot{P}^*)^2\} &= \text{Re}(\dot{P})^2 E\{\text{Re}(\tilde{P})^2\} \\
 &\quad + 2\text{Re}(\dot{P})\text{Im}(\dot{P}) E\{\text{Re}(\tilde{P})\text{Im}(\tilde{P})\} \\
 &\quad + \text{Im}(\dot{P})^2 E\{\text{Im}(\tilde{P})^2\} \\
 E\{\text{Re}(\tilde{P}\dot{P}^*)\text{Re}(P\dot{P}^*)\} &= \text{Re}(P)\text{Re}(\dot{P}) E\{\text{Re}(\tilde{P})\text{Re}(\dot{P})\} \\
 &\quad + \text{Im}(P)\text{Im}(\dot{P}) E\{\text{Im}(\tilde{P})\text{Im}(\dot{P})\} \\
 &\quad + \text{Im}(P)\text{Re}(\dot{P}) E\{\text{Re}(\tilde{P})\text{Im}(\dot{P})\} \\
 &\quad + \text{Re}(P)\text{Im}(\dot{P}) E\{\text{Im}(\tilde{P})\text{Re}(\dot{P})\} \\
 E\{\text{Re}(P\dot{P}^*)^2\} &= \text{Re}(P)^2 E\{\text{Re}(\dot{P})^2\} \\
 &\quad + 2\text{Re}(P)\text{Im}(P) E\{\text{Re}(\dot{P})\text{Im}(\dot{P})\} \\
 &\quad + \text{Im}(P)^2 E\{\text{Im}(\dot{P})^2\}. \tag{A.1}
 \end{aligned}$$

Note that

$$\begin{aligned}
 E\{\text{Re}(\tilde{P})^2\} &= \frac{1}{2} \left[\text{Re}(E\{\tilde{P}^2\}) + E\{|\tilde{P}|^2\} \right] \\
 E\{\text{Re}(\tilde{P})\text{Im}(\tilde{P})\} &= \frac{1}{2} \text{Im}(E\{\tilde{P}^2\}) \\
 E\{\text{Im}(\tilde{P})^2\} &= \frac{1}{2} \left[-\text{Re}(E\{\tilde{P}^2\}) + E\{|\tilde{P}|^2\} \right] \\
 E\{\text{Re}(\tilde{P})\text{Re}(\dot{P})\} &= \frac{1}{2} \left[\text{Re}(E\{\tilde{P}\dot{P}\}) + \text{Re}(E\{\tilde{P}\dot{P}^*\}) \right] \\
 E\{\text{Im}(\tilde{P})\text{Im}(\dot{P})\} &= \frac{1}{2} \left[-\text{Re}(E\{\tilde{P}\dot{P}\}) + \text{Re}(E\{\tilde{P}\dot{P}^*\}) \right] \\
 E\{\text{Re}(\tilde{P})\text{Im}(\dot{P})\} &= \frac{1}{2} \left[\text{Im}(E\{\tilde{P}\dot{P}\}) - \text{Im}(E\{\tilde{P}\dot{P}^*\}) \right] \\
 E\{\text{Im}(\tilde{P})\text{Re}(\dot{P})\} &= \frac{1}{2} \left[\text{Im}(E\{\tilde{P}\dot{P}\}) + \text{Im}(E\{\tilde{P}\dot{P}^*\}) \right] \\
 E\{\text{Re}(\dot{P})^2\} &= \frac{1}{2} \left[\text{Re}(E\{\dot{P}^2\}) + E\{|\dot{P}|^2\} \right] \\
 E\{\text{Re}(\dot{P})\text{Im}(\dot{P})\} &= \frac{1}{2} \text{Im}(E\{\dot{P}^2\}) \\
 E\{\text{Im}(\dot{P})^2\} &= \frac{1}{2} \left[-\text{Re}(E\{\dot{P}^2\}) + E\{|\dot{P}|^2\} \right]. \tag{A.2}
 \end{aligned}$$

Since the asymptotic distribution of the DFT is Gaussian [121, Ch. 4] we can safely assume that Z in (4.29) is normal with zero-mean given that $E\{S_q(\omega, t_i)\} = 0$ and $E\{N_m(\omega, t_i)\} = 0$. For zero-mean Gaussian random variables, Isserlis' theorem [122]

states that

$$\begin{aligned}
\mathbb{E}\{Z_{i_1}Z_{i_1}^*Z_{i_2}Z_{i_2}^*\} &= \mathbb{E}\{Z_{i_1}Z_{i_1}^*\}\mathbb{E}\{Z_{i_2}Z_{i_2}^*\} \\
&+ \mathbb{E}\{Z_{i_1}Z_{i_2}\}\mathbb{E}\{Z_{i_1}^*Z_{i_2}^*\} \\
&+ \mathbb{E}\{Z_{i_1}Z_{i_2}^*\}\mathbb{E}\{Z_{i_1}^*Z_{i_2}\}
\end{aligned} \tag{A.3}$$

where $Z_i = Z(\tilde{\theta}_k, \omega, t_i)$. In addition to the spatial uncorrelatedness assumptions made in Section 4.5.1 we further assume both source signals and noise are temporally uncorrelated, i.e., $\mathbb{E}\{Z_{i_1}Z_{i_2}\} = 0, i_1 \neq i_2$. Then, a few algebraic manipulations lead to

$$\begin{aligned}
&\mathbb{E}\{\tilde{P}^2\} \\
&= P^2 + \frac{1}{I} \left[\sum_{q_1=0}^{Q-1} \sum_{q_2=0}^{Q-1} \left(D_M(\omega, q_1, k)^2 D_M^*(\omega, q_2, k)^2 \right. \right. \\
&+ |D_M(\omega, q_1, k)|^2 |D_M(\omega, q_2, k)|^2 \left. \right) W_{q_1}(2\alpha_l) W_{q_2}(2\alpha_l) \\
&+ \sigma_n^2 D_M^*(-2\omega, 0, k) \sum_{q=0}^{Q-1} D_M^*(\omega, q, k)^2 W_q(2\alpha_l) \\
&+ \sigma_n^2 D_M(-2\omega, 0, k) \sum_{q=0}^{Q-1} D_M(\omega, q, k)^2 W_q(2\alpha_l) \\
&+ 2\sigma_n^2 \sum_{q=0}^{Q-1} |D_M(\omega, q, k)|^2 W_q(2\alpha_l) \\
&+ \left. \sigma_n^4 \left(|D_M(-2\omega, 0, k)|^2 + 1 \right) D_I(2\alpha_l RT_s) \right], \tag{A.4}
\end{aligned}$$

$$\begin{aligned}
&\mathbb{E}\{|\tilde{P}|^2\} \\
&= |P|^2 + \frac{1}{I} \left[\sum_{q_1=0}^{Q-1} \sum_{q_2=0}^{Q-1} \left(D_M(\omega, q_1, k)^2 D_M^*(\omega, q_2, k)^2 \right. \right. \\
&+ |D_M(\omega, q_1, k)|^2 |D_M(\omega, q_2, k)|^2 \left. \right) W_{q_1}(0) W_{q_2}(0) \\
&+ \sigma_n^2 D_M^*(-2\omega, 0, k) \sum_{q=0}^{Q-1} D_M^*(\omega, q, k)^2 W_q(0) \\
&+ \sigma_n^2 D_M(-2\omega, 0, k) \sum_{q=0}^{Q-1} D_M(\omega, q, k)^2 W_q(0) \\
&+ 2\sigma_n^2 \sum_{q=0}^{Q-1} |D_M(\omega, q, k)|^2 W_q(0) \\
&+ \left. \sigma_n^4 \left(|D_M(-2\omega, 0, k)|^2 + 1 \right) \right], \tag{A.5}
\end{aligned}$$

$$\begin{aligned}
& \mathbb{E}\{\tilde{\mathbf{P}}\dot{\mathbf{P}}\} = \mathbf{P}\dot{\mathbf{P}} \\
& + \frac{1}{I} \left[\sum_{q_1=0}^{Q-1} \sum_{q_2=0}^{Q-1} \left(2\text{Re}(\dot{\mathbf{D}}_M(\boldsymbol{\omega}, q_1, k)\mathbf{D}_M(\boldsymbol{\omega}, q_1, k) \right. \right. \\
& \mathbf{D}_M^*(\boldsymbol{\omega}, q_2, k)^2) + 2\text{Re}(\dot{\mathbf{D}}_M(\boldsymbol{\omega}, q_1, k)\mathbf{D}_M^*(\boldsymbol{\omega}, q_1, k) \\
& \left. \left. |\mathbf{D}_M(\boldsymbol{\omega}, q_2, k)|^2) \right) \mathbf{W}_{q_1}(2\alpha_l)\mathbf{W}_{q_2}(2\alpha_l) \right. \\
& + \frac{\sigma_n^2}{2} \dot{\mathbf{D}}_M^*(-2\boldsymbol{\omega}, 0, k) \sum_{q=0}^{Q-1} \mathbf{D}_M^*(\boldsymbol{\omega}, q, k)^2 \mathbf{W}_q(2\alpha_l) \\
& + \frac{\sigma_n^2}{2} \dot{\mathbf{D}}_M(-2\boldsymbol{\omega}, 0, k) \sum_{q=0}^{Q-1} \mathbf{D}_M(\boldsymbol{\omega}, q, k)^2 \mathbf{W}_q(2\alpha_l) \\
& + \sigma_n^2 \mathbf{D}_M(-2\boldsymbol{\omega}, 0, k) \sum_{q=0}^{Q-1} \dot{\mathbf{D}}_M(\boldsymbol{\omega}, q, k)\mathbf{D}_M(\boldsymbol{\omega}, q, k)\mathbf{W}_q(2\alpha_l) \\
& + \sigma_n^2 \mathbf{D}_M^*(-2\boldsymbol{\omega}, 0, k) \sum_{q=0}^{Q-1} \dot{\mathbf{D}}_M^*(\boldsymbol{\omega}, q, k)\mathbf{D}_M^*(\boldsymbol{\omega}, q, k)\mathbf{W}_q(2\alpha_l) \\
& + \sigma_n^2 \sum_{q=0}^{Q-1} \dot{\mathbf{D}}_M(\boldsymbol{\omega}, q, k)\mathbf{D}_M^*(\boldsymbol{\omega}, q, k)\mathbf{W}_q(2\alpha_l) \\
& + \sigma_n^2 \sum_{q=0}^{Q-1} \dot{\mathbf{D}}_M^*(\boldsymbol{\omega}, q, k)\mathbf{D}_M(\boldsymbol{\omega}, q, k)\mathbf{W}_q(2\alpha_l) \\
& \left. + \sigma_n^4 \text{Re} \left(\dot{\mathbf{D}}_M^*(-2\boldsymbol{\omega}, 0, k)\mathbf{D}_M(-2\boldsymbol{\omega}, 0, k) \right) \mathbf{D}_I(2\alpha_l RT_s) \right], \quad (\text{A.6})
\end{aligned}$$

$$\begin{aligned}
\mathbb{E}\{\tilde{\mathbf{P}}\dot{\mathbf{P}}^*\} &= \mathbf{P}\dot{\mathbf{P}}^* \\
&+ \frac{1}{I} \left[\sum_{q_1=0}^{Q-1} \sum_{q_2=0}^{Q-1} \left(2\text{Re}(\dot{D}_M(\boldsymbol{\omega}, q_1, k)D_M(\boldsymbol{\omega}, q_1, k) \right. \right. \\
&D_M^*(\boldsymbol{\omega}, q_2, k)^2) + 2\text{Re}(\dot{D}_M(\boldsymbol{\omega}, q_1, k)D_M^*(\boldsymbol{\omega}, q_1, k) \\
&|D_M(\boldsymbol{\omega}, q_2, k)|^2) \left. \right) \mathbf{W}_{q_1}(0)\mathbf{W}_{q_2}(0) \\
&+ \frac{\sigma_n^2}{2} \dot{D}_M^*(-2\boldsymbol{\omega}, 0, k) \sum_{q=0}^{Q-1} D_M^*(\boldsymbol{\omega}, q, k)^2 \mathbf{W}_q(0) \\
&+ \frac{\sigma_n^2}{2} \dot{D}_M(-2\boldsymbol{\omega}, 0, k) \sum_{q=0}^{Q-1} D_M(\boldsymbol{\omega}, q, k)^2 \mathbf{W}_q(0) \\
&+ \sigma_n^2 D_M(-2\boldsymbol{\omega}, 0, k) \sum_{q=0}^{Q-1} \dot{D}_M(\boldsymbol{\omega}, q, k) D_M(\boldsymbol{\omega}, q, k) \mathbf{W}_q(0) \\
&+ \sigma_n^2 D_M^*(-2\boldsymbol{\omega}, 0, k) \sum_{q=0}^{Q-1} \dot{D}_M^*(\boldsymbol{\omega}, q, k) D_M^*(\boldsymbol{\omega}, q, k) \mathbf{W}_q(0) \\
&+ \sigma_n^2 \sum_{q=0}^{Q-1} \dot{D}_M(\boldsymbol{\omega}, q, k) D_M^*(\boldsymbol{\omega}, q, k) \mathbf{W}_q(0) \\
&+ \sigma_n^2 \sum_{q=0}^{Q-1} \dot{D}_M^*(\boldsymbol{\omega}, q, k) D_M(\boldsymbol{\omega}, q, k) \mathbf{W}_q(0) \\
&+ \sigma_n^4 \text{Re} \left(\dot{D}_M^*(-2\boldsymbol{\omega}, 0, k) D_M(-2\boldsymbol{\omega}, 0, k) \right) \left. \right], \tag{A.7}
\end{aligned}$$

$$\begin{aligned}
& \mathbb{E}\{\dot{\mathbf{P}}^2\} = \dot{\mathbf{P}}^2 \\
& + \frac{1}{I} \left[\sum_{q_1=0}^{Q-1} \sum_{q_2=0}^{Q-1} \left(2\text{Re}(\dot{\mathbf{D}}_M(\omega, q_1, k)^2 \mathbf{D}_M^*(\omega, q_2, k)^2) \right. \right. \\
& + 2|\dot{\mathbf{D}}_M(\omega, q_1, k)|^2 |\mathbf{D}_M(\omega, q_2, k)|^2 \\
& + 2\text{Re}(\dot{\mathbf{D}}_M(\omega, q_1, k) \mathbf{D}_M^*(\omega, q_1, k) \dot{\mathbf{D}}_M(\omega, q_2, k) \mathbf{D}_M^*(\omega, q_2, k)) \\
& \left. \left. + 2\dot{\mathbf{D}}_M(\omega, q_1, k) \mathbf{D}_M(\omega, q_1, k) \dot{\mathbf{D}}_M^*(\omega, q_2, k) \mathbf{D}_M^*(\omega, q_2, k) \right) \right] \\
& \mathbf{W}_{q_1}(2\alpha_l) \mathbf{W}_{q_2}(2\alpha_l) \\
& + \frac{\sigma_n^2}{4} \left(\dot{\mathbf{D}}_M^*(-2\omega, 0, k) + \dot{\mathbf{D}}_M^*(-2\omega, 0, k) \tan \tilde{\theta}_k \right) \\
& \sum_{q=0}^{Q-1} \mathbf{D}_M^*(\omega, q, k)^2 \mathbf{W}_q(2\alpha_l) \\
& + \frac{\sigma_n^2}{4} \left(\dot{\mathbf{D}}_M(-2\omega, 0, k) + \dot{\mathbf{D}}_M(-2\omega, 0, k) \tan \tilde{\theta}_k \right) \\
& \sum_{q=0}^{Q-1} \mathbf{D}_M(\omega, q, k)^2 \mathbf{W}_q(2\alpha_l) \\
& + \sigma_n^2 \mathbf{D}_M(-2\omega, 0, k) \sum_{q=0}^{Q-1} \dot{\mathbf{D}}_M(\omega, q, k)^2 \mathbf{W}_q(2\alpha_l) \\
& + \sigma_n^2 \mathbf{D}_M^*(-2\omega, 0, k) \sum_{q=0}^{Q-1} \dot{\mathbf{D}}_M^*(\omega, q, k)^2 \mathbf{W}_q(2\alpha_l) \\
& + \frac{\sigma_n^2 \omega^2 d^2 \cos^2 \tilde{\theta}_k (M-1)(2M-1)}{3c^2} \sum_{q=0}^{Q-1} |\mathbf{D}_M(\omega, q, k)|^2 \\
& \mathbf{W}_q(2\alpha_l) + 2\sigma_n^2 \sum_{q=0}^{Q-1} |\dot{\mathbf{D}}_M(\omega, q, k)|^2 \mathbf{W}_q(2\alpha_l) \\
& + \sigma_n^2 \dot{\mathbf{D}}_M^*(-2\omega, 0, k) \sum_{q=0}^{Q-1} \dot{\mathbf{D}}_M^*(\omega, q, k) \mathbf{D}_M^*(\omega, q, k) \mathbf{W}_q(2\alpha_l) \\
& + \sigma_n^2 \dot{\mathbf{D}}_M(-2\omega, 0, k) \sum_{q=0}^{Q-1} \dot{\mathbf{D}}_M(\omega, q, k) \mathbf{D}_M(\omega, q, k) \mathbf{W}_q(2\alpha_l) \\
& + j \frac{\sigma_n^2 \omega d \cos \tilde{\theta}_k (M-1)}{c} \sum_{q=0}^{Q-1} \dot{\mathbf{D}}_M(\omega, q, k) \mathbf{D}_M^*(\omega, q, k) \mathbf{W}_q(2\alpha_l) \\
& - j \frac{\sigma_n^2 \omega d \cos \tilde{\theta}_k (M-1)}{c} \sum_{q=0}^{Q-1} \dot{\mathbf{D}}_M^*(\omega, q, k) \mathbf{D}_M(\omega, q, k) \mathbf{W}_q(2\alpha_l) \\
& + \left(\frac{\sigma_n^4}{2} \text{Re}((\dot{\mathbf{D}}_M^*(-2\omega, 0, k) + \dot{\mathbf{D}}_M^*(-2\omega, 0, k) \tan \tilde{\theta}_k) \right. \\
& \mathbf{D}_M(-2\omega, 0, k)) + \frac{\sigma_n^4 \omega^2 d^2 \cos^2 \tilde{\theta}_k (M-1)(2M-1)}{3c^2} \\
& \left. - \frac{\sigma_n^4 \omega^2 d^2 \cos^2 \tilde{\theta}_k (M-1)^2}{2c^2} + \frac{\sigma_n^4}{2} |\dot{\mathbf{D}}_M(-2\omega, 0, k)|^2 \right) \mathbf{D}_I(2\alpha_l RT_s) \Big], \quad (\text{A.8})
\end{aligned}$$

$$\begin{aligned}
& \mathbb{E}\{|\dot{\tilde{\mathbf{P}}}|^2\} = |\dot{\tilde{\mathbf{P}}}|^2 \\
& + \frac{1}{I} \left[\sum_{q_1=0}^{Q-1} \sum_{q_2=0}^{Q-1} \left(2\text{Re}(\dot{\mathbf{D}}_M(\boldsymbol{\omega}, q_1, k)^2 \mathbf{D}_M^*(\boldsymbol{\omega}, q_2, k)^2) \right. \right. \\
& + 2|\dot{\mathbf{D}}_M(\boldsymbol{\omega}, q_1, k)|^2 |\mathbf{D}_M(\boldsymbol{\omega}, q_2, k)|^2 \\
& + 2\text{Re}(\dot{\mathbf{D}}_M(\boldsymbol{\omega}, q_1, k) \mathbf{D}_M^*(\boldsymbol{\omega}, q_1, k) \dot{\mathbf{D}}_M(\boldsymbol{\omega}, q_2, k) \mathbf{D}_M^*(\boldsymbol{\omega}, q_2, k)) \\
& \left. \left. + 2\dot{\mathbf{D}}_M(\boldsymbol{\omega}, q_1, k) \mathbf{D}_M(\boldsymbol{\omega}, q_1, k) \dot{\mathbf{D}}_M^*(\boldsymbol{\omega}, q_2, k) \mathbf{D}_M^*(\boldsymbol{\omega}, q_2, k) \right) \right] \\
& \mathbf{W}_{q_1}(0) \mathbf{W}_{q_2}(0) \\
& + \frac{\sigma_n^2}{4} \left(\ddot{\mathbf{D}}_M^*(-2\boldsymbol{\omega}, 0, k) + \dot{\mathbf{D}}_M^*(-2\boldsymbol{\omega}, 0, k) \tan \tilde{\theta}_k \right) \\
& \sum_{q=0}^{Q-1} \mathbf{D}_M^*(\boldsymbol{\omega}, q, k)^2 \mathbf{W}_q(0) \\
& + \frac{\sigma_n^2}{4} \left(\ddot{\mathbf{D}}_M(-2\boldsymbol{\omega}, 0, k) + \dot{\mathbf{D}}_M(-2\boldsymbol{\omega}, 0, k) \tan \tilde{\theta}_k \right) \\
& \sum_{q=0}^{Q-1} \mathbf{D}_M(\boldsymbol{\omega}, q, k)^2 \mathbf{W}_q(0) \\
& + \sigma_n^2 \mathbf{D}_M(-2\boldsymbol{\omega}, 0, k) \sum_{q=0}^{Q-1} \dot{\mathbf{D}}_M(\boldsymbol{\omega}, q, k)^2 \mathbf{W}_q(0) \\
& + \sigma_n^2 \mathbf{D}_M^*(-2\boldsymbol{\omega}, 0, k) \sum_{q=0}^{Q-1} \dot{\mathbf{D}}_M^*(\boldsymbol{\omega}, q, k)^2 \mathbf{W}_q(0) \\
& + \frac{\sigma_n^2 \omega^2 d^2 \cos^2 \tilde{\theta}_k (M-1)(2M-1)}{3c^2} \sum_{q=0}^{Q-1} |\mathbf{D}_M(\boldsymbol{\omega}, q, k)|^2 \\
& \mathbf{W}_q(0) + 2\sigma_n^2 \sum_{q=0}^{Q-1} |\dot{\mathbf{D}}_M(\boldsymbol{\omega}, q, k)|^2 \mathbf{W}_q(0) \\
& + \sigma_n^2 \dot{\mathbf{D}}_M^*(-2\boldsymbol{\omega}, 0, k) \sum_{q=0}^{Q-1} \dot{\mathbf{D}}_M^*(\boldsymbol{\omega}, q, k) \mathbf{D}_M^*(\boldsymbol{\omega}, q, k) \mathbf{W}_q(0) \\
& + \sigma_n^2 \dot{\mathbf{D}}_M(-2\boldsymbol{\omega}, 0, k) \sum_{q=0}^{Q-1} \dot{\mathbf{D}}_M(\boldsymbol{\omega}, q, k) \mathbf{D}_M(\boldsymbol{\omega}, q, k) \mathbf{W}_q(0) \\
& + j \frac{\sigma_n^2 \omega d \cos \tilde{\theta}_k (M-1)}{c} \sum_{q=0}^{Q-1} \dot{\mathbf{D}}_M(\boldsymbol{\omega}, q, k) \mathbf{D}_M^*(\boldsymbol{\omega}, q, k) \mathbf{W}_q(0) \\
& - j \frac{\sigma_n^2 \omega d \cos \tilde{\theta}_k (M-1)}{c} \sum_{q=0}^{Q-1} \dot{\mathbf{D}}_M^*(\boldsymbol{\omega}, q, k) \mathbf{D}_M(\boldsymbol{\omega}, q, k) \mathbf{W}_q(0) \\
& + \frac{\sigma_n^4}{2} \text{Re}((\ddot{\mathbf{D}}_M^*(-2\boldsymbol{\omega}, 0, k) + \dot{\mathbf{D}}_M^*(-2\boldsymbol{\omega}, 0, k) \tan \tilde{\theta}_k) \\
& \mathbf{D}_M(-2\boldsymbol{\omega}, 0, k)) + \frac{\sigma_n^4 \omega^2 d^2 \cos^2 \tilde{\theta}_k (M-1)(2M-1)}{3c^2} \\
& \left. - \frac{\sigma_n^4 \omega^2 d^2 \cos^2 \tilde{\theta}_k (M-1)^2}{2c^2} + \frac{\sigma_n^4}{2} |\dot{\mathbf{D}}_M(-2\boldsymbol{\omega}, 0, k)|^2 \right] \tag{A.9}
\end{aligned}$$

where $D_M(\omega, q, k) = D_M(\omega d(\sin \theta_q - \sin \tilde{\theta}_k)/c)$, $\dot{D}_M(\omega, q, k) = \dot{D}_M(\omega d(\sin \theta_q - \sin \tilde{\theta}_k)/c)$ and $\ddot{D}_M(\omega, q, k) = \ddot{D}_M(\omega d(\sin \theta_q - \sin \tilde{\theta}_k)/c)$. Using (A.4)-(A.9) we can calculate (A.2), (A.1) and then we get (4.47).

Similarly, the finite-sample variance (4.49) can be calculated by replacing P's with Y's in (A.1).

CURRICULUM VITAE

Name Surname: Umut FIRAT

EDUCATION:

- **B.Sc.:** 2003, Yıldız Technical University, Faculty of Electrical & Electronics, Department of Electronics & Communications Engineering
- **M.Sc.:** 2006, Yıldız Technical University, Faculty of Electrical & Electronics, Department of Electronics & Communications Engineering

PROFESSIONAL EXPERIENCE AND REWARDS:

- 2023-Present Department Head at TÜBİTAK BİLGEM
- 2017 İTÜ-BAP Grant (Project 39264)
- 2013 TÜBİTAK BİDEB 2224 Grant
- 2012 Visiting Researcher at STO CMRE (Fellowship)
- 2011-2023 Senior Researcher at TÜBİTAK BİLGEM
- 2010 TÜBİTAK BİDEB 2224 Grant
- 2007-2011 Researcher at TÜBİTAK MAM
- 2006 Electronics Engineer at Verifone
- 2005 Electronics Engineer at Tekofaks Panasonic

PUBLICATIONS, PRESENTATIONS AND PATENTS ON THE THESIS:

- **Firat, U. & Akgül, T.** "Compressive sensing of cyclic bispectrum." (submitted to IEEE Journal of Oceanic Engineering in February 2023).
- **Firat, U. & Akgül, T.** "Compressive beamformer for direction-of-arrival estimation of cyclostationary propeller noise." Signal Processing 214 (2024).
- **Firat, U., Akgül, T., & Dede, A.** "Ambient, ship-radiated and biologic noise in bosporus and gokceada." 1. National Bioacoustics Workshop (2018), Gökçeada, Çanakkale, Türkiye.

- **Firat, U. & Akgül, T.** "Compressive sensing for detecting ships with second-order cyclostationary signatures." *IEEE Journal of Oceanic Engineering* 43.4 (2017): 1086-1098.
- **Firat, U. & Akgül, T.** "Gemi akustik iz analizi." (in Turkish) *EMO Bilimsel Dergi* 7.13 (2017): 25-31.
- **Firat, U. & Akgül, T.** "Spectral estimation of cavitation related narrow-band ship radiated noise based on fractional lower order statistics and multiple signal classification." *IEEE OCEANS Conference* (2013), San Diego, USA.

OTHER PUBLICATIONS, PRESENTATIONS AND PATENTS:

- **Firat, U., Engin, Ş. N., Saraçlar, M., & Ertüzün, A. B.** "Wind speed forecasting based on second order blind identification and autoregressive model." *IEEE Ninth International Conference on Machine Learning and Applications* (2010), Washington DC, USA.
- **Firat U.,** "Kaotik zaman serilerinin yapay sinir ağlarıyla kestirimi: deprem verisi durumu." (in Turkish), M.Sc. Thesis (2006).
- **Firat, U.,** "Yapay sinir ağı kullanarak deprem eğiliminin kestirimi." (in Turkish) *Earthquake Symposium* (2005), Kocaeli, Türkiye.